DIFFERENTIALLY-ENCODED DI-SYMBOL TIME-DIVISION MULTIUSER IMPULSE RADIO IN UWB CHANNEL

ZHANG QI

(*M. Sci., UESTC, P. R. China*)

A THESIS SUBMITTED FOR THE DEGREE OF PH. D.

DEPARTMENT OF ELECTRICAL AND COMPUTER ENGINEERING

NATIONAL UNIVERSITY OF SINGAPORE

2007

to my parents

Acknowledgements

I am indebted to many people toward the completion of my Ph.D. study. It would be impossible to finish this journey without their guidance and support.

I own my greatest gratitude to my supervisor, Prof. Ng Chun Sum, for his patient guidance all through my Ph.D. study. Particularly, he patiently read through every paragraph of this thesis, gave me many valuable suggestions in thesis writing, and helped me correct numerous English mistakes throughout the manuscript. His down-to-earth research attitude and step-by-step approach impressed me deeply.

I would like to thank Prof. Tjhung Tjeng Thiang and Prof. Arumugam Nallanathan, who are the committee members of my Ph.D. Qualifying Examination (QE), for their valuable and constructive suggestions on my QE report. My gratitude also goes to many other professors who had taught me or discussed with me.

I wish to thank my wonderful colleges in Communications Laboratory for their friendship and help. They are Sun Zhenyu, Shan Cheng, Yu Zhan, Peng Ningkun, Bao Qiming, Li Yan, Li Rong, Wang Xiaoli, Zhang Jianwen, Ng Khai Sheng, Li Mi, He Jun, Zhu Yonglan, Jiang Jinhua, Lokesh Bheema Thiagarajan, Hou Shengwei, Zhang Xiaolu, Zhang Lan, Liu Fangming, and Da Bin. The warm discussions between us on countless research/non-research topics are part of my

enjoyable memory at National University of Singapore.

Thanks are also given to Ms. Serene Oe, who is the lab officer of the Communications Laboratory, for her help during the last 4 years.

My Ph.D. study is supported by National University of Singapore. I deeply appreciate the provider of the scholarship for giving me this precious opportunity of top quality education and research.

Finally I would like to thank my parents and my sister. It is their endless love, support and encouragement that stimulate me to walk through the 23 years of education and to advance further. I dedicate this thesis to them.

Summary

In this thesis, we proposed a differentially-encoded, di-symbol time-division multiuser impulse radio (d^2TD-IR) system with delay-sum autocorrelation receivers (AcRs). In traditional time-division multiple access systems, each user transmits a single pulse during a symbol duration in a pre-assigned chip which is longer than maximum excess delay of the channel. However, due to the exponential decay property of ultra-wideband (UWB) channel, we proposed the use of much shorter chip duration, which significantly increases the transmission rate. Because dense pulse transmission will induce multiuser interference, two time-hopping access sequences, which alternately encode the odd- and even-index symbols, are employed with delay-sum AcRs to maximally suppress the interference. It was shown that when the chip duration is properly chosen, the proposed system outperforms conventional time-hopping impulse radio system at high signal-to-noise ratio (SNR). This thesis also proposed a method to estimate the optimal chip duration when only the average power decay profile of the UWB channel is known.

The proposed d^2TD-IR system assumes perfect synchronization among users. To complete the system, we proposed a synchronization algorithm based on time of arrival estimation. This was developed into a recursive algorithm which combines synchronization and power control. Simulation results showed that after the

synchronization process or combined process of synchronization and power control, the system bit-error-rate (BER) performances get very close to those of a system with perfect synchronization and power control.

To achieve low BER at relatively low SNR, we examined the effects of low-density parity-check (LDPC) codes on the d^2TD-IR system. Compared with an uncoded system, the LDPC coded system was observed to achieve a much lower BER at relatively low SNR. A class of LDPC product codes was also proposed to reduce the encoding complexity of conventional LDPC codes at the expense of slight degradation in BER performance and slight increase in decoding complexity.

Finally, the single-input single-output (SISO) d^2TD-IR was extended to a differential space-time coded (DSTC) multiple-input-multiple-output (MIMO) system. It was observed that because of spatial diversity, a system employing 2 transmit and 2 receive antennas achieves significant performance gain over a SISO system. For a single user system, when there is no intersymbol interference (ISI), we derived the system BER performance which matches the simulation results. In the above situation, it was also found the code performance only depends on the code distance and not on the rank criterion as in conventional DSTC MIMO systems. In ISI channel, it was shown that codes with a Toeplitz structure can improve BER performance. Based on the group structure, corresponding maximum distance codes were designed for arbitrary number of the transmit antennas.

Contents

List of Figures

List of Tables

List of Abbreviations

AcR	autocorrelation receiver
ARake	All-Rake
AWGN	additive white Gaussian noise
BER	bit-error-rate
BEP	bit-error-probability
BIAWGN	binary-input additive white Gaussian noise
BPSK	binary phase-shift-keying
BS	base station
CDMA	code-division multiple access
CM	channel model
CMOS	complementary metal oxide semiconductor
d^2TD-IR	differentially-encoded di-symbol time-division multiuser impulse radio
DC	direct current
DRC	differential repetition codes
DS	direct-sequence
DSTC	differential space-time codes
FCC	Federal Communication Commission
FEC	forward error correction

FH	frequency-hopping
FIR	finite impulse response
GPS	global positioning system
IEEE	Institute of Electrical and Electronics Engineers
IFI	inter-frame interference
IR	impulse radio
ISI	intersymbol interference
LDPC	low-density parity-check
LOS	line-of-sight
MAT	mean acquisition time
MIMO	multiple-input-multiple-output
MMSE	minimum mean-square error
MUI	multiuser interference
NLOS	non-line-of-sight
OFDM	orthogonal frequency division multiplexing
OOK	on-off keying
OSI	open systems interconnect
PAM	pulse amplitude modulation
PPM	pulse position modulation
PRake	partial Rake
PSM	pulse shape modulation
RMS	root-mean-square
SISO	single-input-single-output
SNR	signal-to-noise ratio

SRake	selective Rake
STDL	stochastic tapped-delay-line
STF	space-time-frequency
S-V	Saleh-Valenzuela
TDMA	time-division multiple access
TH	time-hopping
TOA	time of arrival
TR	transmitted-reference
UWB	Ultra-wideband
WLAN	wireless local area network
WPAN	wireless personal area network
WBAN	wireless body area network

Chapter 1

Introduction

1.1 Background

Ultra-wideband (UWB), a short-range wireless communication technology, is extensively considered for future wireless local area networks (WLANs), wireless personal area and body area networks (WPANs and WBANs), as well as ad hoc and home area networks [1, 2]. These short-range wireless networks, when integrated with the exiting global positioning system (GPS), code-division multiple access (CDMA) system and widespread Internet, enable connectivity for "everybody and everything at any place and any time". Such connectivity demand, driven by a new mobile lifestyle, is indicated by the success of IEEE 802.11 (a, b, g) and Bluetooth products, and the imminent arrival of ZigBee (IEEE 802.15.4) and IEEE 802.15.3 products. However, new and increasingly challenging requirements constantly emerge from the user side, such as high-rate data access, long battery life, boundaryless mobility, intelligent and context-aware devices, and applications offering availability of undisrupted service across different networks. Many of these

requirements frequently contrast with the reality of radio system engineering, where frequency resources are scarce and in high demand. UWB technology is likely to offer a solution for future short-range wireless networks.

1.2 UWB Technology

1.2.1 Brief History

The origin of UWB technology stems from work in time-domain electromagnetics, begun in 1962, to fully describe the transient behavior of a certain class of microwave networks through their characteristic impulse response [3].

However, it was not until the advent of the sampling oscilloscope (Hewlett-Packard 1962) and the development of techniques for subnanosecond (baseband) pulse generation, to provide suitable approximations to an impulse excitation, that the impulse response of microwave networks could be directly observed and measured.

Once impulse measurement techniques were applied to the design of wideband, radiating antenna elements [4], it quickly became obvious that short pulse radar and communications systems could be developed with the same set of tools. These techniques were applied to various applications in radar and communications [5].

The invention of a sensitive, short pulse receiver by Robbins [6] in 1972 to replace the cumbersome time-domain sampling oscilloscope further accelerated system development.

Till 1994, UWB technology was mainly considered for military applications. Thereafter, it was extensively studied for commercial applications such as high speed WLANs, obstacle avoidance radars, precision location tracking and imaging

radars [1, 2].

1.2.2 Modern Definition of UWB

Traditionally, UWB systems are referred to as impulse radio (IR) and its synonymous terms. The transmitter works by sending a train of short pulses (also called monocycles), usually on the order of a nanosecond [7, 8]. The corresponding receiver then translates the pulses into data by listening for a familiar pulse sequence sent by the transmitter. Recently, UWB systems have been redefined with a broader scope to include any device emitting signals with a fractional bandwidth greater than 0.2 or a bandwidth of at least 500 MHz at all times during transmission. The fractional bandwidth is defined by the expression $2(f_H - f_L)/(f_H + f_L)$, where f_H is the upper frequency and f_L the lower frequencies at the -10 dB emission point. By spreading the signal over a broad span of frequency, the average power per Hertz will be very low. The U.S. Federal Communication Commission (FCC) prescribes that the imposed power spectral density should be less than 75 nW/MHz between 3.1 GHz and 10.6 GHz [9]. Thus, the UWB signal appears noise-like and is able to coexist with the prevailing narrowband or wideband systems.

UWB systems can be divided into two groups: multiband and single-band. Multiband UWB systems divide the spectrum between 3.1 to 10.6 GHz into several subbands which are at least 500 MHz wide in compliance with FCC regulations [10–12]. In each subband, multiband UWB systems transmit one pulse and wait until the echoes have died out, which give low inter-frame interference (IFI) but high data rates since signals are transmitted simultaneously using different subbands. Single-band UWB systems are usually referred to as impulse radio (IR).

Single-band impulse radio systems have several advantages over multiband

systems and conventional modulation schemes as listed below:

- since the transmitted pulse train is a baseband signal, IR nullifies expensive radio frequency components in both transmitter and receiver;
- because the baseband pulse train operates in the lowest possible frequency band (it is not modulated onto a carrier), it has the best chance of penetrating obstacles that would be opaque at higher frequencies [8];
- the pulse train has a very low duty cycle which minimizes the interference to other pulse trains operating in the same environment;

In this thesis, we will focus on the single-band impulse radio systems.

1.2.3 Impulse Radio

In impulse radio systems [7, 8, 13–29], the information is conveyed either by the polarity of the pulse (usually referred to as pulse amplitude modulation (PAM)) [17], or by shifting the pulse starting time (usually referred to as pulse position modulation (PPM)) [18]. Other modulation schemes, such as conveying the information by transmitting the pulses or not (usually referred to as on-off keying (OOK)) [19] and by varying the shapes of pulses (usually referred to as pulse shape modulation (PSM)) [20], have also been proposed. However, PAM and PPM are more commonly used since they have been shown to outperform OOK and PSM [21].

To allow many users to share the same channel, each link uses a train of pulses to transmit one information symbol with either distinct pulse-amplitude pattern called a code sequence (usually referred to as direct-sequence impulse radio (DS-IR)) or distinct pulse-shift pattern called a time-hopping sequence (usually referred

to as time-hopping impulse radio (TH-IR)) [18]. With well designed code sequences or time-hopping sequences, catastrophic collisions among different users can be effectively avoided.

However, coherent detection of impulse radio signals is a challenging problem. The short duration of the pulse makes the time acquisition task formidable [22]. The inaccuracy of the time acquisition will result in severe performance degradation [23]. Furthermore, the signal energy is dispersed into different multipath components. To fully exploit the signal energy, Rake receivers are often utilized to maximally capture the energy of the signal and this usually results in highly sophisticated, hence impractical systems [24–26].

For slow-fading channels, transmitted-reference impulse radio (including differential transmitted-reference impulse radio) with an autocorrelation receiver (TR-IR/AcR) [30–43] is an attractive low complexity alternative. TR-IR/AcR schemes can be used to exploit multipath diversity without the need for stringent acquisition and channel estimation [32]. Some existing key works in TR-IR/AcR systems are reviewed in the following subsection.

1.2.4 Transmitted-Reference Impulse Radio

TR-IR/AcR was first adopted in the delay-hopped transmitted-reference system [30]. For each symbol, the system transmits two pulses, one is unmodulated reference (or pilot) pulse and the other is data modulated pulse. Delay-hopping means the delays between the pairs of the pulses vary according to a fixed pattern known to the transmitter and the receiver. The received pilot pulses are then used to form the correlator template for symbol detection. In [31], a differential modulation scheme was introduced by Ho et al. The proposed system uses the

previously transmitted information signal as reference, or pilot, signal. In doing so, the transmission rate of the system can be doubled.

Theoretical performance analysis of TR-IR was first done by Choi and Stark [32], who considered a simple situation where there is no intersymbol interference (ISI). The noise-noise crossterms in their formula of computing system bit-error-rate (BER) performance are approximated to be Gaussian random variables. The BER expression is obtained by numerically averaging the conditional BER over different realizations of the UWB channel model.

Recently, Quek et al derived a closed-form BER expression in dense multipath channels [33]. In the derivation, the noise-noise crossterms is expressed using the sampling expansion approach instead of Gaussian approximation. Although Quek's method is able to accurately predict the performance of TR-IR, its application is not extensive owing to the adoption of an overly simplified channel model in [33]. For more realistic and sophisticated channel models found in the literature, such as [44], Quek's method is not applicable. Furthermore, for most applications of TR-IR, Gaussian approximation is able to approximate the noise-noise crossterms with sufficient accuracy.

In [32, 33], the authors assumed perfect channel synchronization. In the presence of synchronization errors, Ning and Tepedelenlioglu analyzed the system performance with respect to various synchronization accuracy levels [34]. The analysis showed that unlike DS-IR and TH-IR which are very sensitive to synchronization errors, TR-IR/AcR suffers only slight performance degradation when subjected to the same degree of synchronization errors.

The major drawback of TR-IR/AcR lies in employing correlator templates that are corrupted by interference from other users and channel noise during demod-

ulation. This induces performance degradation. To address that problem, many methods have been proposed in the literature [35–42]. The underline mechanism of these methods is to efficiently couple multiple data modulated pulses with multiple unmodulated reference (or pilot) pulses for each symbol transmission.

For example, the 'frame-differential' IR scheme of Witrisal et al [39] transmits each data symbol with a coded pulse-sequence comprising alternate unmodulated (pilot) and modulated (data) pulses. The receiver consists of a bank of pulse-pair correlators that are used to generate the correlation values of successive pairs of odd- and even-index pulses of a received symbol, and the decision statistic for symbol detection is formed by summing these correlation values.

Another implementation can be seen in the differential receiver structure proposed by Tufversson et al [37, 38], which is applied to noncoherent detection of time-hopping impulse radio (TH-IR). Here, each data symbol is transmitted using one coded pilot pulse-sequence and one data pulse-sequence, which is an amplitude modulated and delayed version of the pilot sequence. At the receiver, the pilot and data pulse-sequences of a received symbol are each despreaded using a front-end filter that is matched to the entire sequence, and the decision statistic for symbol detection is formed by the correlation value between the outputs of the two matched filters. The results reported show that the system signal-to-noise ratio (SNR) performance can be improved if despreading is done before correlation (or multiplication), unlike conventional AcRs, which operate in a reversed order.

1.3 Thesis Objectives

From the discussion of previous section, TR-IR appears to be an attractive low complexity solution for future short-range wireless communications. TR-IR with AcRs is able to exploit multipath diversity of UWB channel without the need of stringent time acquisition and channel estimation. Most proposed receivers for TR-IR only entail integrate and compare operations at the symbol rate. Furthermore, noncoherent detection using AcRs is robust to channel synchronization errors and pulse shape distortions.

Previous works on TR-IR mainly focus on peer to peer transmission. To the best of our knowledge, multiuser systems are only considered in [43], where the TR-IR incorporates pseudorandom spreading codes, similar to the CDMA system. However, CDMA scheme does not prevent signal collisions among different users. It only provides processing gain to combat the multiuser interference (MUI). In UWB channels, the signal energy is dispersed into hundreds of multipath components. Because of the exponential decay property of UWB channels, more than 80% of signal energy concentrates in the first arriving several tens of multipath components [44]. To prevent collisions of these multipath components transmitted from different users, an efficient method is to incorporate the TR-IR with the time-division multiple access (TDMA) scheme. The objective of our research is to develop a time-division (TD) multiuser IR system with AcR and study its performance in UWB channels.

We first design and analyze the system based on the assumption of perfect synchronization among users. This issue of synchronization is then studied where an algorithm which combines synchronization and power control is proposed. The

purpose of power control is to equalize the received powers from all users. This would improve the overall system BER by reducing MUI and assigning higher transmission power to users who experienced prolonged deep fade. The effects of low-density parity-check (LDPC) codes and space-time codes on the signal-to-noise ratio (SNR) performance of the proposed system are finally examined.

The design of time-shared multiuser IR generally involves the partition of a symbol into frames, and a frame into chips, where the chip length is chosen to be longer than the support length of a pulse. For a given user, the pulses representing a data symbol are each positioned at the beginning of a chip, with one pulse in each frame. Depending on the way that chips are assigned to users, the system may be classified as using time-division (TD) or time-hopping (TH) multiple access, or a hybrid of the two. The chip duration, which is inversely proportional to the data transmission rate, is a key design parameter of time-shared multiuser IR systems with AcRs. For example, choosing the chip duration much shorter than the maximum excess delay of an UWB channel would significantly increase the system transmission rate, however, it would induce multi-user interference (MUI). A practical approach for reducing MUI, especially for systems designed with short chip duration, is to randomize the interference, which is a characteristic of TH-IR.

In this thesis, we propose a differentially-encoded, di-symbol time-division multiuser impulse radio (d^2TD-IR) system with delay-sum AcR. The delay-sum AcR may be viewed as AcR with a front-end filter as in [37], which instead of being matched to the input coded pulse-sequence, is matched to an identically coded Dirac-δ impulse-sequence. Compared to matched filtering, the delay-sum scheme offers the advantage of lower computational complexity because despreading can be achieved through pulse-summation instead of pulse-convolution. The omission

of matched filtering may, however, lead to some loss in SNR performance.

To mitigate the ill-effects of MUI on the performance of differential detection, we employ two randomly generated TH access sequences to alternately encode the odd- and even-index symbols. Unlike TH-IR where the access sequence for a user changes randomly from symbol to symbol till the sequence recycle, the access sequence here remains fixed for alternate symbols, hence the name di-symbol TD multiple access.

In any time-division multiuser systems, timing synchronization among users is a crucial requirement. Originally conceptualized for infrastructure networks where transmissions can be synchronized by a central controller such as a base station or an access point, the idea has also been extended to ad-hoc networks [45–48].

For the proposed system, the wideband analog delay line is not an unfathomable problem [49, 50]. From the quantized analog delay line structure in [50], the time delay is equal to the duration of the analog signal stored in the batches of binary delay line. In our proposed system, the analog signal to be stored only has a chip duration which can be as short as several nanoseconds.

The proposed d^2TD-IR system is designed with the assumption that the users are perfectly synchronized. It is thus imperative to design an efficient synchronization algorithm to support this operating condition.

Synchronization algorithm for TR-IR has been studied in [51]. However, the algorithm is for single user system. Furthermore, considering a simplified UWB channel model with much shorter maximum excess delay, the authors ignored the effects of intersymbol interference (ISI) in their study. Therefore, our research objective is to modify the synchronization algorithm in [51] and make it applicable to our proposed d^2TD-IR system.

In the proposed d^{2}TD-IR system, the transmitted signals from different users undergo independent fadings. In this situation, power control, which ensures that each user provides almost the same signal power to the base station (BS) receiver, can maximally suppress the multiuser interference (MUI) and hence improve the system performance. Because both synchronization and power control processes require pilot symbols, it is preferable to combine the two processes. However, when two processes are combined, synchronization errors will cause larger power control errors and power control errors will cause larger synchronization errors. Error propagation between the two processes will cause system failure. In this thesis, we present an algorithm which combines the two processes and prevents error propagation.

As mentioned in Subsection 1.2.2, FCC prescribes that UWB systems transmit signal with extremely low power spectral density. To satisfy the requirement, the SNR performance of the proposed d^{2}TD-IR system should be increased as much as possible. This can be done with the help of powerful channel coding scheme. Low-density parity-check (LDPC) codes [52–55] are well known for their abilities to achieve near Shannon channel capacity limit and low decoding complexity compared with the Turbo decoder [56].

Low-density parity-check (LDPC) codes were originally invented and investigated by Gallager [52] in early 1960s. After being "shelved" for about 35 years, this class of codes had been recently rediscovered and shown to form another class of Shannon-limit approaching codes, besides turbo codes [56]. It was shown that a carefully constructed rate 1/2 irregular LDPC code with long block length has a bit error probability of 10^{-6} at just 0.13 dB away from Shannon capacity for AWGN channels [55].

Since the encoding complexity of LDPC codes increases with the square of the code length, a type of LDPC product codes is proposed in Appendix B, which significantly lowers the encoding complexity at the expense of slight degradation in bit-error-rate (BER) performance as well as slight increase in decoding complexity.

Thus motivated, we develop LDPC coded and LDPC product coded d^2TD-IR systems and evaluate their performances in UWB channels.

To increase the SNR performance of the proposed d^2TD-IR system, another method is to introduce spatial diversity, which efficiently combats the fading UWB channels. Spatial diversity can be achieved by multiple-input multiple-output (MIMO) scheme.

Insofar, to the best of our knowledge, research on TR-IR has always been focused on single-input-single-output (SISO) systems. For fading channels, the advantages of space-time codes have been well documented in multiple-input-multiple-output (MIMO) literature [57–63]. UWB channels are known to exhibit little to no fading when multipath energy is harnessed. In this case, multiple receive antennas will still provide an energy boost and thus improve system performance, whereas the amount of diversity gain that can be derived from multiple transmit antennas is generally expected to be minimal. The question of how well can a TR-IR/AcR system harness multipath energy to render multiple transmit antennas schemes ineffective remains open. In the work of Qui et al [64], it was experimentally shown that by using four fixed transmit antennas in their time-reversal UWB scheme, the channel impulse response measured by a mobile receive antenna exhibited a peak amplitude that was twice that of an equivalent system with only one transmit antenna. The UWB pulse used had a 10dB-bandwidth spanning for 700 MHz to 1.6 GHz, and an antenna array with elements spaced at 20 cm was found

to be sufficient to ensure no correlation between the elements. The time-reversal scheme in [64] may be viewed as a special case of transmitted-reference signaling with autocorrelation receiver, where the coupled data- and reference-pulse form a time-reversed pair.

MIMO UWB transmission schemes have been reported in [12, 64–67]. For example, Yang et al [66] proposed an analog space-time coding scheme, which extended the impulse radio to MIMO communications. As in [8], Yang et al employed a Rake receiver in their system. Also recently, Siriwongpairat et al [12] proposed a combination of space-time-frequency (STF) coding and hopping multiband orthogonal frequency division multiplexing (OFDM) modulation for MIMO UWB systems to exploit both spatial and frequency diversities.

Of interest then is to examine the performance gain that can be obtained from MIMO implementation of impulse radios when an autocorrelation based receiver structure is used to capture multipath energy. In this thesis, we propose a differential space-time coded (DSTC) MIMO d^2TD-IR system. For simplicity, the proposed system is considered in a peer-to-peer transmission scenario. Differential space-time codes (DSTC) similar to that described in [62] are used to provide additional diversity and coding gain [68]. The AcR, originally designed to harness multipath energy in SISO d^2TD-IR systems, is extended to MIMO systems.

The peer-to-peer DSTC MIMO scheme is then extended to the multiuser d^2TD-IR system where its performance is studied through computer simulations.

1.4 Thesis Outline

In Chapter 2, the conventional impulse radio system is reviewed. A general introduction to monocycles, modulations, UWB channel models, multiple access scheme and receivers is presented.

We propose a new scheme, which is called differentially-encoded di-symbol time-division multiuser impulse radio (d^2TD-IR) system, in Chapter 3. Its system performance and average capacity are derived. Based on that, a method for estimating the chip duration that maximizes the signal-to-interference-and-noise ratio, with only the knowledge of the channel power decay profile, is discussed. Finally, simulations and numerical results are presented and discussed.

In Chapter 3, the proposed d^2TD-IR system is studied with the assumption of perfect synchronization among users. For completeness of the whole system, we propose a time of arrival (TOA) based algorithm for synchronization in Chapter 4. Furthermore, a recursive algorithm which combines synchronization and power control is also discussed.

In Chapter 5, we examine the effects of LDPC codes and LDPC product codes on the performance of the d^2TD-IR system. The study is carried out through computer simulations.

For single user d^2TD-IR systems, we propose a DSTC MIMO scheme in Chapter 6. In the absence of intersymbol interference (ISI), a bit-error-rate (BER) expression is derived to predict the system performance. Based on the proposed system model, we study the design criteria for DSTC, which are somewhat different from those used in narrowband systems, and use these criteria to design maximum distance codes. To distinguish between diversity gain and coding gain contributed

by DSTC, we examine the performance of the proposed system when DSTC is replaced by differential repetition codes (DRC), which provide only diversity gain. The DSTC MIMO scheme is also implemented on the multiuser d^{2}TD-IR system, whose performance is studied through computer simulation.

Finally in Chapter 7, we conclude this thesis and propose some work for future study.

1.5 Thesis Contributions

Our main contribution in this thesis lies in the design and analysis of a new TDMA-based impulse radio system for UWB channels.

We designed the d^{2}TD-IR system with delay-sum AcR, which employs a hybrid of time-division (TD) and time-hopping (TH) multiple access scheme to suppress the multiuser interference (MUI). The delay-sum AcR, unlike the conventional AcRs, despreads the received signal before correlation (or multiplication). It may be viewed as AcR with a front-end filter which instead of being matched to the input coded pulse-sequence, is matched to an identically coded Dirac-δ impulse-sequence. Compared with TH-IR, the proposed system can achieve better performance at high signal-to-noise ratio (SNR).

We derived the BER and average capacity expressions for the d^{2}TD-IR system. From the results, we proposed a novel method for estimating the optimal chip duration, which is capable of achieving an accuracy to within 10% for 5 dB$<$ $E_b/N_o < 30$ dB by using only the UWB channel power decay profile. The chip duration is a key system design parameter.

The proposed d^{2}TD-IR system was designed with the assumption that signals

from different users are perfectly time synchronized. To realize the assumption, we proposed a combined synchronization and power control recursive algorithm to be used with the d^2TD-IR systems. Power control was incorporated into the algorithm to mitigate BER degradation due to MUI and occurrence of prolonged deep fade. The algorithm inherently avoids error propagation and is capable of achieving results close to the perfect situation.

Finally, we explored the effects of channel coding and diversity signaling on the BER performance of the d^2TD-IR system. For the channel coding, we employed LDPC codes, which is well known to be capable of achieving near Shannon's limit. Besides conventional LDPC codes, we also proposed a class of LDPC product codes which significantly reduces encoding complexity at the expense of slight increase in decoding complexity and slight degradation in BER compared to LDPC codes. For diversity signaling, we extended the d^2TD-IR system into a MIMO system. In the single user scenario, and when there is no intersymbol interference, we derived a close-form BER expression for the MIMO system. We also designed the maximum-distance codes based on group structure for any number of transmit antennas.

Chapter 2

Impulse Radio

UWB systems are capable of achieving reliable and high speed communication using low cost transceivers. One of the qualified candidates is impulse radio (IR), which transmits a train of short pulses (also called monocycles), usually with support length on the order of a nanosecond [8].

In this chapter, we first introduce the UWB monocycles and the different modulation schemes used in impulse radio. This is followed by a review of the channel model recommended by the Institute of Electrical and Electronics Engineers (IEEE) UWB standard committee [44]. Finally, we introduce the pulse position modulation (PPM)-based time-hopping impulse radio (TH-IR) [7, 8] to illustrate how an IR system is modeled. We have chosen TH-IR as an example since it will be used as a basis for performance comparison with our proposed IR systems.

2.1 Monocycles

A monocycle which can be generated easily is one with a bell shape such as a Gaussian monocycle [69]. However, a monocycle should have a zero direct current (DC) offset for it to be efficiently radiated. Therefore, Gaussian derivatives are suitable. Ideally, if the transmit antenna is fed with a monocycle shaped as the first derivative of a Gaussian waveform, a second derivative Gaussian monocycle can be obtained at the output of the antenna. When receiving, the antenna does not act as a differentiator on the incoming signal, but rather presents a flat frequency response [70]. Therefore, after passing through the transmit and receive antennas, the second derivative Gaussian function models the monocycle at the receiver. The second derivative Gaussian monocycle is the most extensively adopted monocycle [8], and is described by

$$\omega(t) = \left[1 - 4\pi(t/\tau_m)^2\right] \exp\left[-2\pi(t/\tau_m)^2\right], \tag{2.1}$$

whose waveform and spectrum are shown in Fig. 2.1, in which $\tau_m = 0.2877$ ns.

Monocycles which have the shapes of Gaussian derivatives do not fully comply with the FCC power spectral mask for UWB systems. To comply with the mask, Parr et al [71] proposed an algorithm to generate the monocycles numerically. The algorithm uses the samples of the corresponding impulse response of the spectral mask to form a Toeplitz matrix, whose dominant eigenvectors are suggested for the shape of monocycles . Monocycles corresponding to different eigenvectors are mutually orthogonal. Furthermore, to achieve the optimal spectral utilization, Wu et al proposed a synthetic monocycle which is generated by passing a convenient basis monocycle, such as a Gaussian monocycle, through digital finite impulse

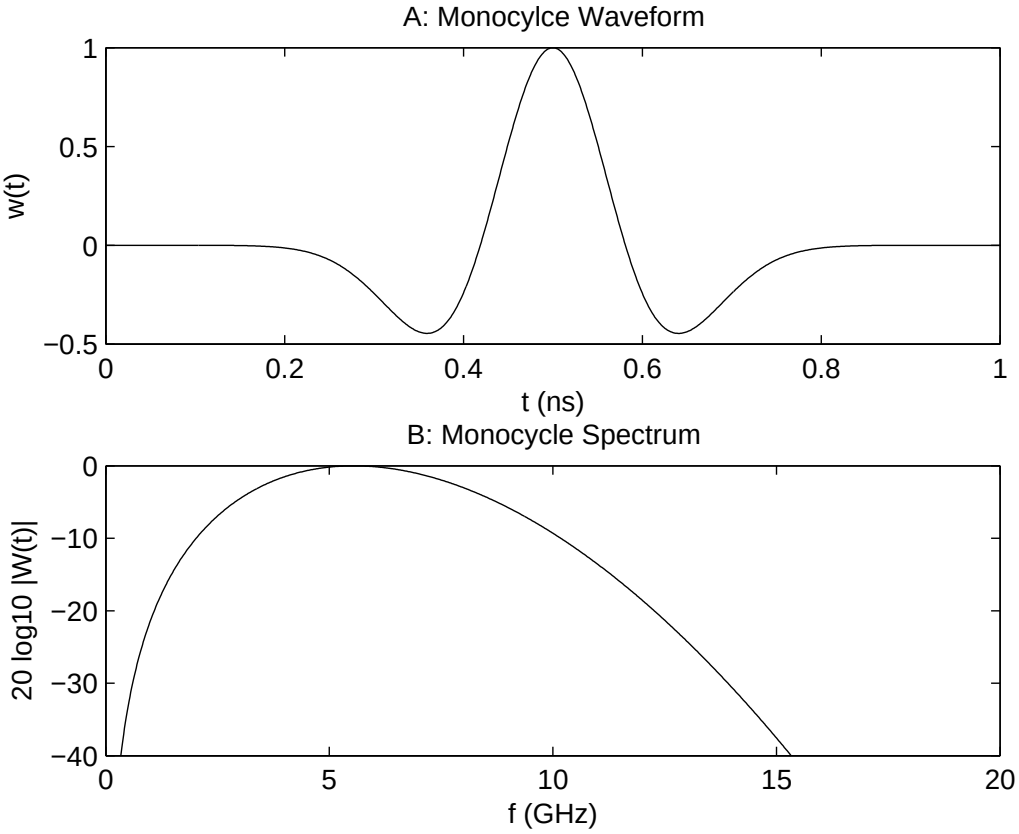

Fig. 2.1: The second derivative Gaussian monocycle waveform and spectrum.

response (FIR) filters [72].

2.2 Modulations

The modulation scheme for impulse radio signaling can be one of pulse position modulation (PPM), pulse amplitude modulation (PAM), on-off keying (OOK), and pulse shaping modulation (PSM). In this context, the transmitted signal of the

impulse radio system can generally be written as [21]

$$s(t) = \sum_j \alpha_j \omega^{(\gamma_j)}(t - \delta_D \beta_j) \tag{2.2}$$

where the index j indicates the frame number, $\omega(t)$ represents the transmitted monocycle and δ_D is the monocyle shift unit if the modulation is PPM. Within each frame, α_j controls the amplitude of the monocycle, β_j the monocycle position and γ_j the monocylce shape. By varying α_j, β_j or γ_j according to the data symbol, we achieve OOK/PAM, PPM or PSM. These are illustrated in Fig. 2.2.

The above modulations are introduced for the binary case. However, PPM, PAM and PSM are not restricted to the binary case. M-ary PPM, PAM and PSM were discussed in [73–77].

2.3 UWB Channel Models

Different from the traditional channels, such as additive white Gaussian noise (AWGN) channel, Rayleigh fading channel and Rician fading channel, the indoor UWB channel may have as many as several hundreds of resolvable paths. In contrast to dense multipath contributions, these paths exist individually over distances larger than a wave length. Various models were proposed for UWB channels in [44, 78–81]. These models are basically formulated based on field tests and measurements. Of interest is the channel model recommended by the IEEE UWB standard committee [44], which we employ in our subsequent studies.

In the IEEE UWB channel model [44], the free space path loss model for large-scale fading is adopted. Based on the clustering phenomenon observed in several

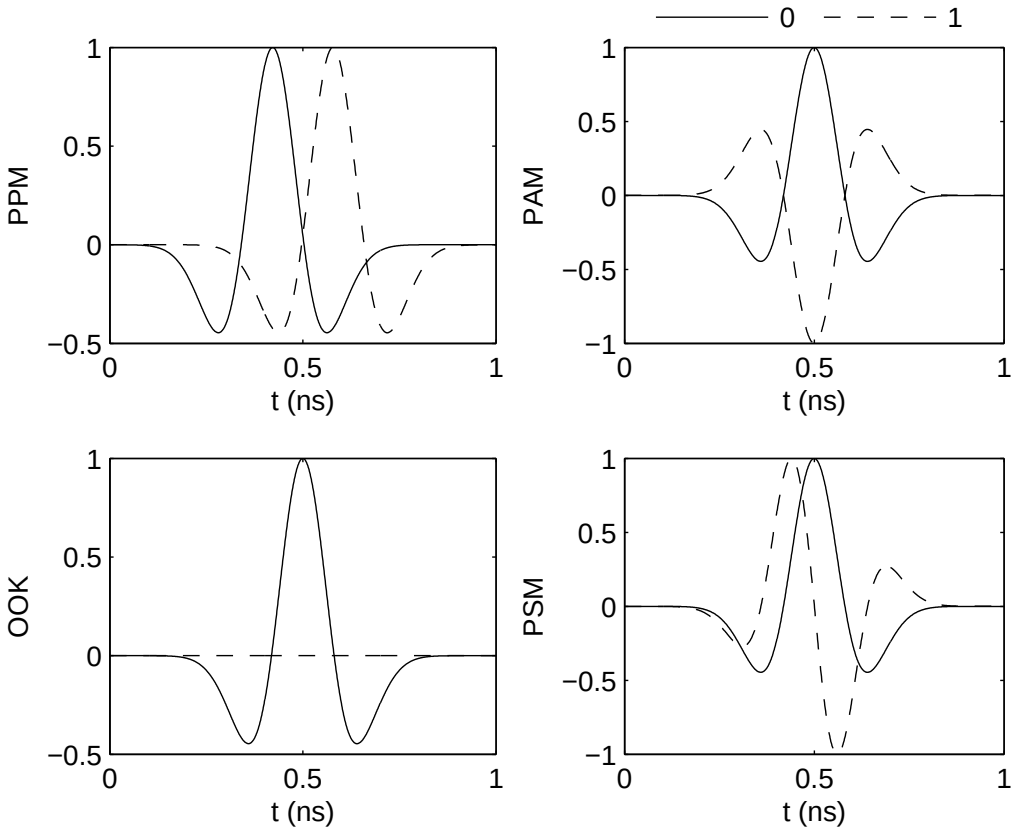

Fig. 2.2: Different modulations of impulse radio systems.

channel measurements, the multipath model for small-scale fading was derived from the S-V model [81] with a couple of slight modifications. Since observations showed that the lognormal distribution seems to better fit the measurement data, a lognormal distribution rather than a Rayleigh distribution for the multipath gain magnitude was suggested. In addition, independent fading is assumed for each cluster as well as each ray within the cluster. Therefore, the multipath model

consists of the following impulse response

$$g(t) = X \sum_{l=0}^{L} \sum_{k=0}^{K} \alpha_{k,l} \delta(t - T_l - \tau_{k,l}) \tag{2.3}$$

where $\alpha_{k,l}$ is the multipath gain coefficient, T_l is the delay of the l^{th} cluster, $\tau_{k,l}$ is the delay of the k^{th} ray relative to the l^{th} cluster arrival time T_l, and X represents the log-normal shadowing.

Let Λ and λ denote the cluster and the ray arrival rates, respectively. With $\tau_{0,l} = 0$ (by definition), the distribution of T_l and $\tau_{k,l}$ are given by

$$p(T_l \,|T_{l-1}) = \Lambda \exp\left[-\Lambda(T_l - T_{l-1})\right], \; l > 0; \tag{2.4}$$

$$p(\tau_{k,l}|\tau_{(k-1),l}) = \lambda \exp\left[-\lambda(\tau_{k,l} - \tau_{(k-1),l})\right], \; k > 0. \tag{2.5}$$

The multipath gain coefficient $\alpha_{k,l}$ is defined as

$$\alpha_{k,l} = p_{k,l} \xi_l \beta_{k,l} \tag{2.6}$$

where $p_{k,l}$ is equiprobable ± 1 to account for signal inversion due to reflections, ξ_l reflects the fading associated with the l^{th} cluster, and $\beta_{k,l}$ corresponds to the fading associated with the k^{th} ray of the l^{th} cluster. The $\xi_l \beta_{k,l}$ is given by

$$\xi_l \beta_{k,l} = 10^{(\mu_{k,l} + n_1 + n_2)/20} \tag{2.7}$$

where n_1 and n_2 are independent Gaussian random variables with zero means and variances σ_1^2 and σ_2^2, respectively. In the above equation, n_1 corresponds to the fading on each cluster and n_2 corresponds to the fading on each ray.

The $\mu_{k,l}$ is given by

$$\mu_{k,l} = \frac{10 \ln \Omega_0 - 10T_l/\Gamma - 10\tau_{k,l}/\gamma}{\ln 10} - \frac{(\sigma_1^2 + \sigma_2^2) \ln 10}{20} \tag{2.8}$$

where Ω_0 is the mean energy of the first path of the first cluster, Γ is the cluster decay factor, and γ is the ray decay factor.

Note that, a complex tap model is not adopted here. The complex baseband model is a natural fit for narrowband systems to capture channel behavior independent of carrier frequency, but this motivation breaks down for UWB systems where a real-valued simulation may be more natural.

Finally, since the log-normal shadowing of the total multipath energy is captured by the term, X, the total energy contained in the terms $\{\alpha_{k,l}\}$ is normalized to unity for each realization. This shadowing term is characterized by

$$X = 10^{n_x/20} \tag{2.9}$$

where n_x is a Gaussian random variable with zero mean and variance σ_x^2.

Based on the general model, four types of channel models (CM) have been specified: CM 1, 0∼4 meters' range with line-of-sight (LOS); CM 2, 0∼4 meter's range with non-line-of-sight (NLOS); CM 3, 4∼10 meters' range, NLOS; and CM 4, greater than 10 meter's range, NLOS. Table 2.1 lists the measurement data associated with the parameters for these four channel models.

Fig. 2.3 - 2.6 show the typical channel impulse response realization of CM 1-4.

Model Parameters	CM 1	CM 2	CM 3	CM 4
Λ (1/ns)	0.0233	0.4	0.0667	0.0667
λ (1/ns)	2.5	0.5	2.1	2.1
Γ (ns)	7.1	5.5	14.00	24.00
γ (ns)	4.3	6.7	7.9	12
σ_1 (dB)	3.3941	3.3941	3.3941	3.3941
σ_2 (dB)	3.3941	3.3941	3.3941	3.3941
σ_x (dB)	3	3	3	3

Table 2.1: UWB channel model parameters.

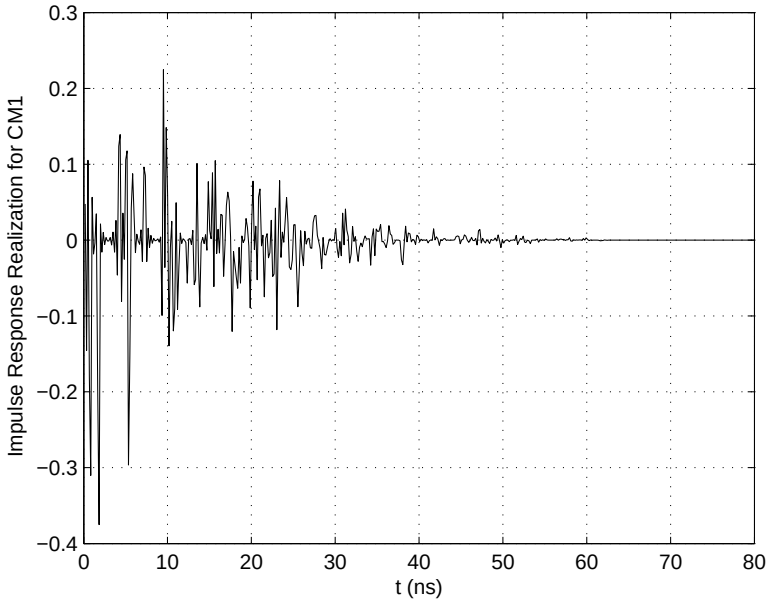

Fig. 2.3: Typical channel response of CM 1.

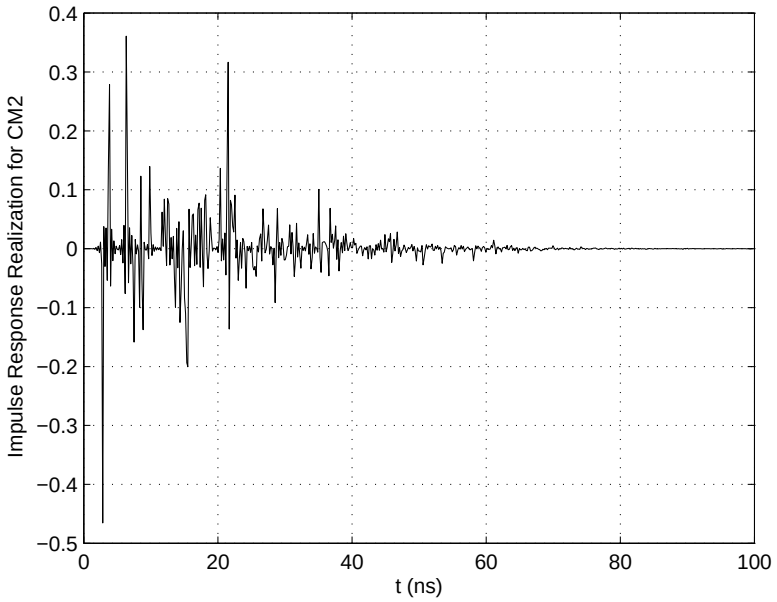

Fig. 2.4: Typical channel response of CM 2.

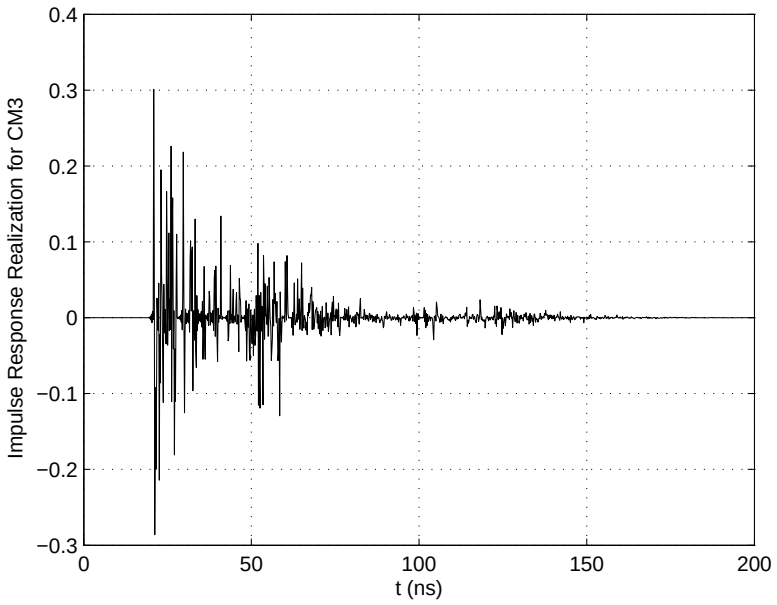

Fig. 2.5: Typical channel response of CM 3.

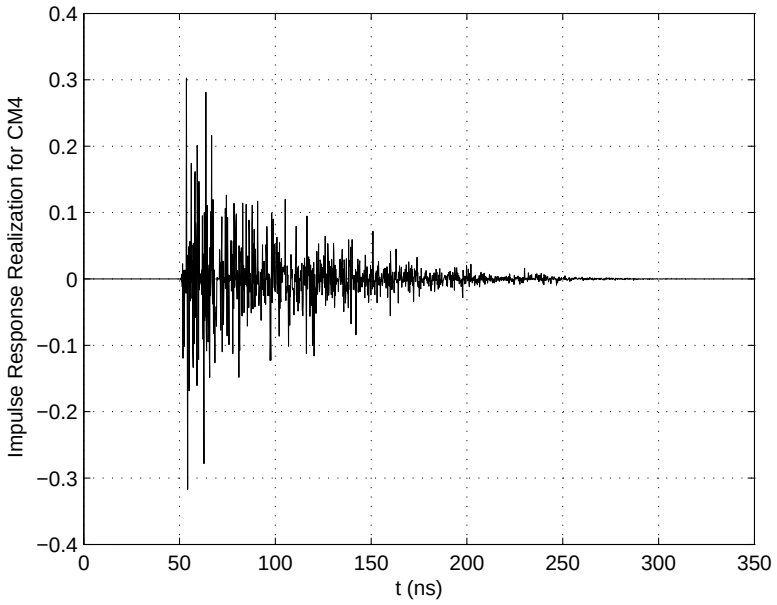

Fig. 2.6: Typical channel response of CM 4.

2.4 PPM-Based Time-Hopping Impulse Radio

In this section, we take the PPM-based time-hopping impulse radio (TH-IR) as an example to explain how an impulse radio system is modeled.

In TH-IR system, every user sends N_s monocycles for each data bit. These monocycles are located apart in sequential frames, each with duration T_f. Because the PPM is used here, the monocycles corresponding to bit 1 are sent δ_D seconds later than the monocycles corresponding to bit 0. The locations of the monocycles in each frame are determined by a user dedicated pseudorandom sequence. The transmitted signal of the k^{th} user is

$$s^{(k)}(t) = \sum_j \omega(t - jT_f - c_j^{(k)} T_c - \delta_D d_j^{(k)}) \tag{2.10}$$

where $\{c_j^{(k)}\}$ is the dedicated pseudorandom sequence for the k^{th} user with integer components. The integer number can take on any value between zero and $N_h - 1$. T_c indicates chip duration and satisfies $N_h T_c \leq T_f$. In (2.10), $\{d_j^{(k)}\}$ is the binary sequence of the transmitted symbols corresponding to user k. This sequence is N_s repetitions of the transmitted data sequence, i.e., if the transmitted binary data sequence is $\{b_i^{(k)}\}$, then we have $d_j^{(k)} = b_i^{(k)}$ for $iN_s \leq j < (i+1)N_s$.

When N_u users are active in the multiple access system, the composite received signal $r(t)$ at the output of this receiver antenna is modeled as

$$r(t) = \sum_{k=1}^{N_u} s^{(k)}(t) \otimes g^{(k)}(t) + n(t) \tag{2.11}$$

where $\otimes$ denotes convolution operation and $g^{(k)}(t)$ is the channel impulse response of k^{th} user.

By assuming that one dominant path exists that conveys the major part of the desired user's energy, Win [8] proposed a simplified model describing the impulse radio multiple access receiver shown in Fig. 2.7. In the figure, the receiver is perfectly locked to the signal from the first user. The received signal $r(t)$ at the output of this receiver antenna can be simplified to

$$r(t) = \sum_{k=1}^{N_u} \alpha^{(k)} s^{(k)}(t - \tau^{(k)}) + n(t) \tag{2.12}$$

where $\alpha^{(k)}$ and $\tau^{(k)}$ models amplitude and delay of the signal $s^{(k)}(t)$ received from the k^{th} user, respectively.

If no other users except the first user were present, the optimum receiver is

the correlation receiver. The correlation receiver implements

$$D_i^{(1)} : \begin{cases} > 0; \text{ decide } b_i^{(1)} = +1 \\ \leq 0; \text{ decide } b_i^{(1)} = -1 \end{cases} \tag{2.13}$$

where the decision statistics $D_i^{(1)}$ is given by

$$D_i^{(1)} = \sum_{j=iN_s}^{(i+1)N_s-1} \int_{\tau^{(1)}+jT_f}^{\tau^{(1)}+(j+1)T_f} r(t)v(t-\tau^{(1)}-jT_f-c_j^{(1)}T_c)dt \tag{2.14}$$

in which

$$v(t) = \omega(t) - \omega(t-\delta_D). \tag{2.15}$$

When other users are present, strictly speaking, the above decision rule is no longer optimum. In the presence of multiuser interference (MUI), which is not really Gaussian, the optimum receiver makes use of the information about the structure of MUI. This detection in a multiuser environment leads to much more complex receiver designs [82]. However, if the number of users is large and no such multiuser detector is feasible, then it is reasonable to approximate the combined effect of the other users as a Gaussian random process [18]. Under this approximation, the total noise which includes MUI and channel noise, is a spectrally white Gaussian random process and such decision rule is optimum.

The above simplest receiver is obtained by assuming that a dominant path exists that conveys the major part of the desired user's energy. This receiver may be viewed as a Rake receiver with a single finger (Rake-1). Note that, although Rake-1 needs to know the strongest path and the associated delay, it is not concerned with the actual value of the path gain. When multipath UWB channel is considered, a

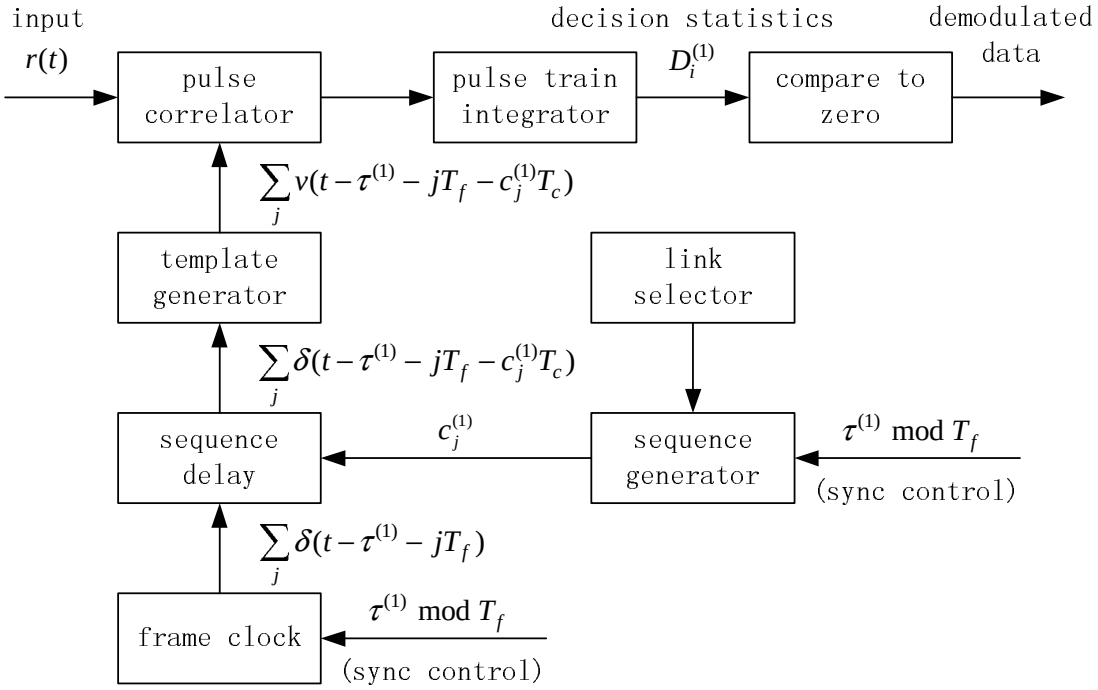

Fig. 2.7: Receiver block diagram of TH-IR system in flat fading channel.

more efficient receiver is the Rake receiver with L fingers (Rake-L).

Assuming the first user to be the user of interest, the block diagram of a Rake receiver with L fingers (Rake-L) is depicted in Fig. 2.8. The decision statistics is now the maximal-ratio combination of the correlators' outputs

$$D_i^{(1)} = \sum_{l=1}^{L} \alpha_l^{(1)} \left\{ \int_{\tau_l^{(1)}+iT_s}^{\tau_l^{(1)}+(i+1)T_s} r(t) \sum_{j=iN_s}^{(i+1)N_s-1} v(t-\tau_l^{(1)}-jT_f-c_j^{(1)}T_c)dt \right\}. \quad (2.16)$$

In practice, the parameters $\{\alpha_l^{(1)}\}$ and $\{\tau_l^{(1)}\}$ are not known a priori and must be estimated. The problem was addressed in [23], where Lottici derived data-aided and non data-aided channel parameter estimate algorithms for the Rake receiver. Because a typical UWB channel generally has several hundred multipath com-

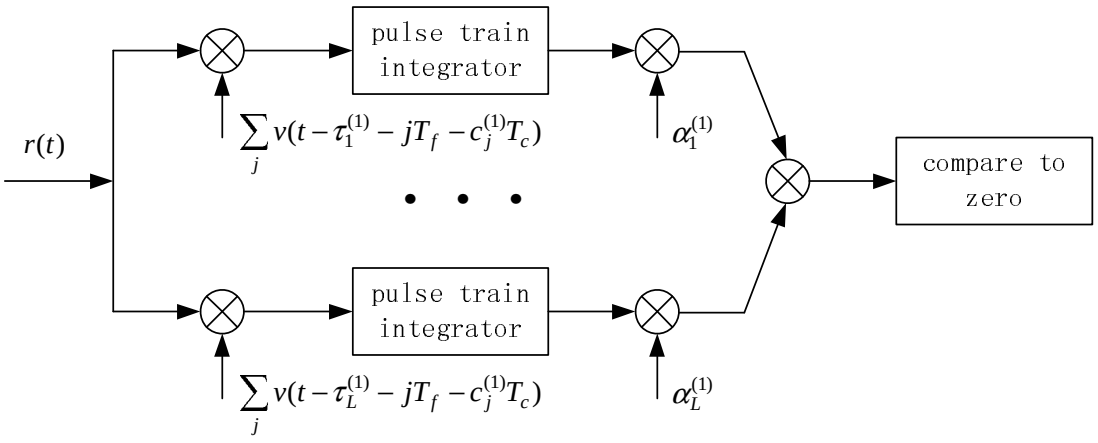

Fig. 2.8: Rake receiver block diagram of TH-IR system in multipath UWB channel.

ponents, to reduce system complexity, Cassioli proposed a partial Rake (PRake) receiver, which combines the first arriving paths [83]. It was shown in [83] that when compared with an All-Rake (ARake) receiver which combines all of the resolvable multipath components and a selective Rake (SRake) receiver which selects the best paths out of the available paths, the PRake receiver seems to provide a good tradeoff between receiver performance and complexity. The author argued that the performance of the PRake receiver with a number of fingers greater than four is similar to those achievable by using a SRake with the same number of fingers.

In previous works, MUI was considered as a white Gaussian random process. To exploit MUI, an iterative ("Turbo") multiuser detection (MUD) method, which achieves good system performance as well as maintains low receiver complexity, was proposed in [84]. The detection process is split into two stages. The first stage is called "pulse detector", the other called "bit detector". The extrinsic information is exchanged between the two parts until the converged results are obtained. It was

reported that its performance approaches that of a single user system after several iterations.

2.5 Summary

In this chapter, key ingredients for an impulse radio (IR) system, such as monocycles, modulations and UWB channel models, were reviewed. The PPM-based TH-IR was discussed in detail to illustrate how an impulse radio system is modeled.

From the analysis of PPM-based TH-IR in 2.4, we note that coherent detection of impulse radio signals requires precise time acquisition, which is a very challenging problem considering the ultra-short duration of the monocycles. Another alternative, which is less sensitive to time acquisition, is transmitted-reference impulse radio (TR-IR) employing AcR. As an improved version of conventional TR-IR, a differentially-encoded di-symbol time-division multiuser impulse radio (d^2TD-IR) system will be proposed in the next chapter.

Chapter 3

Differentially-Encoded Di-Symbol Time-Division Multiuser Impulse Radio

---

Previous works on TR-IR (including differential TR-IR) focus on peer-to-peer transmission. In a multiuser scenario, TR-IR employing efficient multiple access schemes has not been fully explored, especially in a time-division multiple access (TDMA) framework. In this chapter, we propose a differentially-encoded di-symbol time-division multiuser impulse radio (d^2TD-IR) system with delay-sum AcR for an infrastructure network.

In Section 3.1, we first describe the proposed d^2TD-IR system model. Then, we derive the system bit-error-rate (BER) formula based on a general UWB channel model, where the multiuser interference (MUI) is treated as Gaussian noise [8]. Through the BER analysis, the system average capacity [36] is derived. In

Section 3.3, a method for estimating the chip duration that maximizes the signal-to-interference-and-noise ratio, with only the knowledge of the channel power decay profile, is discussed. Finally, new theoretically predicted and computer simulated results are presented and discussed.

3.1 System Description

We consider an N_u-user d^{2}TD-IR system signaling through multipath UWB channel, where each user employs binary pulse amplitude modulation (PAM).

3.1.1 The Transmitter

Let $\cdots b_{-1}^{(k)} b_0^{(k)} b_1^{(k)} b_2^{(k)} \cdots$ denote the sequence of independent and identically distributed (iid) information symbols sent by the k^{th} user in the proposed system, where $b_i^{(k)} \in \{-1, 1\}$. The $b_i^{(k)}$'s are first differentially encoded into another symbol sequence $\cdots d_{-1}^{(k)} d_0^{(k)} d_1^{(k)} d_2^{(k)} \cdots$, where $d_i^{(k)} = (b_i^{(k)} d_{i-1}^{(k)}) \in \{-1, 1\}$, and then transmitted using N_s non-overlapping monocycles per symbol. To incorporate multiple access capability into the system, we divide each symbol interval of duration T into N_s frame intervals, further divide each frame interval into N_h chip intervals where N_h is the maximum number of users the system can support. The signal model for user k then has the form

$$s^{(k)}(t) = \sum_i \sum_{j=0}^{N_s-1} d_i^{(k)} a_{i \bmod 2,j}^{(k)} \omega(t - iT - jT_f - c_{i \bmod 2,j}^{(k)} T_c) \tag{3.1}$$

where $T_f = T/N_s$ is the frame duration, $T_c = T_f/N_h$ the chip duration, and $\omega(t)$ is a causal monocycle of support length $T_\omega < T_c$. In (3.1), the $a_{i \bmod 2,j}^{(k)}$

and $c^{(k)}_{i \bmod 2,j}$ are randomly drawn from the sets $\{-1, 1\}$ and $\{0, 1, \cdots, N_u - 1\}$, respectively, with the constraint that $c^{(k)}_{i \bmod 2,j} \neq c^{(k')}_{i \bmod 2,j} : k \neq k'$. Therefore, $[a^{(k)}_{0,0} c^{(k)}_{0,0} a^{(k)}_{0,1} c^{(k)}_{0,1} \cdots a^{(k)}_{0,N_s-1} c^{(k)}_{0,N_s-1}]$ and $[a^{(k)}_{1,0} c^{(k)}_{1,0} a^{(k)}_{1,1} c^{(k)}_{1,1} \cdots a^{(k)}_{1,N_s-1} c^{(k)}_{1,N_s-1}]$ form the multiple access code sequences assigned to the even- and odd-index symbols of user k. By alternating the two code sequences in this manner randomizes the channel-induced interference experienced by any two adjacent symbols, which in turn improves the average performance of the proposed delay-sum AcR. An example of the structure of $s^{(k)}(t)$ is shown in Fig. 3.1. In the analysis to follow, we consider the full load situation where $N_h = N_u$.

3.1.2 The Channel Model

In our study, we consider a time-invariant, independent UWB channel for each user. The random channels are generated according to [44]. The channel model for user k can be written, in general, as

$$g^{(k)}(t) = \sum_{l=1}^{L^{(k)}} \alpha_l^{(k)} \delta(t - \tau_l^{(k)}) \tag{3.2}$$

where $L^{(k)}$ denotes the number of propagation paths, and $\alpha_l^{(k)}$ and $\tau_l^{(k)}$ denote, respectively, the amplitude and the delay associated with the l^{th} path. We begin by assuming that the signals arriving at the receiver are perfectly time-synchronized at chip-level, and the path delays are normalized with $\tau_1^{(\cdot)} = 0$ for the desired user. Later we shall show that the proposed system performs better than the TH-IR system for cases of imperfect timing synchronization.

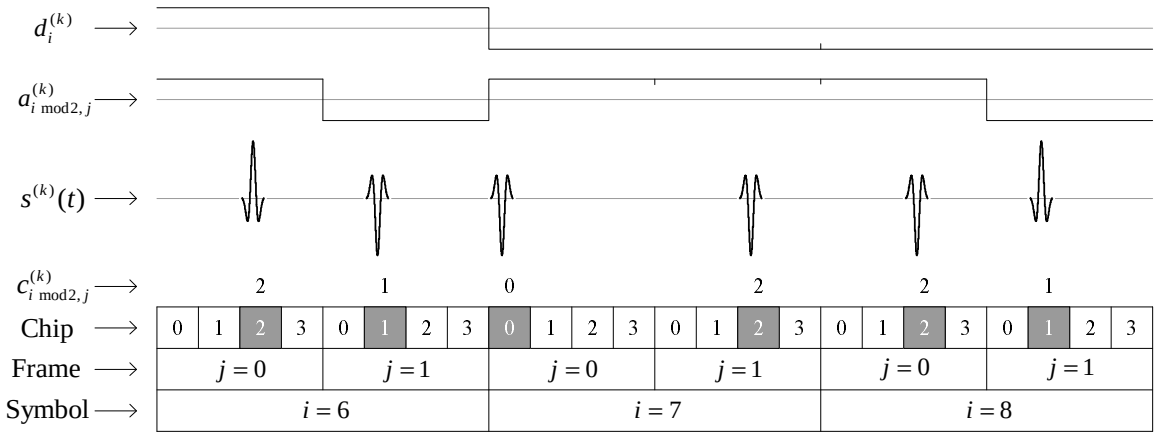

Fig. 3.1: Example of d^2TD-IR signaling $s^{(k)}(t) : 6T < t \leq 9T$ for $N_h = N_u = 4$, $N_s = 2$, system with $a^{(k)}_{0,0} = 1, a^{(k)}_{0,1} = -1, a^{(k)}_{1,0} = 1, a^{(k)}_{1,1} = 1$ and $c^{(k)}_{0,0} = 2, c^{(k)}_{0,1} = 1, c^{(k)}_{1,0} = 0, c^{(k)}_{1,1} = 2$.

The received signal due to user k is thus given by

$$r^{(k)}(t) = \sum_{i} \sum_{j=0}^{N_s-1} d_i^{(k)} a^{(k)}_{i \bmod 2,j} h^{(k)}(t - iT - jT_f - c^{(k)}_{i \bmod 2,j} T_c) \tag{3.3}$$

where

$$h^{(k)}(t) = \omega(t) \otimes g^{(k)}(t) = \sum_{l=1}^{L^{(k)}} \alpha_l^{(k)} \omega(t - \tau_l^{(k)}) \tag{3.4}$$

in which $\otimes$ denotes convolution. The composite received signal then has the form

$$r(t) = \sum_{k=1}^{N_u} r^{(k)}(t) + n(t) \tag{3.5}$$

where $n(t)$ is lowpass filtered additive white Gaussian noise (AWGN) with two-sided power spectral density $N_o/2$. The autocorrelation function of $n(t)$ is

$$R_n(\tau) = \mathrm{E}[n(t)n(t+\tau)] = N_o W \mathrm{sinc}(W\tau) \tag{3.6}$$

where W ($W \gg 1/T_c$) is the bandwidth of the lowpass filter. The ratio E_b/N_o of the system is defined as $\frac{N_s}{N_o}\int_0^{T_\omega}\omega^2(t)dt$.

3.1.3 The Receiver

Assuming that the receiver is locked on to the signal from user k, the proposed delay-sum AcR implements

$$D_i^{(k)}:\begin{cases} > 0;\ \text{decide } b_i^{(k)} = +1 \\ \leq 0;\ \text{decide } b_i^{(k)} = -1 \end{cases} \tag{3.7}$$

where the decision statistics $D_i^{(k)}$ is given by

$$D_i^{(k)} = \int_{(i+1)T-T_c}^{(i+1)T} x_{i \bmod 2}^{(k)}(t)\, x_{(i-1) \bmod 2}^{(k)}(t-T)dt, \tag{3.8}$$

in which

$$x_{i \bmod 2}^{(k)}(t) = \sum_{j=0}^{N_s-1} a_{i \bmod 2,j}^{(k)} r(t-(N_s-1-j)T_f - (N_u-1-c_{i \bmod 2,j}^{(k)})T_c). \tag{3.9}$$

The underlying mechanism of (3.8), with (3.9), can be briefly explained as follows. Each of the N_s frames, indexed by ($j = 0, 1, \cdots, N_s-1$), of the received i^{th} symbol is first multiplied with the respective $a_{i \bmod 2,j}^{(k)}$, and then delayed based on $c_{i \bmod 2,j}^{(k)}$ so that their monocycle-carrying chips are aligned. The aligned monocycle-carrying chips are summed up to form a composite chip. This is then aligned and multiplied with the composite chip of the previously received $(i-1)^{th}$ symbol, and the product is integrated over one chip duration to generate the value of $D_i^{(k)}$. A simplified model describing the receiver structure is shown in Fig. 3.2.

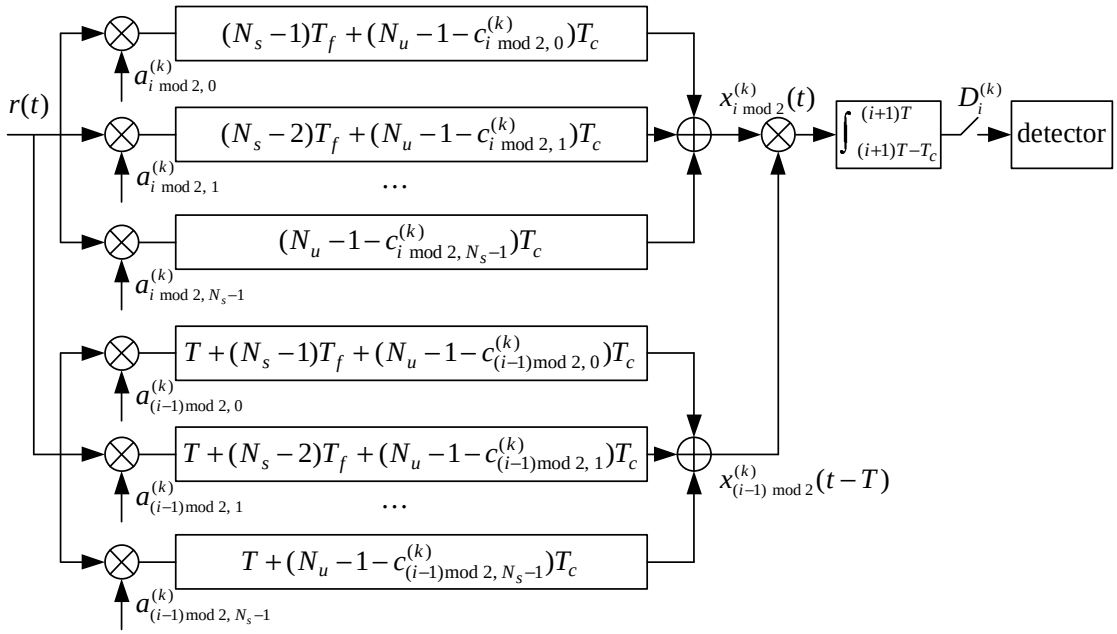

Fig. 3.2: The d^{2}TD-IR receiver block diagram for the k^{th} user.

3.2 Average Capacity and Bit-Error-Probability

The concept of average capacity is used in [36] to provide a metric for both performance and information rate achievable by a communication system. Here, we adopt this concept to our proposed multiuser d^{2}TD-IR system by defining the average capacity as the maximum information rate that each user can achieve in a symbol duration $T = N_u N_s T_c$. In this section, mathematical formulas for predicting the system BER and system average capacity are derived.

Begin by assuming that the channel impulse response has a finite memory length such that $h^{(k)}(t) = 0$ when $t > MT_c$, where M is a positive integer. We may then partition $h^{(k)}(t)$ into M contiguous time slices of duration T_c, and express

each slice as

$$h_m^{(k)}(t) = h^{(k)}(t)\,\tilde{p}\,(t-(m-1)\,T_c)\,;\ m = 1, 2, \cdots, M \tag{3.10}$$

where

$$\tilde{p}\,(t) = \begin{cases} 1;\ 0 \le t < T_c \\ 0;\ \text{otherwise.} \end{cases} \tag{3.11}$$

Let the signal from the first user be the desired signal and denote a user who transmits signal at $m-1$ chip durations before the j^{th} frame of i^{th} symbol of the first user as $v_{m,i \bmod 2,j}$. At the receiver, the sum of N_s received chips of the first user within the time interval $(i+1)T - T_c$ to $(i+1)T$ can be expressed as

$$x_{i \bmod 2}^{(1)}(t + (i+1)T - T_c) = A_i + B_i + C_i \tag{3.12}$$

where A_i, B_i and C_i are defined as follows:

$$A_i := N_s d_i^{(1)} h_1^{(1)}(t), \tag{3.13}$$

$$B_i := \sum_{j=0}^{N_s-1} \sum_{m=2}^{M} \gamma_{m,i,j} h_m^{(v_{m,i \bmod 2,j})}(t), \tag{3.14}$$

$$C_i := \begin{cases} \sum_{j=0}^{N_s-1} a_{i \bmod 2,j}^{(1)} n(t + \beta_{i,j}^{(1)}); & 0 < t \le T_c \\ 0; & t \le 0 \text{ or } t > T_c. \end{cases} \tag{3.15}$$

In (3.13 - 3.15),

$$\beta_{i,j}^{(1)} = iT + jT_f + c_{i \bmod 2,j}^{(1)} T_c \tag{3.16}$$

and

$$\gamma_{m,i,j} = d^{(v_{m,i \bmod 2,j})}_{i+\lfloor (jN_u + c^{(1)}_{i \bmod 2,j} - m+1)/(N_u N_s) \rfloor} a^{(1)}_{i \bmod 2,j} \\ a^{(v_{m,i \bmod 2,j})}_{i+\lfloor (jN_u + c^{(1)}_{i \bmod 2,j} - m+1)/(N_u N_s) \rfloor \bmod 2, j+\lfloor (c^{(1)}_{i \bmod 2,j} - m+1)/N_u \rfloor \bmod N_s} \tag{3.17}$$

where $\lfloor \bullet \rfloor$ denotes integer floor. From (3.8), we have

$$D_i^{(1)} = \int_0^{T_c} x^{(1)}_{i \bmod 2}(t + (i+1)T - T_c)\, x^{(1)}_{(i-1) \bmod 2}(t + iT - T_c)\, dt \tag{3.18}$$

where $D_i^{(1)} = z_d + z_I + u$ can be expressed as the superposition of three terms

$$z_d := A_i \circ A_{i-1}, \tag{3.19}$$

$$z_I := A_i \circ B_{i-1} + B_i \circ A_{i-1} + B_i \circ B_{i-1}, \tag{3.20}$$

$$u := (A_i + B_i) \circ C_{i-1} + C_i \circ (A_{i-1} + B_{i-1}) + C_i \circ C_{i-1} \tag{3.21}$$

in which $\circ$ denotes inner product. In (3.19 - 3.21), z_d is the desired signal; z_I represents the interference component that comes from MUI; and u is the noise component. It can be shown that these three terms are all zero mean and uncorrelated with one another.

First we consider the signal component, z_d, where the expression in (3.19) can be reduced to

$$z_d = b_i^{(1)} N_s^2 \int_0^{T_c} \left(h_1^{(1)}(t) \right)^2 dt. \tag{3.22}$$

Because $b_i^{(1)} \in \{-1, 1\}$, the absolute value of the desired signal z_d is

$$|z_d| = N_s^2 \mathcal{E}_1^{(1)} \tag{3.23}$$

where $\mathcal{E}_m^{(k)} := \int_0^{T_c} \left(h_m^{(k)}(t)\right)^2 dt$ captures the energy of $h_m^{(k)}(t)$.

Next, we consider the interference component, z_I. From (3.13 - 3.14) and (3.20), we know that

$$A_i \circ B_{i-1} = \sum_{j=0}^{N_s-1} \sum_{m=2}^{M} d_i^{(1)} \gamma_{m,i-1,j} N_s h_1^{(1)}(t) \circ h_m^{(v_{m,i-1 \bmod 2,j})}(t), \tag{3.24}$$

$$B_i \circ A_{i-1} = \sum_{j=0}^{N_s-1} \sum_{m=2}^{M} d_{i-1}^{(1)} \gamma_{m,i,j} N_s h_1^{(1)}(t) \circ h_m^{(v_{m,i \bmod 2,j})}(t), \tag{3.25}$$

$$B_i \circ B_{i-1} = \sum_{j_1=0}^{N_s-1} \sum_{j_2=0}^{N_s-1} \sum_{m_1=2}^{M} \sum_{m_2=2}^{M} \gamma_{m_1,i,j_1} \gamma_{m_2,i-1,j_2} h_{m_1}^{(v_{m_1,i \bmod 2,j_1})}(t) \circ h_{m_2}^{(v_{m_2,i-1 \bmod 2,j_2})}(t). \tag{3.26}$$

From (3.24 - 3.26), z_I is the sum of $2MN_s + M^2N_s^2$ random items. From central limit theorem, z_I can be approximated as a Gaussian random variable for cases when $N_s \gg 1$. The conditional variance of z_I is

$$\mathrm{Var}\left[z_I|\xi,\zeta\right] = \mathrm{E}_\eta\left[z_I^2\right] \tag{3.27}$$

where $\mathrm{Var}[\bullet]$ denotes the variance of $[\bullet]$, and $\mathrm{E}_\chi[\bullet]$ denotes the expected value of $[\bullet]$ taken over the random variable χ. In (3.27), ξ represents $\{v_{m,0,j}$ and $v_{m,1,j}; m = 1,2,\cdots,M; j = 0,1,\cdots,N_s-1\}$, ζ represents $\{h^{(k)}(t); k = 1,2,\cdots,N_u\}$ and η represents $\{d_i^{(k)}; k = 2,3,\cdots,N_u; i = \cdots,-1,0,1,2,\cdots\}$. From (3.17), $\{\gamma_{m,i,j}\}$

are independent and with zero mean. Therefore, we have

$$\begin{aligned}\mathrm{Var}\left[z_I|\xi,\zeta\right] = N_s^2 \sum_{i=0}^{1}\sum_{j=0}^{N_s-1}\sum_{m=2}^{M}\left(h_1^{(1)}(t)\circ h_m^{(v_{m,i,j})}(t)\right)^2 \\ + \sum_{j_1=0}^{N_s-1}\sum_{j_2=0}^{N_s-1}\sum_{m_1=2}^{M}\sum_{m_2=2}^{M}\left(h_{m_1}^{(v_{m_1,0,j_1})}(t)\circ h_{m_2}^{(v_{m_2,1,j_2})}(t)\right)^2.\end{aligned} \tag{3.28}$$

Finally, we consider the noise component, u. Based on (3.13 - 3.15), we know that the first two terms in (3.21) are Gaussian. The third term is the integral of the product of two uncorrelated Gaussian processes, which can be seen as approximately Gaussian from the central limit theorem. Therefore, using the same approach as in [32, 33], we can obtain the conditional variance of u as

$$\mathrm{Var}\left[u|\xi,\zeta\right] = \frac{N_s N_o}{2}\left(2N_s^2\mathcal{E}_1^{(1)} + \sum_{i=0}^{1}\sum_{j=0}^{N_s-1}\sum_{m=2}^{M}\mathcal{E}_m^{(v_{m,i,j})}\right) + \frac{N_s^2 N_o^2 W T_c}{2}. \tag{3.29}$$

We define the signal-to-interference-and-noise ratio as

$$\mathrm{SINR}_{\xi,\,\zeta} = \frac{z_d^2}{\mathrm{Var}\left[z_I|\xi,\zeta\right] + \mathrm{Var}\left[u|\xi,\zeta\right]}. \tag{3.30}$$

Therefore, given ξ and ζ, the probability of a symbol error for the first user is determined by

$$\Pr\left(e^{(1)}|\xi,\zeta\right) = \Upsilon\left(\sqrt{\mathrm{SINR}_{\xi,\,\zeta}}\right) \tag{3.31}$$

where $\Upsilon(x) := (1/\sqrt{2\pi})\int_x^\infty \exp(-y^2/2)dy$. By taking the expectation of (3.31) with respect to ξ and ζ, we obtain the system bit error rate as

$$\Pr(e) = \mathrm{E}_{\xi,\,\zeta}\left[\Upsilon\left(\sqrt{\mathrm{SINR}_{\xi,\,\zeta}}\right)\right]. \tag{3.32}$$

From the analysis above, we note that the overall multiuser system, including the pulse transmitter, the physical channel and the delay-sum AcR, may be treated as a binary-input additive white Gaussian noise (BIAWGN) channel as in [36]. For such channels, the mutual information between $b_i^{(1)}$ and the estimated value of it $\widehat{b}_i^{(1)}$ is given by

$$I(\widehat{b}_i^{(1)}, \xi, \zeta; b_i^{(1)}) = \mathrm{E}_{\xi,\,\zeta}\left[\mathrm{E}_{b_i^{(1)}\widehat{b}_i^{(1)}}\left[\log_2 \frac{P\left(\widehat{b}_i^{(1)}\middle|\,\xi,\zeta,b_i^{(1)}\right)}{P\left(\widehat{b}_i^{(1)}\middle|\,\xi,\zeta\right)}\right]\right]. \tag{3.33}$$

The outer expectation is taken over ξ and ζ. The inner expectation, conditioned on each channel realization, is the mutual information for the BIAWGN channel, which is maximized when the input is symmetrically distributed. Using (3.33), the system average capacity is defined as

$$\begin{aligned} C &= \max_{p\left(b_i^{(1)}\right)} I\left(\widehat{b}_i^{(1)}, \xi, \zeta; b_i^{(1)}\right) \\ &= \mathrm{E}_{\xi,\,\zeta}\left[\frac{1}{2}\sum_{b_i^{(1)}\in\{-1,1\}}\int_{-\infty}^{\infty} p\left(z\left|\xi,\zeta,b_i^{(1)}\right.\right)\log_2\frac{p\left(z\left|\xi,\zeta,b_i^{(1)}\right.\right)}{p\left(z|\xi,\zeta\right)}dz\right] \end{aligned} \tag{3.34}$$

where

$$p\left(z\left|\xi,\zeta,b_i^{(1)}\right.\right) = \frac{1}{\sqrt{2\pi\Psi}}\exp\left[-\left(z - b_i^{(1)}|z_d|\right)^2/(2\Psi)\right] \tag{3.35}$$

denotes the probability density function of the demodulator output conditioned on the transmitted bit $b_i^{(1)}$, in which

$$\Psi = \sqrt{\mathrm{Var}\left[z_I|\xi,\zeta\right] + \mathrm{Var}\left[u|\xi,\zeta\right]}. \tag{3.36}$$

Correspondingly,

$$p\left(z|\xi,\zeta\right)=\frac{1}{2}\sum_{b_i^{(1)}\in\{-1,1\}}p\left(z\left|\xi,\zeta,b_i^{(1)}\right.\right). \tag{3.37}$$

It should be noted that the above system BER and average capacity analysis, which is based on averaging across the ensemble of channel realizations, applies to the case of time-invariant channels. When the channel is slow-varying and has a coherence-time greater than two symbol durations, (3.32) and (3.34) assume the meaning of symbol-wise instantaneous BER and average capacity, respectively. In this case the system BER and average capacity can be obtained by further averaging (3.32) and (3.34) over the temporal variation of the channel statistics. Another point to note is that, within the framework of our proposed TDMA-based d^{2}TD-IR system, the transmissions from all users are assumed perfectly time-synchronized. For an asynchronous multiuser scenario, we may introduce a random variable in (3.1) to model the temporal misalignment among users' transmissions [85]. This, however, will lead to a highly complex interference model and the expression for B_i in (3.14), which is salient to the analysis that follows, is no longer applicable.

3.3 Estimation of the Optimal T_c

Given a specific type of UWB channel, it is important to choose a chip duration, T_c, that maximizes the system performance in some sense. In practical situation, the UWB channel impulse response, which may contain hundreds of multipath, is difficult to obtain. The mobility of the users worsens the situation. On many occasions, we may only know the average power decay profile, $G(t)$, of

the channel where

$$G(t) = \mathrm{E}\left[\left(g^{(k)}(t)\right)^2\right]. \tag{3.38}$$

Here, we consider using an exponential function to describe $G(t)$,

$$G(t) = ae^{-bt} + c\delta(t) \tag{3.39}$$

where the term $c\delta(t)$ is included because perfect synchronization is assumed and $\tau_1^{(\cdot)} = 0$.

With $G(t)$ known, we proceed to estimate T_c that maximizes $\mathrm{E}_{\xi,\,\zeta}\left[\sqrt{\mathrm{SINR}_{\xi,\,\zeta}}\right]$. From (3.30), we have

$$\mathrm{E}_{\xi,\,\zeta}\left[\sqrt{\mathrm{SINR}_{\xi,\,\zeta}}\right] = \mathrm{E}_{\xi,\,\zeta}\left[\frac{|z_d|}{\sqrt{\mathrm{Var}\left[z_I|\xi,\zeta\right] + \mathrm{Var}\left[u|\xi,\zeta\right]}}\right]. \tag{3.40}$$

For mathematical tractability, we appeal to the following properties of $\mathrm{Var}\left[z_I|\xi,\zeta\right]$ and $\mathrm{Var}\left[u|\xi,\zeta\right]$:

- When $MN_s \gg 1$, the variance of $\mathrm{Var}\left[z_I|\xi,\zeta\right]$ is much smaller than the square of its mean;
- At high E_b/N_o, $\mathrm{Var}\left[u|\xi,\zeta\right] \ll \mathrm{Var}\left[z_I|\xi,\zeta\right]$ for all values of ξ and ζ;
- At low E_b/N_o, in (3.29) $\dfrac{N_sN_o}{2}\left(2N_s^2\mathcal{E}_1^{(1)} + \displaystyle\sum_{i=0}^{1}\sum_{j=0}^{N_s-1}\sum_{m=2}^{M}\mathcal{E}_m^{(v_{m,i,j})}\right)$ is much smaller than the constant $\dfrac{N_s^2N_o^2WT_c}{2}$, causing the variance of $\mathrm{Var}\left[u|\xi,\zeta\right]$ to be close to zero.

With these, we may approximate $\mathrm{Var}\left[z_I|\xi,\zeta\right]$ and $\mathrm{Var}\left[u|\xi,\zeta\right]$ in (3.40) with their

expectations over ξ and ζ. The problem then reduces to finding a T_c that maximizes

$$\sqrt{\mathrm{SINR}_{\overline{h}(t)}} = \frac{\mathrm{E}_{\xi,\,\zeta}[|z_d|]}{\sqrt{\mathrm{Var}\,[z_I] + \mathrm{Var}\,[u]}} \tag{3.41}$$

where

$$\mathrm{Var}\,[z_I] = \mathrm{E}_{\xi,\,\zeta}\left\{\mathrm{Var}\,[z_I|\xi,\zeta]\right\}, \tag{3.42}$$

and

$$\mathrm{Var}\,[u] = \mathrm{E}_{\xi,\,\zeta}\left\{\mathrm{Var}\,[u|\xi,\zeta]\right\}. \tag{3.43}$$

From (3.23), we have

$$\mathrm{E}_{\xi,\,\zeta}\left[|z_d|\right] = N_s^2 \mathrm{E}\left[\mathcal{E}_1\right]. \tag{3.44}$$

By assuming that the signals transmitted by different users undergo independent and identical fading, we have omitted the superscripts denoting the users in (3.44), and shall continue with this omission for the rest of this section.

From (3.28), we obtain $\mathrm{Var}\,[z_I]$ in (3.42) as

$$\mathrm{Var}\,[z_I] = N_s^3 \sum_{m=2}^{M} \mathrm{E}\left[\sigma_{1m}^2\right] + \sum_{j_1=0}^{N_s-1}\sum_{j_2=0}^{N_s-1}\sum_{m_1=2}^{M}\sum_{m_2=2}^{M} \mathrm{E}\left[\left(h_{m_1}^{(v_{m_1,0,j_1})}(t) \circ h_{m_2}^{(v_{m_2,1,j_2})}(t)\right)^2\right] \tag{3.45}$$

where

$$\sigma_{1m}^2 = \left(h_1(t) \circ h_m(t)\right)^2. \tag{3.46}$$

In (3.46), $h_m(t)$, $(m = 1, 2, ..., M)$ comes from different realizations of the channel model. The second term of the right-hand side of (3.45) has $N_s^2(M-1)^2$ sum terms. Because the terms associated with $v_{m_1,0,j_1} = v_{m_2,1,j_2}$ and $m_1 = m_2$ are much larger than those associated with $v_{m_1,0,j_1} \neq v_{m_2,1,j_2}$ or $m_1 \neq m_2$, we may neglect the latter

in the computation for simplicity. Since the probability of $v_{m,0,j_1} = v_{m,1,j_2}$ is

$$P(v_{m,0,j_1} = v_{m,1,j_2}) = \frac{1}{N_u - 1}, \tag{3.47}$$

we have

$$\sum_{j_1=0}^{N_s-1} \sum_{j_2=0}^{N_s-1} \sum_{m_1=2}^{M} \sum_{m_2=2}^{M} \mathrm{E}\left[\left(h_{m_1}^{(v_{m_1,0,j_1})}(t) \circ h_{m_2}^{(v_{m_2,1,j_2})}(t)\right)^2\right] \approx \frac{N_s^2}{N_u - 1} \sum_{m=2}^{M} \mathrm{E}\left[\mathcal{E}_m^2\right]. \tag{3.48}$$

From (3.29), we obtain $\mathrm{Var}[u]$ in (3.43) as

$$\mathrm{Var}[u] = N_s^2 N_o \left(N_s \mathrm{E}[\mathcal{E}_1] + \sum_{m=2}^{M} \mathrm{E}[\mathcal{E}_m]\right) + \frac{N_s^2 N_o^2 W T_c}{2}. \tag{3.49}$$

In order to compute $\sqrt{\mathrm{SINR}_{\overline{h}(t)}}$, we only need to know $\mathrm{E}[\mathcal{E}_m]$, $\mathrm{E}[\sigma_{1m}^2]$ and $\mathrm{E}[\mathcal{E}_m^2]$. In the Appendix A.1, we have shown that

$$\mathrm{E}[\mathcal{E}_m] = \mathcal{E}_\omega \int_{(m-1)T_c}^{mT_c} G(t)dt, \tag{3.50}$$

$$\mathrm{E}\left[\sigma_{1m}^2\right] = \mathcal{E}_\varphi \int_{0}^{T_c} G(t)G(t + (m-1)T_c)dt, \tag{3.51}$$

$$\mathrm{E}\left[\mathcal{E}_m^2\right] \simeq \mathcal{E}_\omega^2 \left(\int_{(m-1)T_c}^{mT_c} G(t)dt\right)^2 \tag{3.52}$$

where $\mathcal{E}_\omega = \int_0^{T_p} \omega^2(t)dt$ and $\mathcal{E}_\varphi = \int_{-T_p}^{T_p} \left(\int_0^{T_p} \omega(\tau)\omega(t+\tau)d\tau\right)^2 dt$. The T_c that maximizes $\sqrt{\mathrm{SINR}_{\overline{h}(t)}}$ is obtained by solving the equation below

$$\frac{\partial \sqrt{\mathrm{SINR}_{\overline{h}(t)}}}{\partial T_c} = 0. \tag{3.53}$$

In Appendix A.2, we derive an expression, (A.19), which can be used to numerically evaluate the optimal T_c in the sense of (3.53).

3.4 Simulations and Numerical Results

In this section, we present computer simulated and numerically evaluated results to validate our analysis and designs. In all cases, the random channels are generated according to [44]. The channel model used in each simulation, if not specified, is the CM 1, $0 \sim 4$ meters' range with line-of-sight (LOS) model. The sampling interval is 0.167 ns. The bandwidth of the lowpass filter is 2.994 GHz. As in [8], we select the shape of the monocycle $\omega(t)$ to be the second derivative of a Gaussian pulse, namely, $[1 - 4\pi(t/\tau_m)^2] \exp[-2\pi(t/\tau_m)^2]$, where $\tau_m = 0.2877$ ns.

3.4.1 BER Performance (Simulations)

Here, we present simulation results for the BER performance as a function of the ratio E_b/N_o, the chip duration, T_c, and the spreading factor, N_s, for systems that support N_u users. In the legends of all our BER plots, "Simu" represents the BER performance obtained by computer simulation of the overall transmission chain while "Theo" denotes numerical results obtained using (3.32).

Case 1 (BER performance versus E_b/N_o for various T_c and N_s values with N_u and T fixed)

Fig. 3.3 shows the BER performances of the d^{2}TD-IR system with $N_u = 10$ and $T = 668.00$ ns fixed. Different chip durations, T_c, and spreading factors, N_s, where $N_s T_c = T/N_u = 66.80$ ns, are employed in the simulations. The results show

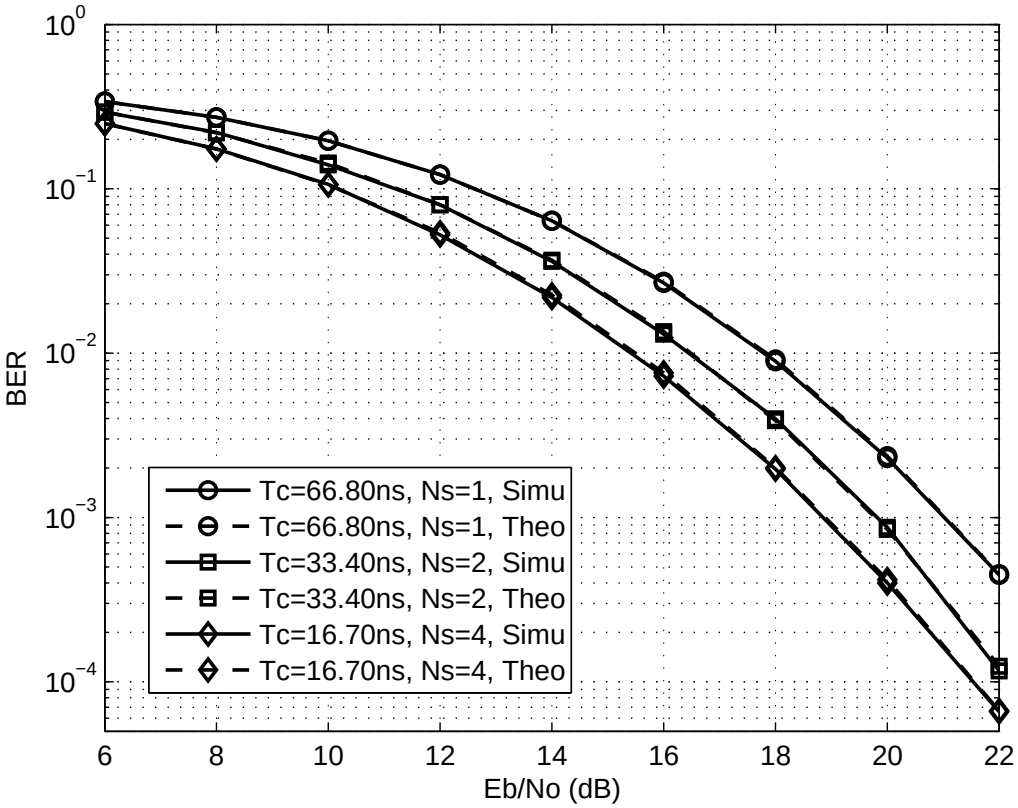

Fig. 3.3: BER versus E_b/N_o for various T_c and N_s values with T fixed; ten-user d^2TD-IR system.

that with the same symbol duration, T, multi-pulse per symbol signaling ($N_s > 1$) performs better than single-pulse signaling ($N_s = 1$) when $E_b/N_o < 22$ dB. Fig. 3.3 also shows that the simulation results match theoretical predictions within the range of E_b/N_o values under consideration.

Case 2 (BER performance versus E_b/N_o for various T_c values with N_u and N_s fixed)

Fig. 3.4 compares the BER performances of the d^{2}TD-IR system for various values of the chip duration, T_c, with $N_u = 10$ and $N_s = 2$ fixed. It is observed

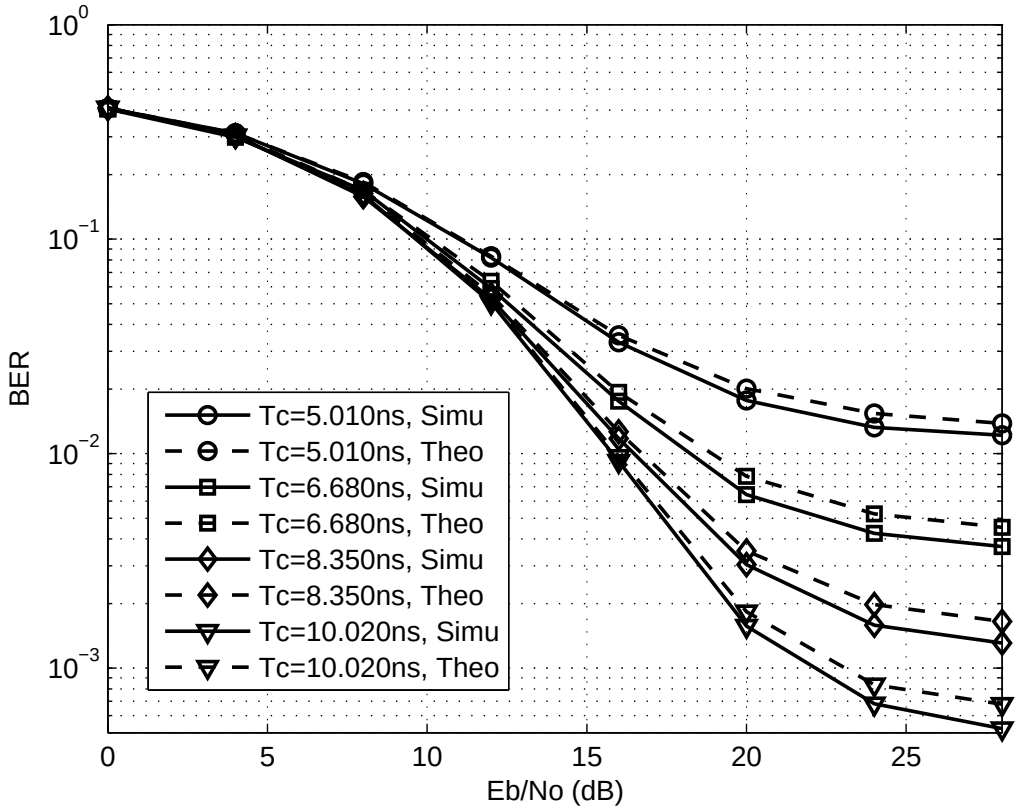

Fig. 3.4: BER versus E_b/N_o for various T_c values with $N_s = 2$; ten-user d^2TD-IR system.

that at low E_b/N_o where the effect of channel noise is dominant, the simulation results can be theoretically predicted to very good accuracy. Whereas at high E_b/N_o, the theoretical BERs are always higher than the simulated ones. This can be explained by the fact that the theoretical BER is derived with a Gaussian assumption on statistics of the interference component, z_I, in (3.20), which requires N_s to be sufficiently large. The observed discrepancy is thus caused by the small N_s used, which shows up when the effect of MUI becomes dominant at high E_b/N_o.

Case 3 (BER performance of d^{2}TD-IR system versus TH-IR system)

Here, we compare the BER performance of the d^{2}TD-IR system with that of the TH-IR system [8]. The results are shown in Fig. 3.5 for systems with $N_u = 10$. For both systems, the symbol duration used is $T = 334.00$ ns, which is equivalent to a system transmission rate of about 30 Mb/s. In TH-IR system, each symbol is conveyed by 10 pulses and the chip duration is 0.835 ns. In our proposed system, spreading factors of $N_s = 1$ and $N_s = 2$, which result in chip durations of 33.400 ns and 16.700 ns, respectively, are used. In Fig. 3.5, the label "Rake-N TH-IR" is used to denote the conventional TH-IR system with an N-finger Rake receiver, which employs maximum ratio combining. The label "d2TD-IR" is used to denote our proposed systems. A general observation is that the BER of d^{2}TD-IR systems improves at a faster rate than that of TH-IR systems as E_b/N_o increases, and both d^{2}TD-IR systems outperform all the TH-IR systems under consideration when the E_b/N_o is greater than 22 dB.

3.4.2 Average Capacity (Numerical Evaluations)

Here, we provide several examples to show how the parameters T_c and N_s affect the average capacity of the system given by (3.34).

Case 1 (Effects of spreading factor N_s)

Here we examine how the variation of N_s would affect the average capacity of the d^{2}TD-IR system with $N_u = 10$ and $T = 300.60$ ns. The average capacities with respect to E_b/N_o for different N_s values are plotted in Fig. 3.6. Here, we note that as the value of N_s changes, the value of T_c will change according to $T_c = T/(N_u N_s)$.

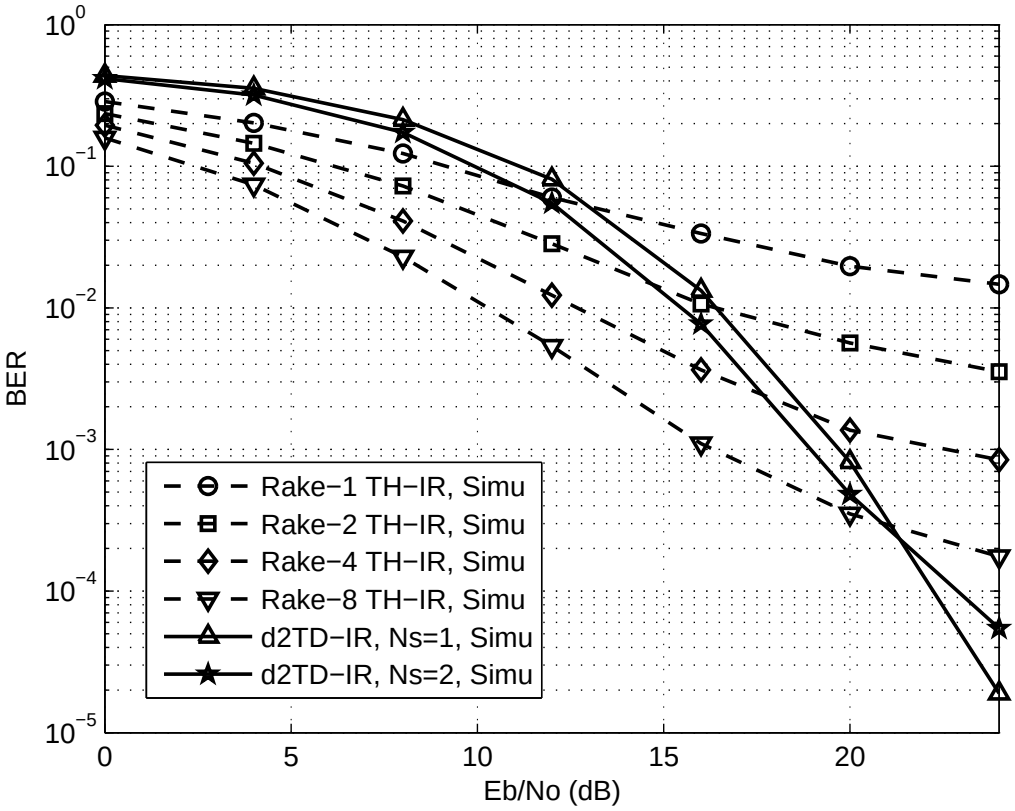

Fig. 3.5: BER versus E_b/N_o; ten-user d^2TD-IR system versus TH-IR system, $T = 334.00$ ns.

From Fig. 3.6, we observe that the value of the spreading factor, N_s, that achieves the highest average capacity at a given E_b/N_o value, decreases as E_b/N_o increases. When $E_b/N_o \to \infty$, the system with $N_s = 1$ will always yield the highest average capacity value. This is because when $E_b/N_o \to \infty$, the effect of channel noise is negligible. The system with a smaller N_s (or larger T_c, because $N_s T_c$ is constant) will result in the least channel induced MUI.

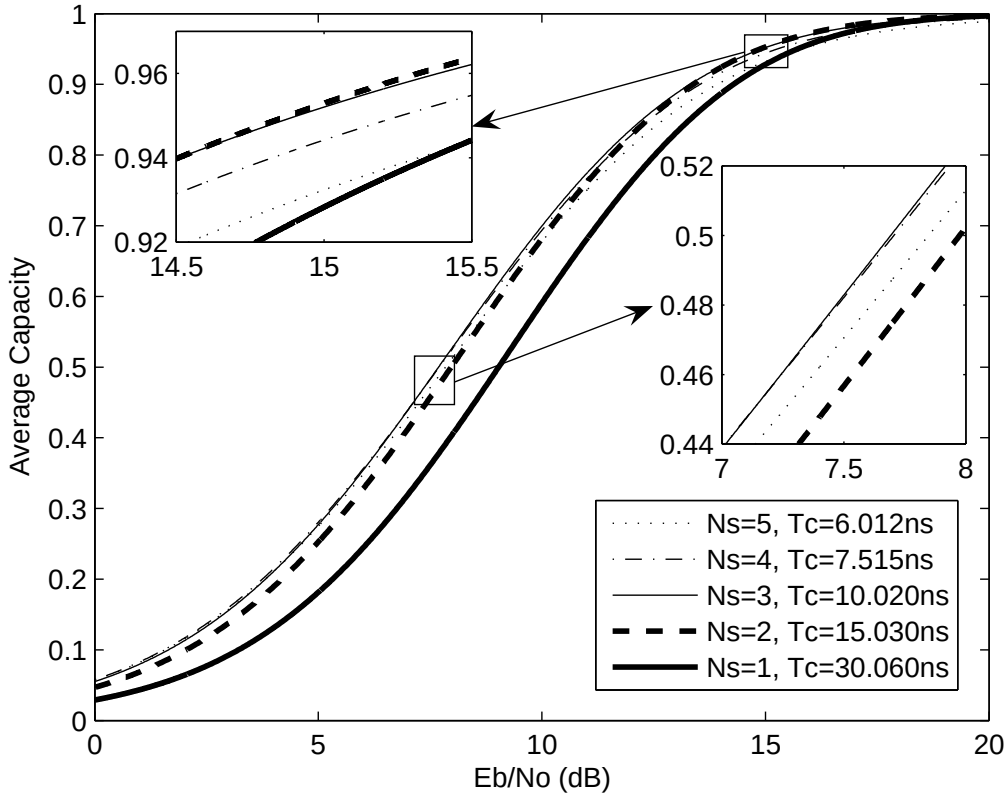

Fig. 3.6: Average capacity comparison with respect to different T_c and N_s values with T fixed; ten-user d^2TD-IR system.

Case 2 (Effects of chip duration T_c)

In Fig. 3.7, we show the effects of chip duration on the average capacity of the system. Here, we set $N_s = 2$, $N_u = 10$, and the symbol duration, T, is allowed to float according to the value of T_c. From Fig. 3.7, we observe that for $T_c \leq 5$ ns, the average capacity increases rapidly with increasing T_c. This is due to the fact that when T_c is relatively short, the power of the desired signal increases rapidly and the power of MUI decreases with increasing T_c, which can be seen from (3.23) and (3.28). This is also the reason that the BER performances improve with increasing

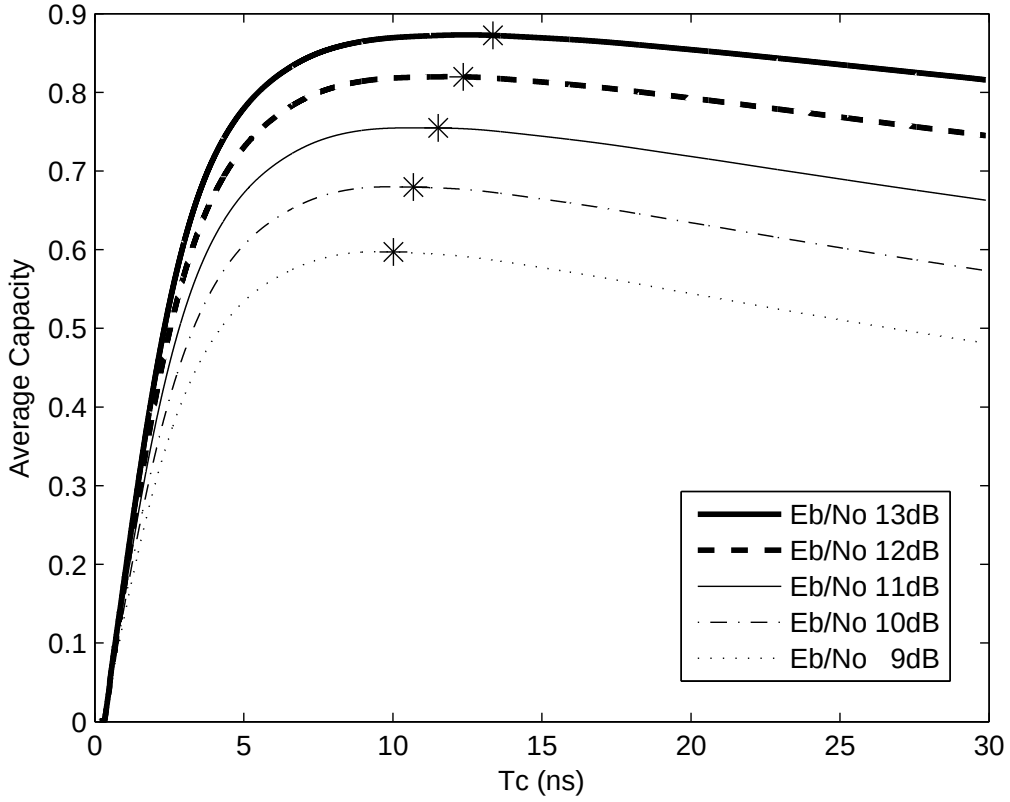

Fig. 3.7: Average capacity versus the chip duration T_c, $N_s = 2$; ten-user d^2TD-IR system.

T_c in Fig. 3.4. Also from Fig. 3.7, when T_c increases beyond about 15 ns, the average capacity decreases slowly. This is because the average power of UWB channel impulse response decay almost exponentially with the delay. When T_c is relatively long, the captured multipath power increases at a slower rate compared to the captured channel noise power, which can be seen from (3.23) and (3.29).

We also use the method presented in Section 3.3 to compute the optimal T_c which maximizes $\sqrt{\text{SINR}_{\overline{h}(t)}}$. The function $G(t)$ in (3.39) used for our computation

is described as follows:

$$G(t) = 0.0371e^{-0.1916t} + 0.0130\delta(t). \tag{3.54}$$

The optimal T_c's which maximize $\sqrt{\text{SINR}_{\overline{h}(t)}}$ are shown as the points marked by "*" in Fig. 3.7. As can be seen in the graph, these T_c's which maximize $\sqrt{\text{SINR}_{\overline{h}(t)}}$ give a very good indication of the actual T_c's that achieve the maximum average capacity values on the curves.

Case 3 (optimal T_c)

Fig. 3.8 compares the T_c which maximizes $\text{E}_{\xi,\,\zeta}\left[\sqrt{\text{SINR}_{\xi,\,\zeta}}\right]$ (labeled "Numerical optimal T_c" in the legend) and that which maximizes $\sqrt{\text{SINR}_{\overline{h}(t)}}$ (labeled "Estimated optimal T_c" in the legend) when $N_s = 1$, and $N_s = 4$ for a d^{2}TD-IR system with $N_u = 10$. From Fig. 3.8, we observe that the T_c which maximizes $\sqrt{\text{SINR}_{\overline{h}(t)}}$ can provide a fairly good estimate of the T_c which maximizes $\text{E}_{\xi,\,\zeta}\left[\sqrt{\text{SINR}_{\xi,\,\zeta}}\right]$. For both $N_s = 1$ and $N_s = 4$, the estimation error falls below 10% for 5 dB$< E_b/N_o <$ 30 dB.

For UWB channel model CM 3 ($4 \sim 10$ meters' range with NLOS model), we provide the comparison of the T_c which maximizes $\text{E}_{\xi,\,\zeta}\left[\sqrt{\text{SINR}_{\xi,\,\zeta}}\right]$ and that which maximizes $\sqrt{\text{SINR}_{\overline{h}(t)}}$ in Fig. 3.9. The function $G(t)$ in (3.39) used for our computation is described as follows:

$$G(t) = 0.0141e^{-0.0701t} + 0.0060\delta(t). \tag{3.55}$$

When $N_s = 1$, and $N_s = 4$, from Fig. 3.9, the estimation error also falls below 10% for 5 dB$< E_b/N_o <$ 30 dB.

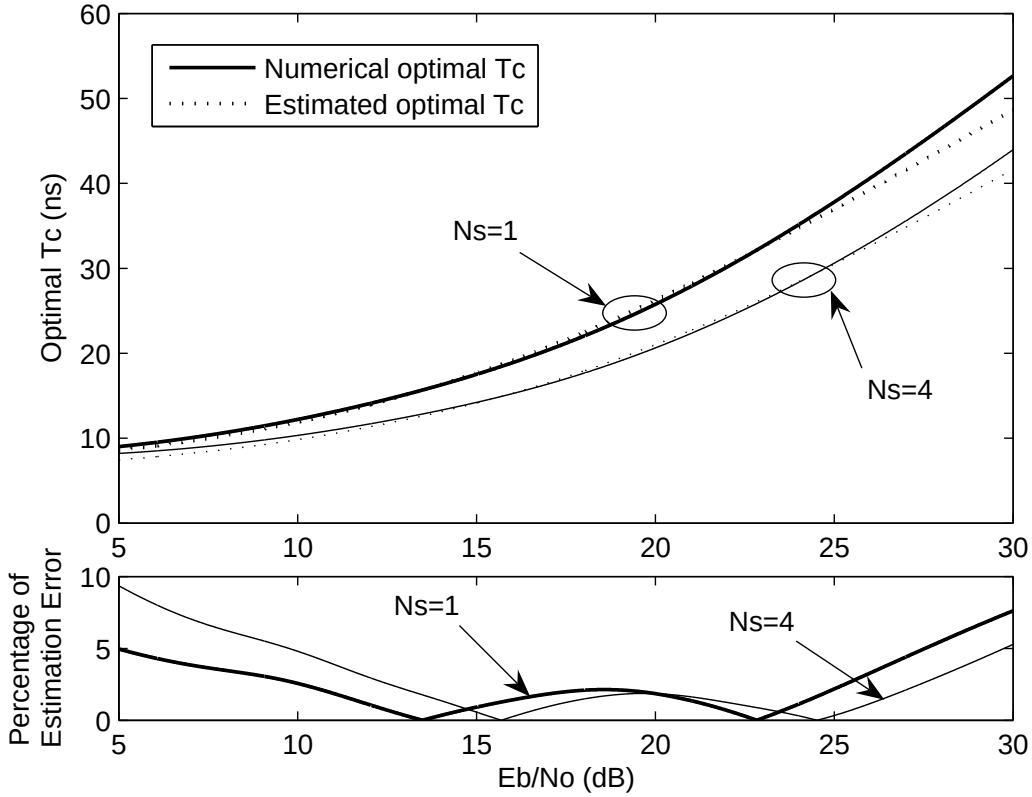

Fig. 3.8: Comparison of the T_c which maximizes $E_{\xi,\,\zeta}\left[\sqrt{SINR_{\xi,\,\zeta}}\right]$ (labeled "Numerical optimal T_c" in the legend) and the T_c which maximizes $\sqrt{SINR_{\overline{h}(t)}}$ (labeled "Estimated optimal T_c" in the legend) when $N_s = 1$ and $N_s = 4$; ten-user d^2TD-IR system in CM 1 UWB channels.

3.4.3 Robustness Issues (Simulations)

Our preceding results are obtained for the quasi-static UWB channel with the assumption of perfect channel synchronization. Here, we examine the performance of the proposed d^2TD-IR system under more practical environments, where the channel is time-varying and where perfect channel synchronization is not achievable.

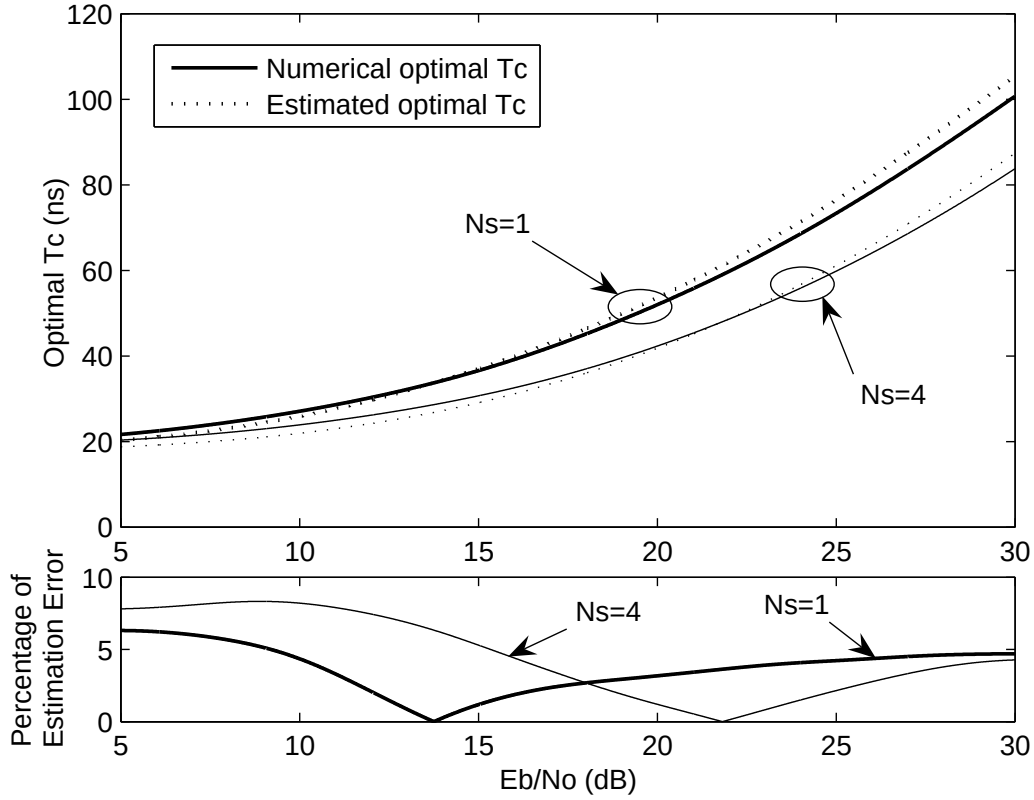

Fig. 3.9: Comparison of the T_c which maximizes $E_{\xi,\,\zeta}\left[\sqrt{SINR_{\xi,\,\zeta}}\right]$ and the T_c which maximizes $\sqrt{SINR_{\overline{h}(t)}}$ when $N_s = 1$ and $N_s = 4$; ten-user d^2TD-IR system in CM 3 UWB channels.

Case 1 (In the presence of channel variation)

We consider a time-varying UWB channel whose impulse response at the offset time of mT_c is denoted as $g^{(k)}(t, mT_c)$. The channel impulse responses $g^{(k)}(t, m_1T_c)$ and $g^{(k)}(t, m_2T_c)$ are independent if $m_1T_c - m_2T_c \geq T_s$, where T_s is the coherence time. In this thesis, the channel evolution per chip duration is generated using a simple linear interpolation model

$$g^{(k)}(t, mT_c) = \frac{T_s - (mT_c \bmod T_s)}{T_s} g^{(k)}_{\lfloor mT_c/T_s \rfloor}(t) + \frac{(mT_c \bmod T_s)}{T_s} g^{(k)}_{\lceil mT_c/T_s \rceil}(t) \quad (3.56)$$

where $\lfloor \bullet \rfloor$ and $\lceil \bullet \rceil$ denote integer floor and ceil, respectively. In (3.56), $g_i^{(k)}(t)$, $i = 1, 2, 3, \cdots$ are randomly generated independent channels. The BER performances of the system are examined with $T_s = 10^{-3}$ s. Fig. 3.10 shows the BER performances of the d^{2}TD-IR system with $N_u = 10$ and $N_s = 2$ fixed in the time-varying and time-invariant UWB channels. In the graph, "TV" stands for the time-varying channel. We observe that the BER performances of the system in the time-varying channel seem almost unchanged compared with that in the static channels. This is due to the AcR, which is inherently robust to the slow channel variation.

Case 2 (Without perfect channel synchronization)

Channel synchronization errors will induce BER performance degradation. To examine the sensitivity of the d^{2}TD-IR system with respect to timing synchronization error, we do the computer simulations by letting

$$\widetilde{g}^{(k)}(t) = g^{(k)}(t - \tau^{(k)}) \tag{3.57}$$

where $g^{(k)}(t)$ and $\widetilde{g}^{(k)}(t)$ are the channel impulse responses with and without perfect channel synchronization, respectively. The timing error $\tau^{(k)}$ is modeled as a Gaussian random variable with zero mean and variance 9 ns^2. In Fig. 3.11, we compare the TH-IR system and the proposed system with and without perfect channel synchronization. In the graph, "WS" stands for the system without perfect channel synchronization. The parameters of the Rake-8 TH-IR system is the same as those in Fig. 3.5. From Fig. 3.11, we observe that the Rake-8 TH-IR system would suffer severe system BER degradation. However, the proposed ten-user system in which $N_s = 2$ and $T_c = 16.700$ ns can still achieve the BER of 8×10^{-3} when E_b/N_o is

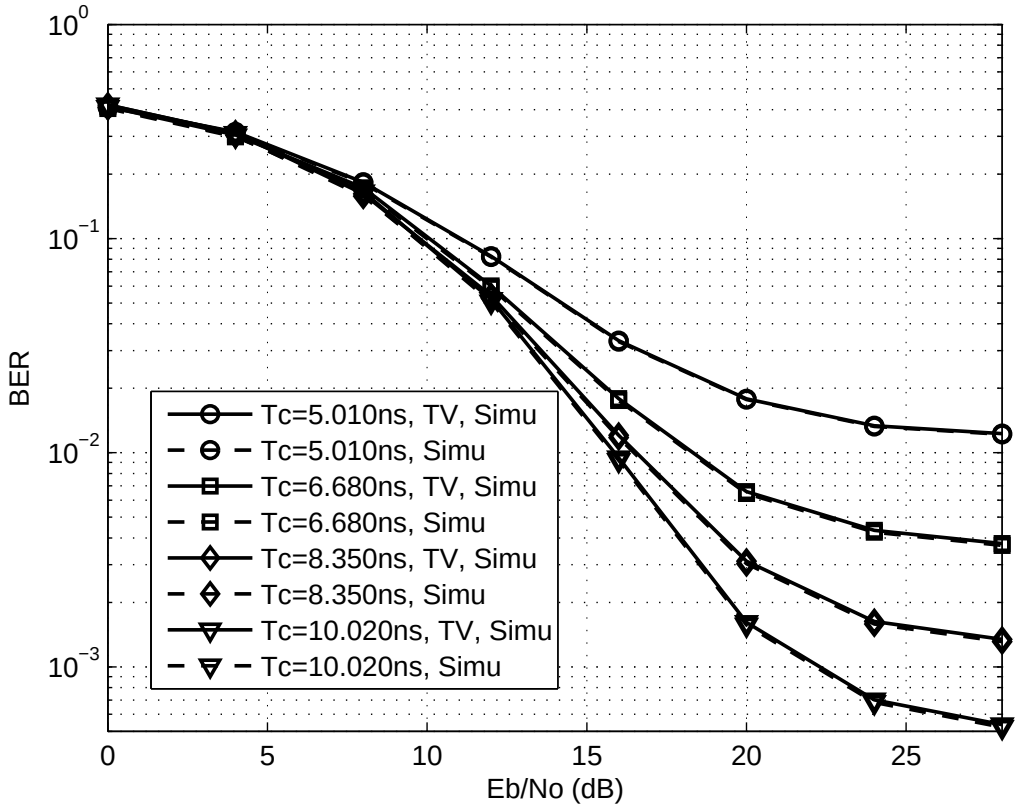

Fig. 3.10: BER versus E_b/N_o; ten-user d^2TD-IR system in which $N_s = 2$ in the time-varying UWB channel.

20 dB. In Fig. 3.11, we also present the simulation results for the proposed system with the same spreading factor and the shorter chip durations $T_c = 10.020$ ns. It is found that with the decrease of T_c, the discrepancy between the BER performances with and without perfect channel synchronization decreases. This is expected since systems with a larger T_c has lesser channel induced MUI and a slight increase in MUI due to synchronization error would have a greater impact on the BER.

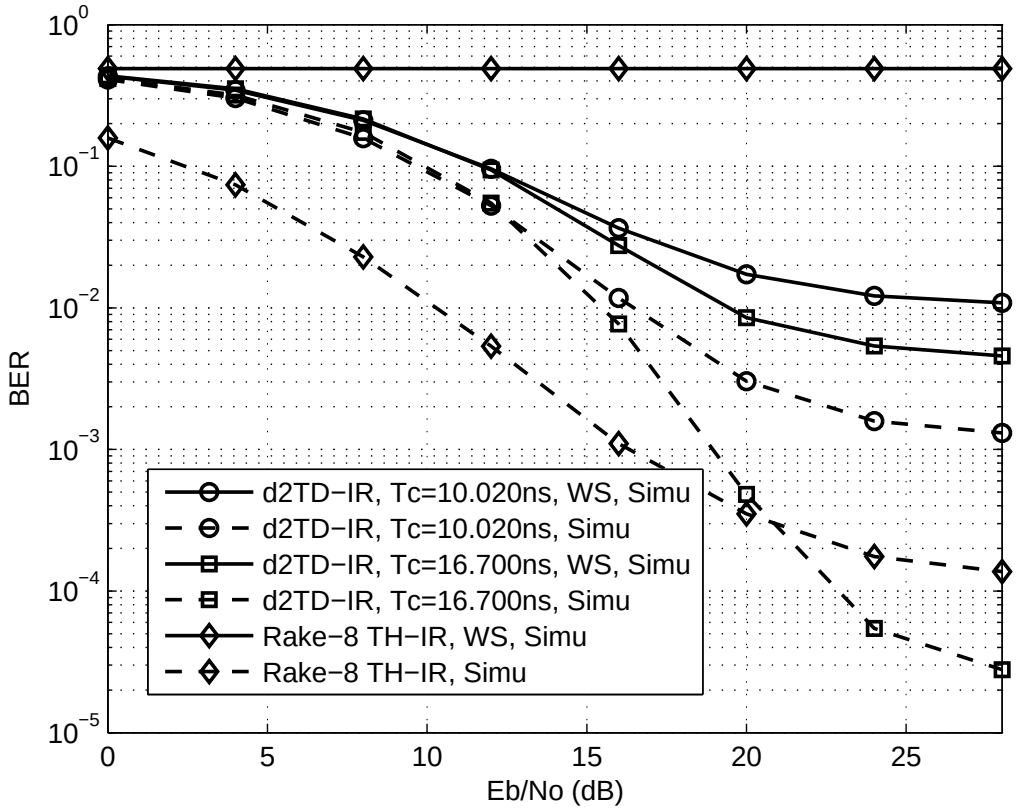

Fig. 3.11: BER versus E_b/N_o; ten-user d^2TD-IR system in which $N_s = 2$ versus TH-IR system, with and without perfect channel synchronization.

3.5 Summary

In this chapter, we proposed a d^2TD-IR system. The system BER performance and average capacity were derived theoretically. With the knowledge of UWB channel power decay profile, we discussed the method to estimate the optimal chip duration which maximizes the signal-to-interference-and-noise ratio. From the simulation and numerical results provided in Section 3.4, it was observed that the proposed system gives better performance than the conventional TH-IR system at high E_b/N_o. This is because the proposed d^2TD-IR employs a hybrid of time-

division (TD) and time-hopping (TH) multiple access scheme and a delay-sum AcR, which efficiently suppress the multiuser interference (MUI). At high E_b/N_o, MUI has significant effect on the system performance.

The proposed d^{2}TD-IR system assumes perfect synchronization among user. The problem of how to achieve perfect synchronization, which has been left open, will be discussed in the next chapter.

Chapter 4

Synchronization and Power Control for d^{2}TD-IR Systems

In Chapter 3, the d^{2}TD-IR system is studied with the assumption of perfect time synchronization among users. The assumption is valid only when we can design an effective synchronization algorithm. We also mentioned that the ill-effects of MUI and prolonged deep fade on the BER performance can be reduced through power control. In this chapter, both synchronization and power control problems for the d^{2}TD-IR system are discussed for the case of infrastructure networks. In the network, different users are synchronized and use the uplink channels to transmit data to the base station (BS). The BS uses downlink channels to broadcast information and control signals to the users.

In Section 4.1, we first describe a non-recursive time of arrival (TOA) based synchronization algorithm. Then, we discuss how to couple power control into the synchronization algorithm and develop a recursive algorithm combining syn-

chronization and power control. In Section 4.3, computer simulated results are presented to test the efficiency of our proposed algorithms.

4.1 Synchronization for d^{2}TD-IR Systems

During the synchronization process, a user starts to transmit pilot symbols on receiving a cue signal from the downlink control/broadcast channel. The transmitted signal model for user k is the same as in (3.1), where the pilot symbols $d_i^{(k)} \in \{-1, 1\}$ and $b_i^{(k)} = d_i^{(k)} d_{i-1}^{(k)} \in \{-1, 1\}$ are known to the BS receiver. Because the BS has no information of the time of arrival (TOA) of the signals from different users, denoted as $\{T_A^{(k)}; k = 1, 2, \cdots, N_u\}$, the received signal due to user k is written as

$$r^{(k)}(t) = \sum_i \sum_{j=0}^{N_s-1} d_i^{(k)} a_{i \bmod 2,j}^{(k)} h^{(k)} \left(t - iT - jT_f - c_{i \bmod 2,j}^{(k)} T_c - T_A^{(k)} \right) \tag{4.1}$$

where $h^{(k)}(t)$ is defined in (3.4). From the composite received signal, $r(t)$, which is defined in (3.5) carrying only the pilot symbols, the BS estimates the TOAs of different users. With the knowledge of TOAs, the BS reschedules the transmit time for different users. The users adjust the transmitter timing based on the feedback from BS. Once synchronization process is complete, the user transmits data in the preassigned chips.

In the following, we will provide a detailed description of a TOA based synchronization approach for the proposed d^{2}TD-IR system, which is an extension of the approach in [51]. As in [51], our synchronization approach is implemented in multiple steps:

Step 1. This step performs a frame-level search. In an indoor environment, the distance between the transmitter and the receiver is considered to be less than 20 meters. Accordingly, the TOA is less than $20/(3 \times 10^8) = 66.67 \times 10^{-9}$ s = 66.67 ns, which is usually less than a frame duration. Therefore, without loss of generality, we assume that $T_A^{(\cdot)}$ is uniformly distributed over $(0, T_f]$, which denotes the initial uncertainty region U_0.

We integrate the output of the i^{th} symbol to obtain the decision statistics by using

$$D_{i,\varsigma_q}^{(k)} = \int_{(i+1)T-T_c+\varsigma_q}^{(i+1)T+\varsigma_q} x_{i \bmod 2}^{(k)}(t) x_{(i-1) \bmod 2}^{(k)}(t-T)dt \tag{4.2}$$

where $x_{i \bmod 2}^{(k)}(t)$ is defined in (3.9) and ς_q is the integration starting point in Step q. For Step 1, $\varsigma_1 = 0, T_c, 2T_c, \cdots, T_f$. The coarse TOA estimation, $\widehat{T}_{A,1}^{(k)}$, for the k^{th} user, is obtained by [51]

$$\widehat{T}_{A,1}^{(k)} = \arg\max_{\varsigma_1} \left\{ \sum_{v=\varsigma_1} D_{i,v}^{(k)} b_i^{(k)} \right\}. \tag{4.3}$$

In (4.3), the decision statistics, $D_{i,\varsigma_1}^{(k)}$, is multiplied with the pilot symbol, $b_i^{(k)}$, to get the estimation of desired signal power when the integration starting point is ς_1. For each value of ς_1, the product $D_{i,\varsigma_1}^{(k)} b_i^{(k)}$ is computed for P consecutive symbol intervals and then averaged to produce an estimate of the TOA. Averaging is required for synchronization accuracy since $D_{i,\varsigma_1}^{(k)}$ contains multiuser interference and channel noise. Because there are $N_u + 1$ different values of ς_1, altogether $P(N_u + 1)$ pilot symbols are needed for Step 1. After the coarse TOA estimation, $\widehat{T}_{A,1}^{(k)}$, is obtained,

the BS arranges the transmitted signal of the k^{th} user to be

$$s_1^{(k)}(t) = s_0^{(k)}(t - \widehat{T}_{A,1}^{(k)}) \tag{4.4}$$

where $s_0^{(k)}(t)$ and $s_1^{(k)}(t)$ denote the transmitted signals before and after coarse synchronization, respectively. Therefore, the uncertainty region after Step 1 is $U_1 = (-T_c, T_c]$.

Step q ($q \geq 2$). Denote the width the uncertainty region U_{q-1} as Δ_{q-1}. The aim of this step is to reduce Δ_{q-1} to Δ_{q-1}/N, where N is an integer constant larger than one. The sampled output of the i^{th} symbol is obtained using (4.2), where the integration starting points are $\varsigma_q = -(N-1)\Delta_{q-1}/(2N), -(N-2)\Delta_{q-1}/(2N), \cdots, (N-1)\Delta_{q-1}/(2N)$. As in Step 1, we collect P products of $D_{i,\varsigma_1}^{(k)} b_i^{(k)}$ for each value of ς_q. Since there are $N+1$ different values of ς_q, altogether $P(N+1)$ pilot symbols are needed for Step q. The TOA estimation, $\widehat{T}_{A,q}^{(k)}$, of Step q for the k^{th} user is obtained by

$$\widehat{T}_{A,q}^{(k)} = \widehat{T}_{A,q-1}^{(k)} + \arg\max_{\varsigma_q} \left\{ \sum_{v=\varsigma_q} D_{i,v}^{(k)} b_i^{(k)} \right\}. \tag{4.5}$$

The BS then arranges the transmitted signal of the k^{th} user to be

$$s_q^{(k)}(t) = s_0^{(k)}(t - \widehat{T}_{A,q}^{(k)}) \tag{4.6}$$

where $s_q^{(k)}(t)$ denotes the transmitted signal after Step q. Therefore, the uncertainty region after Step q is $U_q = (-\Delta_{q-1}/(2N), \Delta_{q-1}/(2N)]$.

The algorithm will stop when the width of uncertainty region is less than or equal to certain value, Δ, which is denoted as synchronization level.

4.2 Power Control for d^{2}TD-IR Systems

In cellular radio and personal communication systems the power levels transmitted by every user are under constant control by the base stations (BSs) [86]. This is done to ensure that each user transmits the smallest power necessary to maintain a good quality link. Power control not only helps prolong battery life for the mobile transmitters, but also dramatically reduces the interference.

To achieve perfect power control in the proposed d^{2}TD-IR system, the signal model for user k in (3.1) should be modified to

$$s^{(k)}(t) = \sum_{i} \sum_{j=0}^{N_s-1} d_i^{(k)} a_{i \bmod 2,j}^{(k)} \sqrt{\Omega^{(k)}} \omega(t - iT - jT_f - c_{i \bmod 2,j}^{(k)} T_c) \tag{4.7}$$

where $\Omega^{(k)}$ is the power level control factor of user k. In this thesis, perfect power control is defined as the case when the BS receives signals of equal power from different users, namely,

$$\Omega^{(k_1)} \int_0^{T_c} \left(h^{(k_1)}(t)\right)^2 dt = \Omega^{(k_2)} \int_0^{T_c} \left(h^{(k_2)}(t)\right)^2 dt \tag{4.8}$$

for $k_1, k_2 \in \{1, 2, \cdots, N_u\}$, where $h^{(k)}(t)$ is defined in (3.4). In Chapter 3, we studied the proposed d^{2}TD-IR system without power control where different users transmit signals with the same power, that is $\Omega^{(k)} = 1$ for $k \in \{1, 2, \cdots, N_u\}$. Under such circumstances, perfect power control is achieved by finding $\Omega^{(k_1)} \neq \Omega^{(k_2)}$, for $k_1, k_2 \in \{1, 2, \cdots, N_u\}$ that satisfy (4.8) since $h^{(k_1)}(t) \neq h^{(k_2)}(t)$.

By assuming perfect power control among users, we do computer simulations to study the performance of d^{2}TD-IR system. It is shown in Fig. 4.3 that with perfect power control, the system performance will dramatically improve. It is thus

desirable to incorporate power control into the proposed d^2TD-IR system. Since our proposed synchronization algorithm is applied in multiple steps, we consider to combine the power control process with the synchronization process, namely, we do power control after each step of synchronization. Intuitively, the above approach should have better performance than doing power control and synchronization separately. However, one practical problem is error propagation, which means users having larger synchronization errors generally have lower received signal power and will be erroneously allocated higher transmission power. To prevent error propagation, we propose a recursive algorithm which combines synchronization and power control in this section. Similar to the synchronization process, the recursive algorithm is implemented in multiple steps:

Step 1. This step is the same as the Step 1 described in Section 4.1. The power control process is omitted in this step, since the synchronization error after this step is relatively large.

Step q ($q \geq 2$). The TOA estimation process in this step is the same as the Step q described in Section 4.1. Each user sends $P(N+1)$ pilots symbols for synchronization. After TOA estimation of Step q, we can also obtain the average power, $\Gamma_q^{(k)}$, of received signals for the k^{th} user

$$\Gamma_q^{(k)} = \frac{1}{P} \max \left\{ \sum_{v=\varsigma_q} D_{i,v}^{(k)} b_i^{(k)} \right\}. \tag{4.9}$$

From (4.2) and (3.18 - 3.22), by assuming the interference and channel noise to be Gaussian as in Chapter 3, we have

$$\mathrm{E}_\eta \left[\Gamma_q^{(k)} \right] = N_s^2 \int_{\widehat{T}_{A,q}^{(k)}}^{T_c + \widehat{T}_{A,q}^{(k)}} \left(h^{(k)}(t) \right)^2 dt \tag{4.10}$$

where η represents the pilot symbols $\{d_i^{(k)}; k = 1, 2, 3, \cdots, N_u\}$. Therefore, $\Gamma_q^{(k)}$ is an estimate of $N_s^2 \int_{\widehat{T}_{A,q}^{(k)}}^{T_c+\widehat{T}_{A,q}^{(k)}} \left(h^{(k)}(t)\right)^2 dt$.

Before the power control process, it is required to check whether the following three conditions are satisfied to prevent error propagation. If any one of the conditions is not satisfied, we repeat Step $q-1$ with the next P incoming pilot symbols using the estimated TOAs, power level control factors, and U_{q-2} obtained in Step $q-2$. These three conditions are:

- the average power of received signals, $\Gamma_q^{(k)}$, for the k^{th} user is larger than zero. This condition is reasonable because the average power should be positive. If not, it is due to either synchronization errors or multiuser interference (MUI) and channel noise. Because it is difficult to know which one is the actual reason, we are required to repeat Step $q-1$;

- the minimum $\Gamma_q^{(k)}$ of all the users in Step q is larger than that in Step $q-1$, namely,

$$\min\left\{\Gamma_q^{(k)}\right\} > \min\left\{\Gamma_{q-1}^{(k)}\right\}. \tag{4.11}$$

  This is because we fix the total transmission power from all users. After combined synchronization and power control process Step $q-1$, we should increase the transmission power of users with weak received signal power and decrease the transmission power of users with strong received signal power. This condition makes sure that the user with the minimum averge power of received signals in Step $q-1$ had been properly allocated more power to transmit signals in Step q;

- the sum of received signal power to transmitted signal power ratios of all the users in Step q is larger than that in Step $q-1$. This condition is equivalent

to the inequality shown below

$$\sum_{k=1}^{N_u} \frac{\Gamma_q^{(k)}}{\Omega_{q-1}^{(k)}} > \sum_{k=1}^{N_u} \frac{\Gamma_{q-1}^{(k)}}{\Omega_{q-2}^{(k)}} \tag{4.12}$$

where $\Omega_q^{(k)}$ is the power level control factor in Step q. Because no power control process before Step 1 and Step 2, $\Omega_0^{(k)}$ and $\Omega_1^{(k)}$ are set to be one for $k \in \{1, 2, \cdots, N_u\}$. This condition is required because with the process of synchronization and power control, the overall transmission efficiency of the system should be improved. Otherwise, there exist large synchronization errors or large power control errors and we should repeat Step $q-1$.

If all the conditions above are satisfied, the BS arranges the transmitted signal of the k^{th} user to be

$$s_{q+1}^{(k)}(t) = \sqrt{\Omega_q^{(k)}}\ s_0^{(k)}(t - \widehat{T}_{A,q}^{(k)}) \tag{4.13}$$

and proceed to do Step $q+1$. To fairly compare the proposed systems with and without power control, we redefine the ratio E_b/N_o as the average transmission power per bit to noise power ratio, which is $\frac{N_s}{N_o N_u} \int_0^{T_\omega} \omega^2(t)dt \sum_{k=1}^{N_u} \Omega_q^{(k)}$. To make sure that average transmission power of all the users with and without power control remains the same, we have

$$\frac{1}{N_u} \sum_{k=1}^{N_u} \Omega_q^{(k)} = 1. \tag{4.14}$$

Therefore, the power level control factor $\Omega_q^{(k)}$ in (4.13) is obtained by

$$\Omega_q^{(k)} = \begin{cases} 1; & q < 2 \\ \left[\dfrac{1}{N_u} \left(\displaystyle\prod_{v=2}^{q} \Gamma_v^{(k)} \right) \displaystyle\sum_{k=1}^{N_u} \dfrac{1}{\displaystyle\prod_{v=2}^{q} \Gamma_v^{(k)}} \right]^{-1} & ; \quad q \geq 2. \end{cases} \tag{4.15}$$

The reason that $\displaystyle\prod_{v=2}^{q} \Gamma_v^{(k)}$ instead of only $\Gamma_q^{(k)}$ is used to compute $\Omega_q^{(k)}$ is because the transmission power of $s_q^{(k)}(t)$ is power controlled by the factor $\Omega_{q-1}^{(k)}$, which is computed based on the information of $\Gamma_2^{(k)}, \Gamma_3^{(k)}, \cdots$, and $\Gamma_{q-1}^{(k)}$.

The algorithm will stop when the width of uncertainty region is less than or equal to certain value, Δ, which is denoted as synchronization level.

4.3 Simulation Results

In this section, we present computer simulation results to validate our designs. In all cases, the random channels are generated according to [44]. The channel model used in each simulation, if not specified, is the CM 1, $0 \sim 4$ meters' range with line-of-sight (LOS) model. The sampling interval is 0.167 ns. The bandwidth of the lowpass filter is 2.994 GHz. As in [8], we select the shape of the monocycle $\omega(t)$ to be the second derivative of a Gaussian pulse, namely, $[1 - 4\pi(t/\tau_m)^2] \exp[-2\pi(t/\tau_m)^2]$, where $\tau_m = 0.2877$ ns.

4.3.1 Synchronization

In Fig. 4.1, we compare the BER performance of the d^{2}TD-IR system after synchronization process with that under perfect synchronization, where the system parameters are $T_c = 10.688$ ns, $N_s = 2$ and $N_u = 10$. In each step of synchronization process, the width of uncertainty regions are reduced by half ($N = 2$). Therefore, to achieve different synchronization levels where $\Delta = 2T_c,\ T_c,\ T_c/2,$ and $T_c/4$, it is required to perform 1, 2, 3, and 4 steps of the synchronization algorithm, respectively. In the simulations, when the synchronization level is $2T_c,\ T_c,$ and $T_c/2$, we use the parameter $P = 100$ whereas when $\Delta = T_c/4$, we use $P = 200$. This is because to achieve $\Delta = T_c/4$, more pilot symbols are needed to guarantee the accuracy of synchronization. From Fig. 4.1, it is observed that the system BER performance when $\Delta = T_c/4$ gets very close to that under perfect synchronization. Even the system under coarse synchronization can achieve the BER of 10^{-2} when E_b/N_o is 19 dB.

Using the same system parameters, we plot the occurrence of TOA estimation errors at E_b/N_o of 24 dB in Fig. 4.2. It is found that with the decrease of synchronization level Δ, the TOA estimation error variance is substantially reduced.

4.3.2 Combination of Synchronization and Power Control

In Chapter 3, we studied the proposed d^{2}TD-IR system without power control. The d^{2}TD-IR system BER performances with and without power control are compared in Fig. 4.3 for various values of chip duration, T_c, with $N_u = 10$ and $N_s = 2$ fixed. In the graph, "WPC" stands for the system with perfect power control. From Fig. 4.3, it is observed that with perfect power control, the error floors

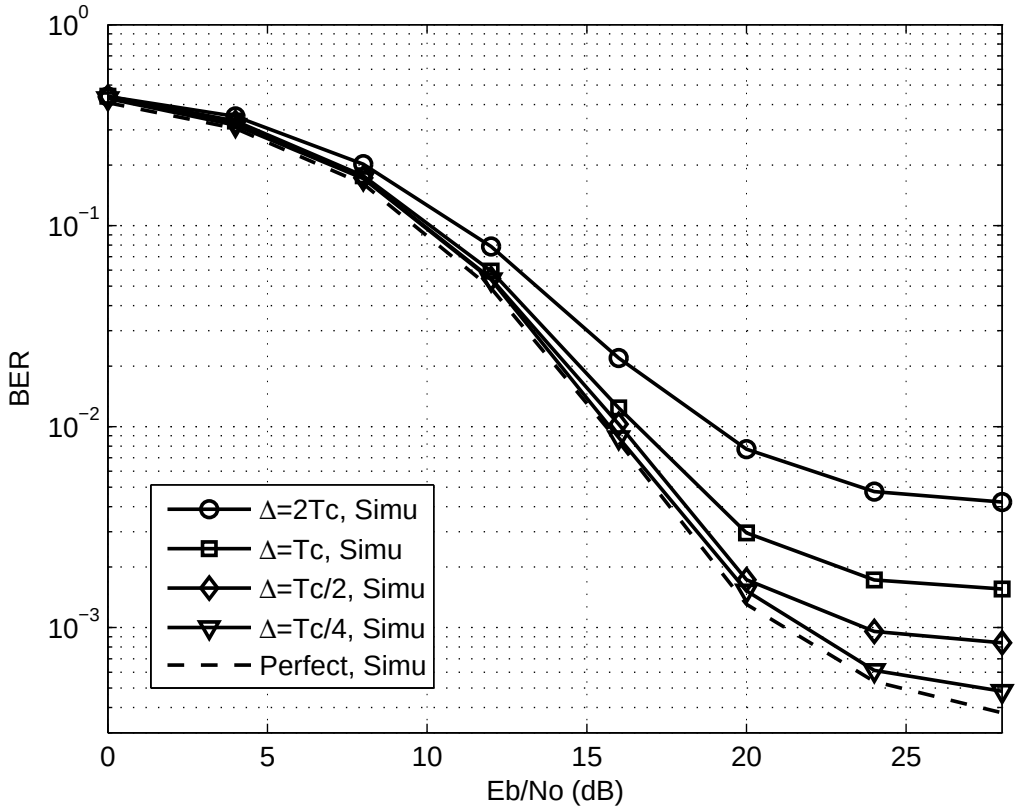

Fig. 4.1: BER versus E_b/N_o; comparison of ten-user d^2 TD-IR system after synchronization, where $\Delta = 2T_c,\ T_c,\ T_c/2,$ and $T_c/4$, with that under perfect synchronization, $T_c = 10.688$ ns, $N_s = 2$.

at high E_b/N_o reduce significantly. The system with $T_c = 10.020$ ns can reach the BER of 3×10^{-6} when E_b/N_o is greater than 20 dB. The results are reasonable because the error floors are due to the multiuser interference (MUI) and power control aims at reducing MUI.

In Fig. 4.4, we compare the BER performance of the d^2TD-IR system after the recursive algorithm which combines synchronization and power control with that under perfect synchronization and power control. The system parameters are the same with the Sub-section 4.3.1 except that the parameter P for all the

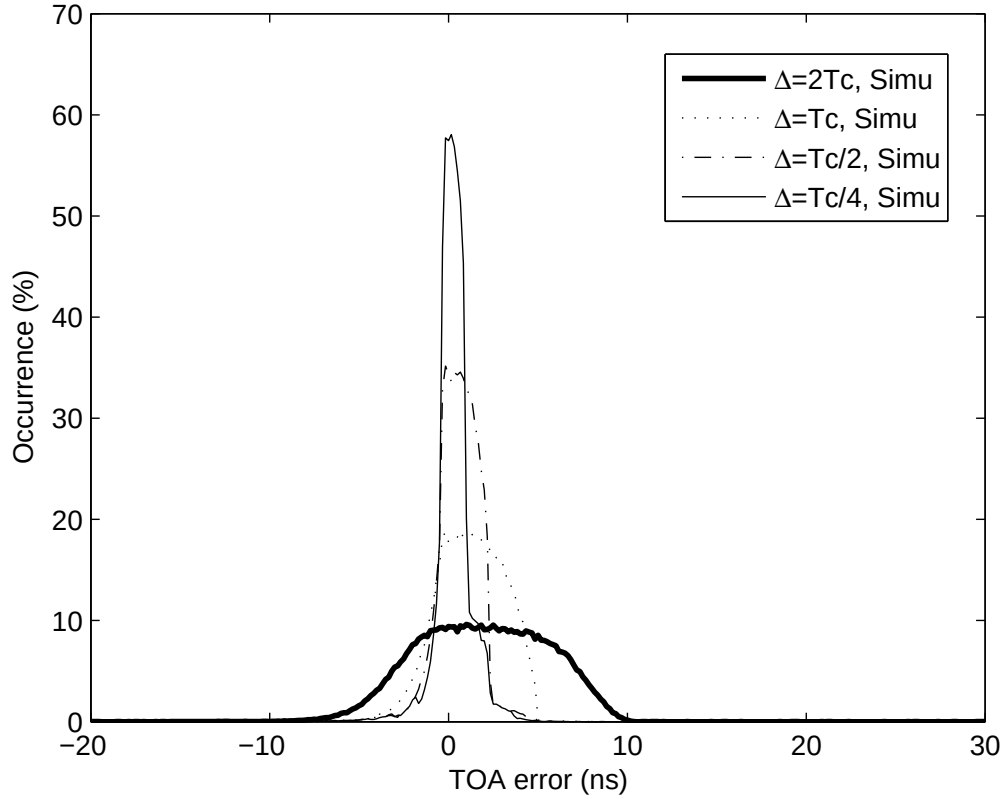

Fig. 4.2: TOA estimation error distribution of ten-user d^2TD-IR system after synchronization, where $\Delta = 2T_c,\ T_c,\ T_c/2,$ and $T_c/4$, at E_b/N_o of 24 dB, $T_c = 10.688$ ns, $N_s = 2$.

BER performance curves is set to be 100. From Fig. 4.4, it is observed that the system BER performance when $\Delta = T_c/4$ gets very close to that under perfect synchronization and perfect power control.

Compared with a non-recursive algorithm, the recursive algorithm has a property that the acquisition time is not deterministic. To examine the efficiency of our proposed algorithm, we compute the mean acquisition time (MAT) of the proposed d^2TD-IR system. In this thesis, the MAT is defined as the average time duration, or (average number of pilot symbols) $\times$ (symbol duration), to achieve the required

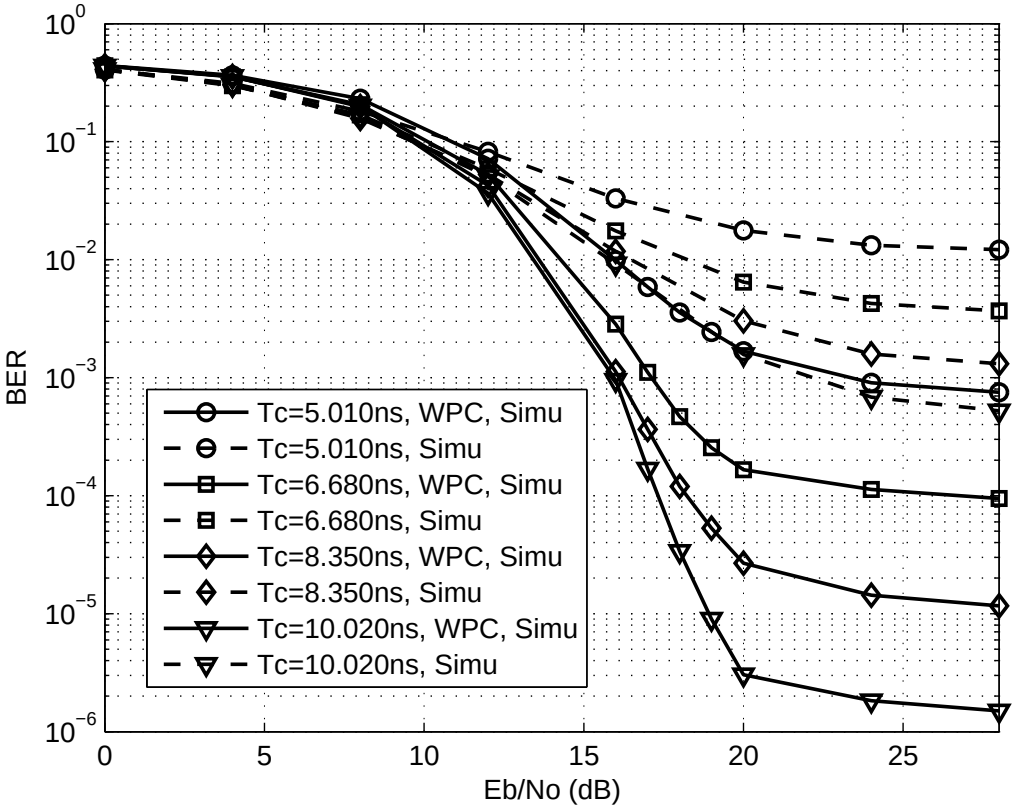

Fig. 4.3: BER versus E_b/N_o for various T_c values with $N_s = 2$; comparison of ten-user d^2TD-IR system with and without power control.

synchronization level over different channel realizations. Using the same system parameters, the MAT at various E_b/N_o are plotted in Fig. 4.5. It is noticed that the MAT remains the same for the d^{2}TD-IR system when $\Delta = 2T_c$. This is because to achieve $\Delta = 2T_c$ requires only Step 1 of the proposed algorithm and no recursive requirement for Step 1. For the d^{2}TD-IR system when $\Delta = T_c,\ T_c/2,$ and $T_c/4$, it is found that with the increase of E_b/N_o, the MAT reduces dramatically. At E_b/N_o of 24 dB, to achieve $\Delta = T_c/4$ only requires a MAT of about 0.11 ms or about 510 pilot symbols on average.

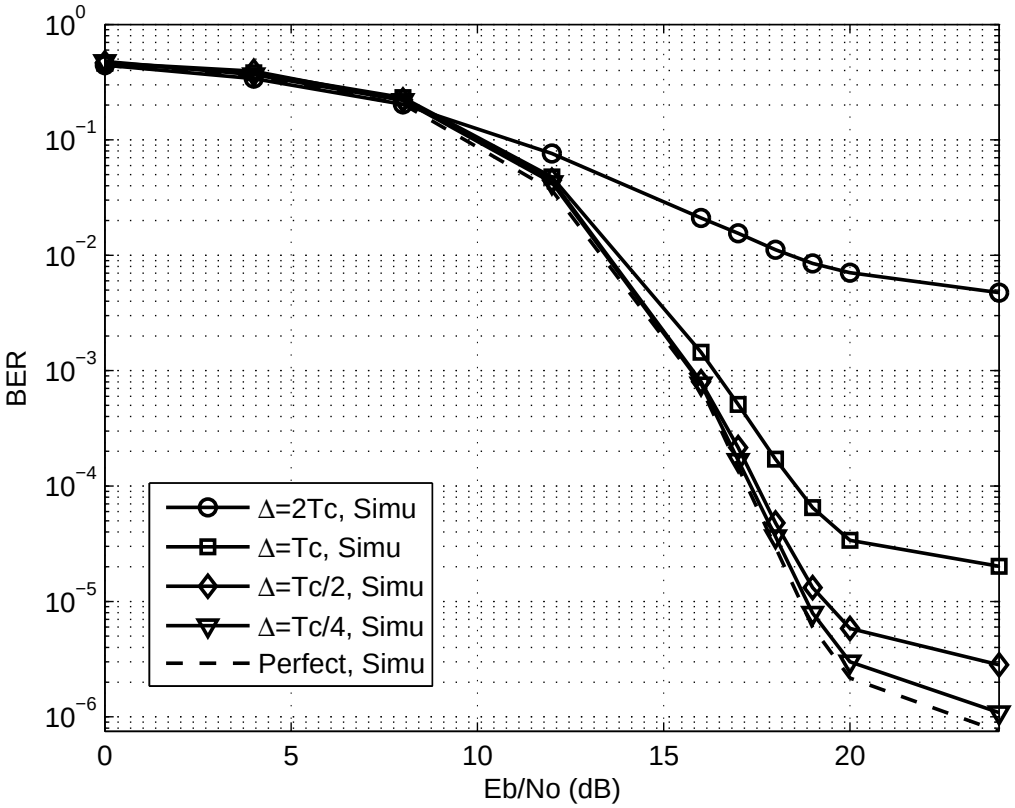

Fig. 4.4: BER versus E_b/N_o; comparison of ten-user d^2TD-IR system after combined synchronization and power control process, where $\Delta = 2T_c,\ T_c,\ T_c/2,$ and $T_c/4$, with that under perfect synchronization and power control, $T_c = 10.688$ ns, $N_s = 2$.

4.4 Summary

In this chapter, the methods for synchronization and power control of the d^2TD-IR system were discussed. We proposed a TOA based algorithm for synchronization and a recursive algorithm which combines synchronization and power control. The simulations were provided to show the effectiveness and efficiency of the two algorithms.

With the proposed synchronization and power control algorithms, the d^2TD-IR

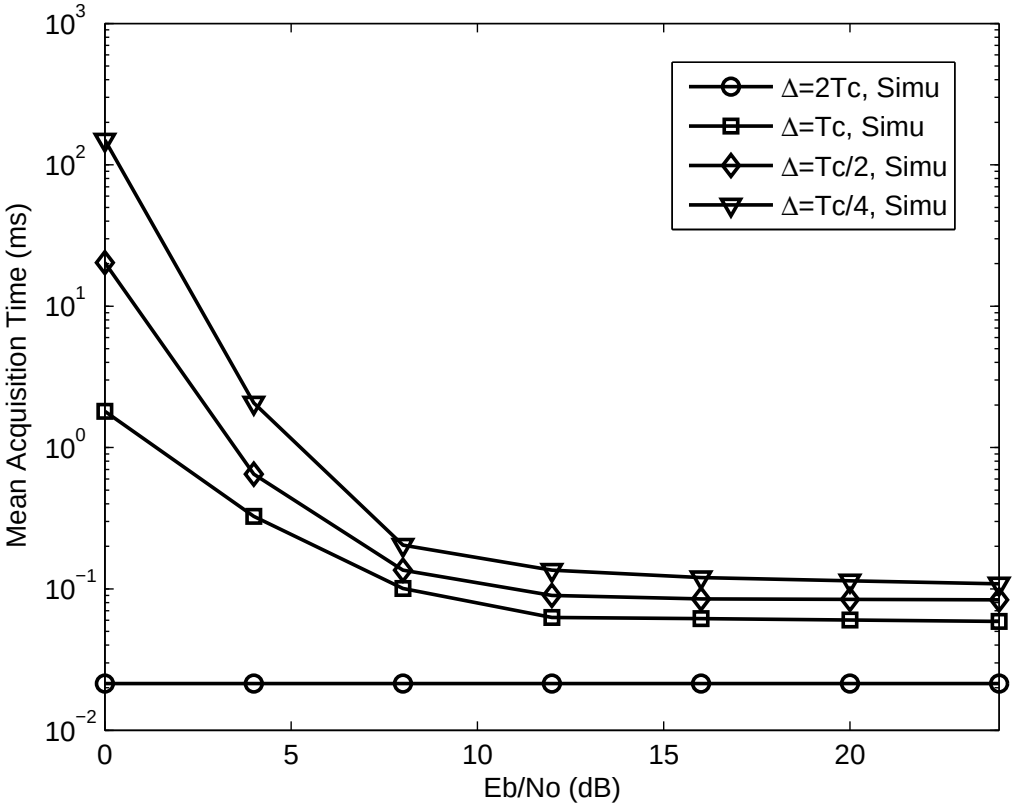

Fig. 4.5: MAT versus E_b/N_o; ten-user d^2 TD-IR system after combined synchronization and power control process, where $\Delta = 2T_c,\ T_c,\ T_c/2,$ and $T_c/4$, $T_c = 10.688$ ns, $N_s = 2$.

system performs well. To further reduce the transmission power while maintaining low bit-error-rate (BER), we are required to incorporate powerful channel coding schemes, such as LDPC codes, into the proposed d^2TD-IR system which will be discussed in the next chapter.

Chapter 5

LDPC Coded and LDPC Product Coded d^2TD-IR Systems

For UWB systems, FCC prescribes that the power spectral density of transmit signal should be as low as 75 nW/MHz. To satisfy the requirement, the proposed d^2TD-IR system should reduce the transmission power as much as possible. To lower the transmission power while maintaining system bit-error-rate (BER) performance, a possible method is to employ powerful channel coding schemes. In this chapter, we examine the effects of low-density parity-check (LDPC) codes [52] on our proposed d^2TD-IR system. We have chosen LDPC codes as the channel coding scheme since they are well known for their abilities to achieve near Shannon channel capacity limit with low decoding complexity compared with a Turbo decoder [56].

Another purpose of this chapter is to study the performance of LDPC product coded d^2TD-IR system. In Appendix B, we present a type of LDPC product

codes, which can significantly lower the encoding complexity at the expense of slight degradation in error-rate performance as well as slight increase in decoding complexity. It is interesting to know whether the two codes, LDPC codes and LDPC Product codes, can achieve similar BER performances when they are applied to the proposed d^2TD-IR system.

Here, we first briefly introduce LDPC codes. Details on LDPC product codes are given in Appendix B. The performances of LDPC coded and LDPC product coded d^2TD-IR systems are then studied through computer simulations.

5.1 LDPC Codes

Low-density parity-check (LDPC) codes were originally invented and investigated by Gallager [52] in early 1960s. After being "shelved" for about 35 years, this class of codes had been recently rediscovered and shown to form another class of Shannon-limit approaching codes, besides turbo codes [56].

The idea of LDPC codes was inspired by Shannon's noisy channel coding theorem. It states that there exist channel codes (and decoder) with correspondingly large code lengths such that the probability of decoding error can be as small as desired, if the transmission rate $R < C$, where C is the channel capacity. Shannon used random selected codes to prove his theorem. The same idea was used in the random generation of parity check matrices of LDPC codes, which contain mostly zero's and relatively few one's. In [52], Gallager also invented a powerful iterative decoding algorithm called belief propagation algorithm (also referred to as message-passing algorithm) for LDPC codes, whose complexity increases linearly with the code lengths. The low-complexity decoding algorithm was found to per-

forms amazingly well. It was shown that a carefully constructed rate 1/2 irregular LDPC code with long block length can achieve a bit error probability of 10^{-6} at just 0.13 dB away from Shannon capacity for AWGN channels [55].

A binary (N, K, λ, ρ) LDPC code is a linear block code which has length N, dimension K, an $(N-K) \times N$ parity-check matrix $\mathbf{H}$ with average column (row)-weight λ (ρ), and a generator matrix $\mathbf{G}$. In the parity check matrix $\mathbf{H}$, the ones are placed at random, as seen in Table 5.1. The corresponding bipartite graph consists of N variable nodes, $(N-K)$ check nodes, and a certain number of edges [55]. The N variable nodes correspond to the N entries of the codeword. The $N-K$ check nodes correspond to the $N-K$ parity check constraints which define the code. An edge exists between a variable node and a check node if and only if there is a one in the corresponding entry in the parity check matrix. If the parity check matrix contains the same number of ones in every column and the same number of ones in every row, the code is known as a regular LDPC code; otherwise, it is called irregular LDPC code. In contrast to $\mathbf{H}$, the generator matrix $\mathbf{G}$ is dense. Consequently, the number of bit operations at the encoder grows with the square of the code length.

The LDPC codes have the following advantages over other channel coding schemes [87]:

- the LDPC decoder usually has a much lower computational complexity than the turbo-code decoder. Moreover, the decoding of LDPC is highly parallelizable;

- The minimum distance of binary LDPC codes increases linearly with the block length with probability close to 1 [52];

1	1	1	1	0	0	0	0	0	0	0	0	0	0	0	0	0	0	0
0	0	0	0	1	1	1	1	0	0	0	0	0	0	0	0	0	0	0
0	0	0	0	0	0	0	0	1	1	1	1	0	0	0	0	0	0	0
0	0	0	0	0	0	0	0	0	0	0	0	1	1	1	1	0	0	0
0	0	0	0	0	0	0	0	0	0	0	0	0	0	0	0	1	1	1
1	0	0	0	1	0	0	0	1	0	0	0	1	0	0	0	0	0	0
0	1	0	0	0	1	0	0	0	1	0	0	0	0	0	0	1	0	0
0	0	1	0	0	0	1	0	0	0	0	0	0	1	0	0	0	1	0
0	0	0	1	0	0	0	0	0	0	1	0	0	0	1	0	0	0	1
0	0	0	0	0	0	0	1	0	0	0	1	0	0	0	1	0	0	0
1	0	0	0	0	1	0	0	0	0	0	1	0	0	0	0	0	1	0
0	1	0	0	0	0	1	0	0	0	1	0	0	0	0	1	0	0	0
0	0	1	0	0	0	0	1	0	0	0	0	1	0	0	0	0	0	1
0	0	0	1	0	0	0	0	1	0	0	0	0	1	0	0	1	0	0
0	0	0	0	1	0	0	0	0	1	0	0	0	0	1	0	0	0	0

Table 5.1: Example of the parity check matrix of an LDPC code for $N = 20$, $K = 5$, $\lambda = 3$ and $\rho = 4$.

- Compared with other types of forward error correction (FEC) block codes, LDPC code with any block-length and any code rate is easier to design, which makes the code scalable according to our requirement;
- LDPC codes do not typically show an error floor, which is suitable for short-frame applications;
- Due to the random generation of parity-check matrix, the coded bits have been efficiently interleaved; therefore, no extra interleaver is needed;
- LDPC codes have hard decision decoding algorithms as well as soft decision decoding algorithms, whereas turbo codes only have soft decision decoding

algorithms. This makes LDPC codes more flexible than turbo codes.

5.2 LDPC Coded d^2TD-IR Systems

The block diagram of the LDPC coded d^2TD-IR system is shown in Fig. 5.1. Let $\mathbf{x} = [x_1, x_2, \cdots, x_K]$ denote the information vector sent by the k^{th} user in the LDPC coded d^2TD-IR system. The vector $\mathbf{x}$ is encoded into a codeword $\mathbf{y} = [y_1, y_2, \cdots, y_N]$ by an LDPC encoder, whose parity check matrix is $\mathbf{H}$. The unipolar binary entries, y_i, of the codeword $\mathbf{y}$ are then converted to polar binary form using

$$b_i^{(k)} = (1 - 2y_i) \text{ for } i = 1, 2, \cdots, N, \tag{5.1}$$

which represents the transmitted symbol of the k^{th} user. The symbols $b_1^{(k)} b_2^{(k)} \cdots b_N^{(k)}$ are differentially encoded and then transmitted using a train of short pulses as in the d^2TD-IR system.

The transmitted signals propagate through the UWB channel and arrive at the receiver. The delay-sum AcR of d^2TD-IR system integrates and samples the received signals. The sampled results $\{D_i^{(k)}\}$, as defined in (3.8) are then sent to LDPC decoder. The log-likelihood for the symbol y_i, $i = 1, 2, \cdots, N$, is expressed as

$$\mathrm{M}_0(y_i) = \log \frac{\Pr\left\{ y_i = 0 \,\middle|\, D_i^{(k)} \right\}}{\Pr\left\{ y_i = 1 \,\middle|\, D_i^{(k)} \right\}}. \tag{5.2}$$

We implement the soft decision belief propagation (BP) based algorithm for de-

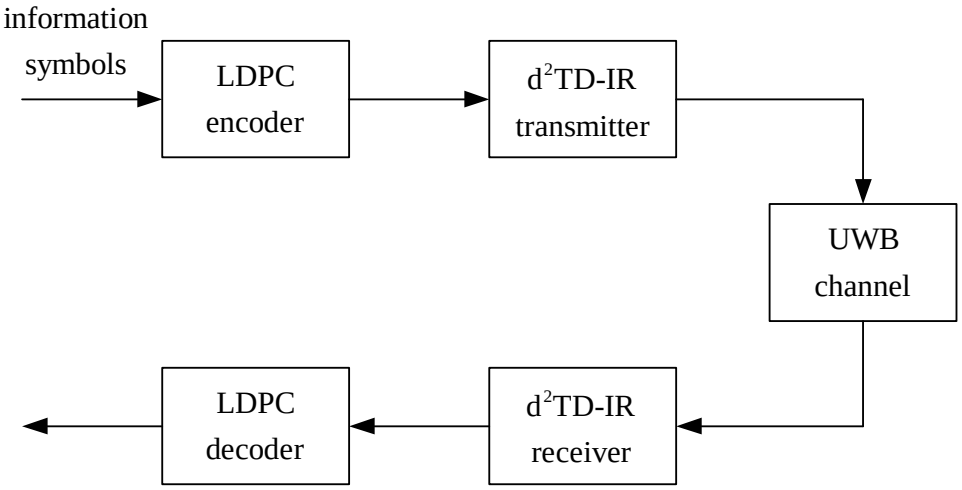

Fig. 5.1: Block diagram of LDPC coded d^2 TD-IR system.

coding. The update equations for the messages under BP are as follows [53]

$$\mathrm{M}_{vc}^{(l)} = \begin{cases} \mathrm{M}_0; & \text{if } l = 0 \\ \mathrm{M}_0 + \sum_{c' \in C_v \backslash \{c\}} \mathrm{M}_{c'v}^{(l-1)}; & \text{if } l \geq 1, \end{cases} \tag{5.3}$$

$$\mathrm{M}_{cv}^{(l)} = \mathrm{In} \frac{1 + \prod_{v' \in V_c \backslash \{v\}} \tanh\left(\mathrm{M}_{v'c}^{(l)}/2\right)}{1 - \prod_{v' \in V_c \backslash \{v\}} \tanh\left(\mathrm{M}_{v'c}^{(l)}/2\right)} \tag{5.4}$$

where C_v is the set of check nodes that are incident on the variable node v, and V_c is the set of variable nodes that are incident on the check node c. $\mathrm{M}_{vc}^{(l)}$ is the message of the variable node v that is transferred to the check nodes c during l^{th} iteration. $\mathrm{M}_{cv}^{(l)}$ is the message of the variable node c that is transferred to the check nodes v during l^{th} iteration.

After each iteration, the probability of each bit being 1 or 0 in terms of its likelihood is simply

$$\Pr\{y_i = 0\} = \frac{e^{\mathrm{M}_l}}{1 + e^{\mathrm{M}_l}}, \tag{5.5}$$

$$\Pr\{y_i = 1\} = \frac{1}{1 + e^{\mathrm{M}_l}} \tag{5.6}$$

where

$$\mathrm{M}_l = \mathrm{M}_0 + \sum\nolimits_{c \in C_v} \mathrm{M}_{cv}^{(l-1)}. \tag{5.7}$$

The decoder decides that

$$\widehat{y}_i^{(l)} = \begin{cases} 0; & \text{if } \mathrm{M}_l \geq 0 \\ 1; & \text{if } \mathrm{M}_l < 0 \end{cases} \tag{5.8}$$

where $\widehat{y}_i^{(l)}$ is the tentative decoding result for y_i after l^{th} iteration. Denote $\widehat{\mathbf{y}}^{(l)} = [\widehat{y}_1^{(l)}, \widehat{y}_2^{(l)}, \cdots, \widehat{y}_N^{(l)}]$. If $\widehat{\mathbf{y}}^{(l)}\mathbf{H}^{\dagger} = \mathbf{0}$ or the maximum number of iterations has been reached, the BP algorithm stops, otherwise it continues.

5.3 Simulation Results

In Fig. 5.2, we compare bit-error-rate (BER) performances of the d^2TD-IR system with and without LDPC coding. The d^2TD-IR system parameters are $T_c = 10.688$ ns, $N_s = 2$ and $N_u = 10$. In the simulations, the random channels are generated according to [44]. The channel model is CM 1, $0 \sim 4$ meters' range with line-of-sight (LOS) model. The signals arriving at the receiver are perfectly time-synchronized and power controlled. For the LDPC coded system, the $(9000, 4500, 3, 6)$ LDPC code are used to encode and decode the information symbols. Decoding is carried out with the BP algorithm [53] where the maximum iteration number is set at 12. To obtain the value of a posteriori probability (APP) $\Pr\{y_i | D_i^k\}$ of the symbol y_i, pilot symbols are transmitted before the transmission of LDPC coded symbols to achieve the estimated desired signal power and noise

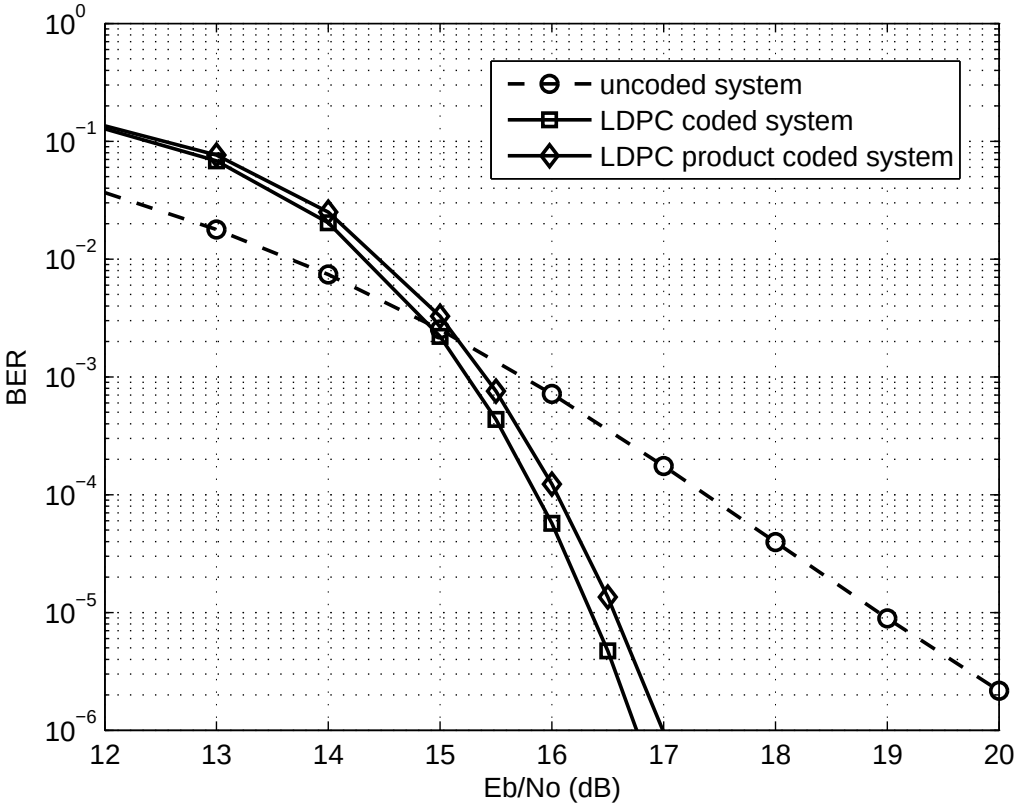

Fig. 5.2: BER versus E_b/N_o; comparison of ten-user d^2 TD-IR system with and without LDPC coding, $T_c = 10.688$ ns, $N_s = 2$.

(including multiuser interference and channel noise) level. From Fig. 5.2, it is observed that the LDPC coded system achieves about 3 dB coding gain at the BER of 3×10^{-6}. The coding gain is less than that of LDPC coded narrowband system in additive white Gaussian noise (AWGN) channel. This is because the BER performance presented in the figure is the average performance over different UWB channel realizations. It is possible that some users in the system undergo deep fadings, under this condition, a large number of decoding errors will occur, causing the average BER to increase.

In Appendix B, we propose a type of LDPC product codes, which can significantly lower the encoding complexity at the expense of slight degradation in error-rate performance as well as slight increase in decoding complexity. The LDPC product code with $N = 9000$, $K = 4500$ and $\lambda = 4$ in the simulations of Appendix B is used to encode and decode the transmitted symbols of the d^2TD-IR system. It is found that the LDPC product code achieves almost similar coding gain compared to the LDPC code. At the BER of 3×10^{-6}, the coding gain only reduces by about 0.3 dB.

5.4 Summary

In this chapter, we proposed to implement LDPC coding and LDPC product coding schemes to encode and decode the transmitted symbols of d^2TD-IR system. Computer simulations were provided to compare the BER performance of LDPC coded and uncoded systems.

While powerful channel coding schemes, such as LDPC codes or LDPC product codes are most effective for AWGN channel, their performance may deteriorate when the coded signal is subjected to long periods of deep fade encountered in slow or static fading channels. A method to combat fading is to introduce diversity through the multiple-input-multiple-output (MIMO) implementation. In the next chapter, we will extend the proposed d^2TD-IR system into a MIMO system and investigate its performance.

Chapter 6

Differential Space-Time Coded MIMO d^2TD-IR Systems

In the proposed d^2TD-IR system, the transmitted signals from each user propagate through a UWB channel. Multipath components arriving at the receiver can cause significant performance degradation of the system if they are not properly mitigated or exploited to advantage. A method to combat multipath fading is to introduce diversity. It is well known that spatial diversity can be achieved using multiple-input multiple-output (MIMO) scheme, which employs multiple antennas at the transmitter and the receiver. In this chapter, we propose a differential space-time coded (DSTC) MIMO d^2TD-IR system and examine its performance in standard UWB channels [44].

Here, we first consider the simplest scenario where the d^2TD-IR system is a single user system and has a spreading factor of one. Under these conditions, we extend the proposed d^2TD-IR to a DSTC MIMO system. An equivalent system

model is derived in Section 6.2. Through the discussion of the design criteria of DSTC, we propose maximum distance codes for our system in Section 6.3. Computer simulation results are presented and discussed in Section 6.4.

The performance of DSTC MIMO d^{2}TD-IR is also examined in a multiuser environment using computer simulations in Section 6.4.

6.1 System Description

We consider a single user d^{2}TD-IR system with P transmit and Q receive antennas operating in a quasi-static UWB environment, of which the block diagram is shown in Fig. 6.1. It is assumed that the elements of the transmit and receive antenna arrays are spaced more than the coherence distance so that the channel coefficients for different transmit-receive antenna pairs are statistically independent.

6.1.1 The Transmitter

The use of matrix multiplication in differential encoding was first introduced in [62, 63] for differential unitary space-time modulation. Here, we adopt a similar approach where we let

$$\Omega = \left\{ \mathbf{U}^{(1)}, \mathbf{U}^{(2)}, \cdots, \mathbf{U}^{(N_\Omega)} \right\} \tag{6.1}$$

be a set of possible $N \times N$ orthogonal message matrices where each matrix has elements belonging to the set $\{-1, 0, 1\}$. In (6.1), the integer $N_\Omega \geq 2$ denotes the cardinality of the orthogonal constellation.

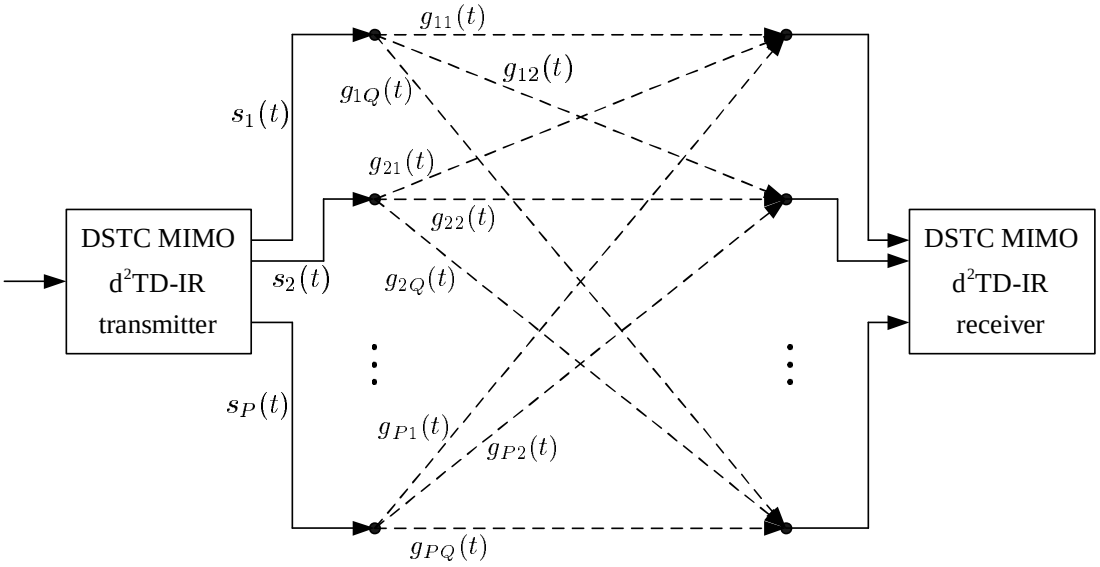

Fig. 6.1: DSTC MIMO d² TD-IR system block diagram.

The transmission block $\mathbf{D}_k$ for the k^{th} message matrix $\mathbf{U}_k \in \Omega$ is obtained by

$$\mathbf{D}_k = \mathbf{D}_{k-1}\mathbf{U}_k. \tag{6.2}$$

The initial (or reference) transmission block, $\mathbf{D}_0$, is chosen to be a $P \times N$ matrix ($P \leq N$) with elements belonging to the set $\{-1, 1\}$, and which satisfies

$$\mathbf{D}_0\mathbf{D}_0^{\dagger} = N\mathbf{I}_P \tag{6.3}$$

where $\dagger$ denotes the transpose operation, and $\mathbf{I}_P$ the $P \times P$ identity matrix. $\mathbf{D}_0$ thus adapts the message matrices in Ω for transmission with P antennas. Because $\mathbf{U}_k : k = 1, 2, \cdots$ are square orthogonal matrices with only one non-zero entry, (-1 or 1), per row and column, it is easy to see that $\mathbf{D}_k : k = 1, 2, \cdots$ will also be

$P \times N$ matrices with elements belonging to the set $\{-1, 1\}$, and which satisfy

$$\mathbf{D}_k \mathbf{D}_k^{\dagger} = N\mathbf{I}_P;\ k = 1, 2, \cdots . \tag{6.4}$$

The column of $\mathbf{D}_k$, are referred to as space-time symbols. Let

$$\mathbf{d}_{k,n} = [d_{1,kN+n-1}, d_{2,kN+n-1}, \cdots, d_{p,kN+n-1}, \cdots, d_{P,kN+n-1}]^{\dagger} \tag{6.5}$$

denote the space-time symbol transmitted at time $t = (kN + n - 1)\, T$. We define

$$\widetilde{\mathbf{D}}_{k,n} = [\mathbf{d}_{k,1-n}, \mathbf{d}_{k,2-n}, \cdots \mathbf{d}_{k,N-n}] \text{ and } \widetilde{\mathbf{D}}_{k,0} = \mathbf{D}_k \tag{6.6}$$

as a block of N consecutive space-time symbols where $\widetilde{\mathbf{D}}_{k,0}$ represents the k^{th} transmission block $\mathbf{D}_k$. Because the spreading factor is 1, each element in $\mathbf{D}_k$ is used to amplitude modulate a causal wideband monocycle, $\omega(t)$, which begins at $t = 0$ and has a support length of $T_\omega\, (\ll T)$ where T is the symbol duration. The transmitted signal from the p^{th} antenna then has the form

$$s_p(t) = \sum_{k=0}^{\infty} \sum_{n=1}^{N} d_{p,kN+n-1} \omega\left(t - (kN + n - 1)\, T\right) = \sum_{j=0}^{\infty} d_{p,j} \omega\left(t - jT\right) \tag{6.7}$$

where $j = kN + n - 1$.

6.1.2 The Channel Model

Following [12] and [66], we consider a quasi-static dense multipath fading environment and assume the channel coefficients for different transmit-receive antenna pairs to be statistically independent. The random channels are generated

according to [44]. The clusters, and the rays within each cluster, arrive as Poisson random points in time. The amplitudes of the clusters and the rays are log-normal distributed with exponentially decaying mean square values. Simplifying the notation, we model the impulse response of the channel between the p^{th} transmit antenna and the q^{th} receive antenna as

$$g_{pq}(t) = \sum_{l=1}^{L_{pq}} \alpha_{pq,l} \delta(t - \tau_{pq,l}) \tag{6.8}$$

where L_{pq} denotes the number of propagation paths, $\alpha_{pq,l}$ and $\tau_{pq,l}$ are the random amplitude and delay associated with the l^{th} path. The signals arriving at the receiver are assumed to be perfectly synchronized. Hence the path delays are normalized with $\min[\tau_{pq,1}]$ set to zero.

Let $h_{pq}(t)$ be the overall channel response to the monocycle, $\omega(t)$, given by

$$h_{pq}(t) = \omega(t) \otimes g_{pq}(t) = \sum_{l=1}^{L_{pq}} \alpha_{pq,l} \omega(t - \tau_{pq,l}) \tag{6.9}$$

where $\otimes$ denotes convolution. The received signal at the q^{th} receiver antenna then has the form

$$r_q(t) = \sum_{p=1}^{P} \sum_{j=0}^{\infty} d_{p,j} h_{pq}(t - jT) + n_q(t) \tag{6.10}$$

where $n_q(t)$ is a bandlimited additive white Gaussian noise (AWGN) process with autocorrelation function

$$R_{n,q}(\tau) = N_o W \operatorname{sinc}(W\tau) \tag{6.11}$$

where $N_o/2$ and W ($\gg 1/T_\omega \gg 1/T$) are, respectively, the power spectral density

of the AWGN and the bandwidth of the system lowpass filter. The signal-to-noise ratio, E_b/N_o, of the system is defined as $\frac{P}{N_o}\int_0^{T_\omega}\omega^2(t)\,dt$.

6.1.3 The Receiver

To implement the autocorrelation receiver, we use $r_q(t)$ in (6.10) to form the matrix

$$\mathbf{Y}_k(t)=\begin{pmatrix} r_1(t+kNT) & r_1(t+kNT+T) & \cdots & r_1(t+kNT+(N-1)T) \\ r_2(t+kNT) & r_2(t+kNT+T) & \cdots & r_2(t+kNT+(N-1)T) \\ \cdots & \cdots & \cdots & \cdots \\ r_Q(t+kNT) & r_Q(t+kNT+T) & \cdots & r_Q(t+kNT+(N-1)T) \end{pmatrix} \tag{6.12}$$

where $\mathbf{Y}_k(t)$ is treated as a matrix of continuous time waveforms. The decision statistics, $\mathbf{R}_k$, for detecting the k^{th} message block, $\mathbf{U}_k$, is then obtained as

$$\mathbf{R}_k=\int_0^T \mathbf{Y}_k^{\dagger}(t)\,\mathbf{Y}_{k-1}(t)\,dt \tag{6.13}$$

where $\mathbf{R}_k$ is an $N\times N$ matrix, whose u^{th}-row and v^{th}-column element is given by

$$[\mathbf{R}_k]_{u,v}=\sum_{q=1}^{Q}\int_0^T r_q(t+kNT+(u-1)T)\,r_q(t+(k-1)NT+(v-1)T)\,dt. \tag{6.14}$$

Following [62], the receiver computes

$$\widehat{\mathbf{U}}_k=\arg\max_{\mathbf{U}\in\Omega}\mathrm{Tr}(\mathbf{U}\mathbf{R}_k) \tag{6.15}$$

where "Tr $(\cdot)$" denotes the trace of a matrix. The receiver structure $P = Q = N = 2$ is illustrate in Fig. 6.2.

6.2 Equivalent System Model

In this section, we derive an equivalent system model to evaluate the performance of the proposed single user DSTC MIMO d^2TD-IR system in the UWB channel.

Begin by assuming that the channel impulse response has a finite memory length such that $h_{pq}(t) = 0$ when $t > MT$, where M is a positive integer. We may then partition $h_{pq}(t)$ into M contiguous time slices of duration T, and express it as

$$h_{pq}(t) = \sum_{m=1}^{M} h_{pq}(t)\,\tilde{p}(t-(m-1)T) \tag{6.16}$$

where $\tilde{p}(t) = \begin{cases} 1;\ 0 \le t < T \\ 0;\ \text{otherwise} \end{cases}$. Applying (6.16) into (6.10), it can be shown that

$$\begin{aligned} r_q(t+kNT+(\varsigma-1)T)\,\tilde{p}(t) = &\sum_{p=1}^{P}\sum_{m=1}^{M} d_{p,kN+\varsigma-m} h_{pq,m}(t) \\ &+ n_q(t+kNT+(\varsigma-1)T)\,\tilde{p}(t) \end{aligned} \tag{6.17}$$

where

$$h_{pq,m}(t) = h_{pq}(t+(m-1)T)\,\tilde{p}(t);\ m = 1,2,\cdots,M \tag{6.18}$$

is the channel response in the time interval $(m-1)T \le t < mT$ at the q^{th} receive antenna to a monocycle transmitted at time $t = 0$ by the p^{th} transmit antenna.

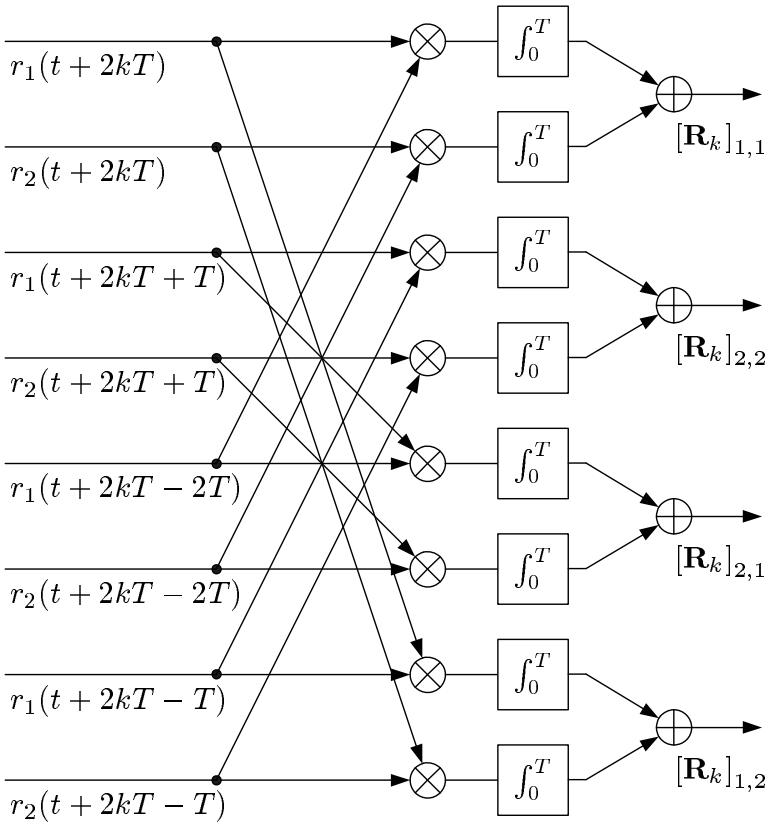

Fig. 6.2: MIMO AcR block diagram for $P = Q = N = 2$.

Using (6.17), we may now express (6.14) as

$$[\mathbf{R}_k]_{u,v} = [\mathbf{S}_k]_{u,v} + [\mathbf{N}_k]_{u,v} \tag{6.19}$$

where

$$[\mathbf{S}_k]_{u,v}=\sum_{q=1}^{Q}\int_0^T\left[\left(\sum_{p=1}^{P}\sum_{m=1}^{M}d_{p,kN+u-m}h_{pq,m}\left(t\right)\right)\times\left(\sum_{p=1}^{P}\sum_{m=1}^{M}d_{p,(k-1)N+v-m}h_{pq,m}\left(t\right)\right)\right]dt$$
$$=\sum_{p'=1}^{P}\sum_{m'=1}^{M}\sum_{p''=1}^{P}\sum_{m''=1}^{M}\left[d_{p',kN+u-m'}d_{p'',(k-1)N+v-m''}\sum_{q=1}^{Q}\int_0^T h_{p'q,m'}\left(t\right)h_{p''q,m''}\left(t\right)dt\right] \tag{6.20}$$

and

$$[\mathbf{N}_k]_{u,v}=A_1+A_2+A_3 \tag{6.21}$$

in which

$$A_1=\sum_{p=1}^{P}\sum_{m=1}^{M}d_{p,(k-1)N+v-m}\sum_{q=1}^{Q}\int_0^T h_{pq,m}\left(t\right)n_q\left(t+kNT+\left(u-1\right)T\right)dt, \tag{6.22}$$

$$A_2=\sum_{p=1}^{P}\sum_{m=1}^{M}d_{p,kN+u-m}\sum_{q=1}^{Q}\int_0^T h_{pq,m}\left(t\right)n_q\left(t+\left(k-1\right)NT+\left(v-1\right)T\right)dt, \tag{6.23}$$

$$A_3=\sum_{q=1}^{Q}\int_0^T n_q\left(t+kNT+\left(u-1\right)T\right)n_q\left(t+\left(k-1\right)NT+\left(v-1\right)T\right)dt. \tag{6.24}$$

With $[\mathbf{S}_k]_{u,v}$ and $[\mathbf{N}_k]_{u,v}$ forming the u^{th}-row and v^{th}-column elements of $\mathbf{S}_k$ and $\mathbf{N}_k$, respectively, we may express the decision statistics $\mathbf{R}_k$ in (6.13) as

$$\mathbf{R}_k=\mathbf{S}_k+\mathbf{N}_k. \tag{6.25}$$

In (6.18), $\{h_{pq,m}\left(t\right):m\in[1,M],p\in[1,P],q\in[1,Q]\}$ is a set of independent random processes defined over the interval $[0,T]$ with each process defined by a train of wideband monocycles with independent inter-arrival times. When $m'\neq m''$ or

$p' \neq p''$, the occurrence of a monocycle in $h_{p'q,m'}(t)$ in perfect alignment with a monocycle in $h_{p''q,m''}(t)$ has zero probability. Hence, if the support length, T_ω, of the monocycles is extremely short and the symbol duration, $T\,(\gg T_\omega)$, is sufficiently long to collect a large number of multipath components (a hundred or more in our case) we may omit those $p' \neq p''$ and/or $m' \neq m''$ terms in (6.20) to obtain the approximation

$$\begin{aligned}
[\mathbf{S}_k]_{u,v} &\simeq \sum_{p=1}^{P}\sum_{m=1}^{M}\left[d_{p,kN+u-m}d_{p,(k-1)N+v-m}\sum_{q=1}^{Q}\mathcal{E}_{pq,m}\right] \\
&= \sum_{p=1}^{P}\left[d_{p,kN+u-1}d_{p,(k-1)N+v-1}\sum_{q=1}^{Q}\mathcal{E}_{pq,1}\right] \\
&+ \sum_{m=2}^{M}\sum_{p=1}^{P}\left[d_{p,kN+u-m}d_{p,(k-1)N+v-m}\sum_{q=1}^{Q}\mathcal{E}_{pq,m}\right]
\end{aligned} \tag{6.26}$$

where

$$\mathcal{E}_{pq,m} = \int_0^T h_{pq,m}^2(t)\,dt, \tag{6.27}$$

with negligible loss of accuracy. The signal matrix, $\mathbf{S}_k$, can now be written as

$$\mathbf{S}_k = \mathbf{D}_k^\dagger \mathbf{H}_1 \mathbf{D}_{k-1} + \sum_{m=1}^{M-1}\widetilde{\mathbf{D}}_{k,m}^\dagger \mathbf{H}_{m+1}\widetilde{\mathbf{D}}_{k-1,m} \tag{6.28}$$

where $\mathbf{D}_k = \widetilde{\mathbf{D}}_{k,0}$ as defined in (6.6), and

$$\mathbf{H}_m = \mathrm{diag}\left[\sum_{q=1}^{Q}\mathcal{E}_{1q,m}, \sum_{q=1}^{Q}\mathcal{E}_{2q,m}, \cdots, \sum_{q=1}^{Q}\mathcal{E}_{Pq,m}\right] \tag{6.29}$$

To simplify our analysis of $[\mathbf{N}_k]_{u,v}$ in (6.21), we recall that $n_q(t)$ is a wideband

AWGN process with bandwidth $W \gg 1/T_\omega \gg 1/T$ and hence

$$R_{n,q}(\tau) = 0; \quad |\tau| \geq T_\omega \tag{6.30}$$

can be reasonably assumed. The correlation of the noise terms found in (6.22 - 6.24), can generally be written as

$$\mathrm{E}\left\{ \begin{array}{l} n_{q'}\left(t + (k-1)NT + (v-1)T\right) \\ \times\ n_{q''}\left(t + kNT + (u-1)T\right) \end{array} \right\} = \left\{ \begin{array}{ll} 0; & q' \neq q'' \\ R_{n,q}\left(|N + u - v|\, T\right); & q' = q'' = q \end{array} \right. . \tag{6.31}$$

When $q' = q'' = q$, $1 \leq u \leq N$ and $1 \leq v \leq N$, the correlation lag $|N + u - v|\, T$ in (6.31) is lower bounded by T, which yields $R_{n,q}(|N + u - v|\, T) = 0$ according to (6.30). This implies that $n_q(t + (k-1)NT + (v-1)T)$ and $n_q(t + kNT + (u-1)T)$ are uncorrelated. Clearly, A_1 and A_2 are Gaussian random variables when conditioned on the set $\zeta = \{h_{pq}(t)\}$. A_3 can also be seen from the central limit theorem as approximately Gaussian distributed. With these observations, we simplify our noise analysis by treating A_1, A_2 and A_3, conditioned on ζ, as independent Gaussian random variables. The conditional mean and variance of $[\mathbf{N}_k]_{u,v}$ are, respectively, given by

$$\mathrm{E}\left\{ [\mathbf{N}_k]_{u,v} \middle| \zeta \right\} = 0 \tag{6.32}$$

and

$$\mathrm{Var}\left\{ [\mathbf{N}_k]_{u,v} \middle| \zeta \right\} = \mathrm{E}\left[A_1^2 \middle| \zeta\right] + \mathrm{E}\left[A_2^2 \middle| \zeta\right] + \mathrm{E}\left[A_3^2\right] \tag{6.33}$$

where $\mathrm{Var}[\cdot]$ denotes variance and $\mathrm{E}[\cdot]$ the expected value operator. Using (6.22),

the conditional variance of A_1 can be expressed as

$$\mathrm{E}\left[A_1^2\middle|\,\zeta\right] = \mathrm{E}\left[\begin{array}{l}\displaystyle\sum_{p'=1}^{P}\sum_{m'=1}^{M} d_{p',(k-1)N+v-m'}\sum_{q'=1}^{Q}\int_0^T h_{p'q',m'}\left(t'\right) n_{q'}\left(t'+kNT+\left(u-1\right)T\right)dt' \\ \displaystyle\sum_{p''=1}^{P}\sum_{m''=1}^{M} d_{p'',(k-1)N+v-m''}\sum_{q''=1}^{Q}\int_0^T h_{p''q'',m''}\left(t''\right) n_{q''}\left(t''+kNT+\left(u-1\right)T\right)dt''\end{array}\right]$$

$$= \sum_{p=1}^{P}\sum_{m=1}^{M}\left[\sum_{q=1}^{Q}\int_0^T\int_0^T h_{pq,m}\left(t'\right) h_{pq,m}\left(t''\right) R_{n,q}\left(t'-t''\right) dt'dt''\right] \tag{6.34}$$

because $\mathrm{E}\left[d_{p'',(k-1)N+v-m''}d_{p',(k-1)N+v-m'}\right] = \begin{cases} 0;\ p'\neq p'' \text{ or } m'\neq m'' \\ 1;\ p'=p'' \text{ and } m'=m'' \end{cases}$. In a similar manner, we can use (6.23) to show that

$$\mathrm{E}\left[A_2^2\middle|\,\zeta\right] = \mathrm{E}\left[A_1^2\middle|\,\zeta\right]. \tag{6.35}$$

As a second, and coarser, approximation, we let

$$R_{n,q}\left(\tau\right) \simeq \frac{N_o}{2}\delta\left(\tau\right), \tag{6.36}$$

on the basis that $R_{n,q}\left(\tau\right)$ appears almost impulse like for sufficiently large bandwidth-to-symbol rate ratio, WT. Applying (6.36) in (6.34), it is straightforward to show that

$$\mathrm{E}\left[A_1^2\middle|\,\zeta\right] = \mathrm{E}\left[A_2^2\middle|\,\zeta\right] \simeq \frac{N_o}{2}\sum_{p=1}^{P}\sum_{q=1}^{Q}\mathcal{E}_{pq} \tag{6.37}$$

where

$$\mathcal{E}_{pq} = \sum_{m=1}^{M}\mathcal{E}_{pq,m}. \tag{6.38}$$

For A_3 given in (6.24), which is independent of ζ, we have

$$\mathrm{E}\left[A_3^2\right] = \sum_{q=1}^{Q} \int_0^T \int_0^T \mathrm{E}\left[\begin{array}{l} n_q\left(t' + kNT + (u-1)\,T\right) n_q\left(t'' + kNT + (u-1)\,T\right) \times \\ n_q\left(t' + kNT + (v-1-N)\,T\right) n_q\left(t'' + kNT + (v-1-N)\,T\right) \end{array} \right] dt'dt''$$

$$= \sum_{q=1}^{Q} \int_0^T \int_0^T \left[\begin{array}{l} R_{n,q}^2\left(t' - t''\right) + R_{n,q}^2\left((u-v+N)\,T\right) + \\ R_{n,q}\left((u-v+N)\,T + t' - t''\right) R_{n,q}\left((u-v+N)\,T + t'' - t'\right) \end{array} \right] dt'dt''$$

$$= \sum_{q=1}^{Q} \int_0^T \int_0^T R_{n,q}^2\left(t' - t''\right) dt'dt'' \quad \cdots\cdots\cdots\cdots\cdots \quad \text{(after applying (6.30))}$$

$$\simeq \frac{QN_o^2WT}{2}. \tag{6.39}$$

Based on the approximate analysis above, the elements of $\mathbf{N}_k$ have identical conditional variances given by

$$\sigma_{N|\zeta}^2 = \mathrm{Var}\left\{ \left[\mathbf{N}_k\right]_{u,v} \middle| \, \zeta \right\} = N_o \sum_{p=1}^{P} \sum_{q=1}^{Q} \mathcal{E}_{pq} + \frac{QN_o^2WT}{2}. \tag{6.40}$$

6.2.1 Systems without ISI

When the symbol duration, T, is chosen to be sufficiently large so as to span the full memory length of the channel monocycle response, which results in $M = 1$ in (6.16), the transmission will not experience ISI. Under this condition, $\mathbf{S}_k$ in (6.28) becomes

$$\mathbf{S}_k = \mathbf{D}_k^{\dagger}\,\mathbf{H}_1\mathbf{D}_{k-1} = \mathbf{U}_k^{\dagger}\mathbf{D}_{k-1}^{\dagger}\mathbf{H}_1\mathbf{D}_{k-1}. \tag{6.41}$$

Each element $[\mathbf{R}_k]_{u,v}$ of the decision statistics $\mathbf{R}_k$ then has a conditional probability density function given by

$$f_{[\mathbf{R}_k]_{u,v}|\zeta}\left([\mathbf{R}_k]_{u,v}\right) = \frac{1}{\sqrt{2\pi\sigma^2_{N|\zeta}}} \exp\left(\frac{-\left([\mathbf{R}_k]_{u,v} - [\mathbf{S}_k]_{u,v}\right)^2}{2\sigma^2_{N|\zeta}}\right). \tag{6.42}$$

Suppose we form the set

$$\Phi_\xi = \mathrm{Tr}\left(\mathbf{U}^{(\xi)}\mathbf{R}_k\right);\ \xi = 1, 2, \cdots, N_\Omega \tag{6.43}$$

and let $\widehat{\mathbf{U}}_k$, as defined in (6.15), be the detected message block. The probability of correct detection for a given channel matrix when $\mathbf{U}^{(l)}$ is transmitted during the k^{th} transmission block is given by

$$\begin{aligned}\Pr\left(\widehat{\mathbf{U}}_k = \mathbf{U}^{(l)} \middle| \mathbf{U}^{(l)}, \zeta\right) &= \Pr\left(\max\left\{\Phi_1, \Phi_2, \cdots, \Phi_{N_\Omega}\right\} = \Phi_l\right) \\ &= \int_{-\infty}^{\infty} \left[\left.\frac{\partial F_{\Phi_1\Phi_2\cdots\Phi_{N_\Omega}}\left(\phi_1, \phi_2, \cdots, \phi_{N_\Omega}\right)}{\partial\phi_l}\right|_{\phi_k=\phi_l\ \forall k\neq l}\right] d\phi_l.\end{aligned} \tag{6.44}$$

where $F_\chi(\cdot)$ denotes the probability distribution function of χ. The corresponding average probability of correct detection is then computed by

$$\begin{aligned}\Pr\left(\widehat{\mathbf{U}}_k = \mathbf{U}^{(l)} \middle| \mathbf{U}^{(l)}\right) = \int_0^\infty \cdots \int_0^\infty &\Pr\left(\widehat{\mathbf{U}}_k = \mathbf{U}^{(l)} \middle| \mathbf{U}^{(l)}, \zeta\right) f_{\mathcal{E}_{11}}(\varepsilon_{11}) \\ &f_{\mathcal{E}_{12}}(\varepsilon_{12}) \cdots f_{\mathcal{E}_{PQ}}(\varepsilon_{PQ})\, d\varepsilon_{11} d\varepsilon_{12} \cdots d\varepsilon_{PQ}.\end{aligned} \tag{6.45}$$

For large P and Q values, the evaluation of (6.45) is non-trivial. However,

for the case of $P \leq 2$ and $Q \leq 2$, (6.45) can be used to efficiently predict the performance of the system.

6.3 Differential Space-Time Codes Design

Unlike those designed in [62], the codes in this thesis are subjected to an additional restriction, that is, all of the entries of $\mathbf{U}^{(l)}$, $l = 1, 2, \cdots, N_\Omega$, in code Ω belong to $\{-1, 0, 1\}$. Furthermore, the rank criterion [62, 68] of DSTC is no longer a design criterion. This is because $\mathbf{H}_1$ in the signal matrix $\mathbf{S}_k$ without ISI (6.41), is a diagonal matrix. Therefore, even repetition codes [68] can exploit full spatial diversity of the channel. In this section, we provide the DSTC design criteria for channels with and without ISI. We also introduce a class of maximum distance codes to be used with the proposed system for any number of transmit antennas.

6.3.1 Design Criteria

In general, the UWB channels have extremely long memory length. Hence, the avoidance of ISI is often impractical. From (6.15) and (6.25), we know that the code Ω must be designed to maximize $\mathrm{Tr}(\mathbf{U}_k\mathbf{S}_k)$. To simplify the derivation, we rewrite $\widetilde{\mathbf{D}}_{k,m}$ in (6.6) as follows

$$\widetilde{\mathbf{D}}_{k,m} = \left(\overrightarrow{\mathbf{D}}_{(k-1),m}, \overleftarrow{\mathbf{D}}_{k,(N-m)}\right) \tag{6.46}$$

where $\overrightarrow{\mathbf{D}}_{(k-1),m}$ denotes the last m columns of $\mathbf{D}_{k-1}$ and $\overleftarrow{\mathbf{D}}_{k,(N-m)}$ denotes the first $N-m$ columns of $\mathbf{D}_k$. We also rewrite $\mathbf{U}_k$ as follows

$$\mathbf{U}_k = \begin{pmatrix} \mathbf{V}_{1,m} & \mathbf{V}_{2,m} \\ \mathbf{V}_{3,m} & \mathbf{V}_{4,(N-m)} \end{pmatrix} \tag{6.47}$$

where $\mathbf{V}_{1,m}$ is an $m \times m$ matrix, $\mathbf{V}_{2,m}$ is an $m \times (N-m)$ matrix, $\mathbf{V}_{3,m}$ is an $(N-m) \times m$ matrix and $\mathbf{V}_{4,(N-m)}$ is an $(N-m) \times (N-m)$ matrix. Therefore, using $\mathbf{S}_k$ in (6.28), we have

$$\mathrm{Tr}\left(\mathbf{U}_k\mathbf{S}_k\right) = \mathrm{Tr}\left(\mathbf{U}_k\mathbf{D}_k^{\dagger}\mathbf{H}_1\mathbf{D}_{k-1}\right) + \sum_{m=1}^{M-1} \mathrm{Tr}\left(\mathbf{U}_k\widetilde{\mathbf{D}}_{k,m}^{\dagger}\mathbf{H}_{m+1}\widetilde{\mathbf{D}}_{k-1,m}\right) \tag{6.48}$$

where

$$\mathrm{Tr}\left(\mathbf{U}_k\mathbf{D}_k^{\dagger}\mathbf{H}_1\mathbf{D}_{k-1}\right) = \mathrm{Tr}\left(\mathbf{D}_{k-1}^{\dagger}\mathbf{H}_1\mathbf{D}_{k-1}\right) = N\mathrm{Tr}\left(\mathbf{H}_1\right) \tag{6.49}$$

and

$$\begin{aligned} &\mathrm{Tr}\left(\mathbf{U}_k\widetilde{\mathbf{D}}_{k,m}^{\dagger}\mathbf{H}_{m+1}\widetilde{\mathbf{D}}_{k-1,m}\right) = \mathrm{Tr}\left(\mathbf{V}_{1,m}\overrightarrow{\mathbf{D}}_{(k-1),m}^{\dagger}\mathbf{H}_{m+1}\overrightarrow{\mathbf{D}}_{(k-2),m}\right) \\ +\ &\mathrm{Tr}\left(\mathbf{V}_{2,m}\overleftarrow{\mathbf{D}}_{k,(N-m)}^{\dagger}\mathbf{H}_{m+1}\overrightarrow{\mathbf{D}}_{(k-2),m}\right) + \mathrm{Tr}\left(\mathbf{V}_{3,m}\overrightarrow{\mathbf{D}}_{(k-1),m}^{\dagger}\mathbf{H}_{m+1}\overleftarrow{\mathbf{D}}_{(k-1),(N-m)}\right) \\ +\ &\mathrm{Tr}\left(\mathbf{V}_{4,(N-m)}\overleftarrow{\mathbf{D}}_{k,(N-m)}^{\dagger}\mathbf{H}_{m+1}\overleftarrow{\mathbf{D}}_{(k-1),(N-m)}\right). \end{aligned} \tag{6.50}$$

Using the relationship $\mathbf{D}_k = \mathbf{D}_{k-1}\mathbf{U}_k$, and (6.46) and (6.47), the last term in (6.50) can be further decomposed into

$$\begin{aligned}
&\mathrm{Tr}\left(\mathbf{V}_{4,(N-m)}\overleftarrow{\mathbf{D}}^{\dagger}_{k,(N-m)}\mathbf{H}_{m+1}\overleftarrow{\mathbf{D}}_{(k-1),(N-m)}\right)\\
=\ &\mathrm{Tr}\left(\mathbf{V}_{4,(N-m)}\left(\overleftarrow{\mathbf{D}}_{(k-1),(N-m)}\mathbf{V}_{1,(N-m)}+\overrightarrow{\mathbf{D}}_{(k-1),m}\mathbf{V}_{3,(N-m)}\right)^{\dagger}\mathbf{H}_{m+1}\overleftarrow{\mathbf{D}}_{(k-1),(N-m)}\right)\\
=\ &\mathrm{Tr}\left(\mathbf{V}_{4,(N-m)}\mathbf{V}^{\dagger}_{1,(N-m)}\overleftarrow{\mathbf{D}}^{\dagger}_{(k-1),(N-m)}\mathbf{H}_{m+1}\overleftarrow{\mathbf{D}}_{(k-1),(N-m)}\right)\\
+\ &\mathrm{Tr}\left(\mathbf{V}_{4,(N-m)}\mathbf{V}^{\dagger}_{3,(N-m)}\overrightarrow{\mathbf{D}}^{\dagger}_{(k-1),m}\mathbf{H}_{m+1}\overleftarrow{\mathbf{D}}_{(k-1),(N-m)}\right). \qquad (6.51)
\end{aligned}$$

Note that in the first term of (6.51),

$$\begin{aligned}
&\mathrm{Tr}\left(\overleftarrow{\mathbf{D}}^{\dagger}_{(k-1),(N-m)}\mathbf{H}_{m+1}\overleftarrow{\mathbf{D}}_{(k-1),(N-m)}\right)\\
&=(N-m)\mathrm{Tr}\left(\mathbf{H}_{m+1}\right)\geq\mathrm{Tr}\left(\widetilde{\mathbf{V}}\overleftarrow{\mathbf{D}}^{\dagger}_{(k-1),(N-m)}\mathbf{H}_{m+1}\overleftarrow{\mathbf{D}}_{(k-1),(N-m)}\right)
\end{aligned} \qquad (6.52)$$

where $\widetilde{\mathbf{V}}$ is any orthogonal message matrix with elements belonging to the set $\{-1,0,1\}$. Therefore, if we can find a code which satisfies the following property,

$$\mathbf{V}_{4,(N-m)} = \mathbf{V}_{1,(N-m)}, \qquad (6.53)$$

we can maximize $\mathrm{Tr}\left(\mathbf{V}_{4,(N-m)}\mathbf{V}^{\dagger}_{1,(N-m)}\overleftarrow{\mathbf{D}}^{\dagger}_{(k-1),(N-m)}\mathbf{H}_{m+1}\overleftarrow{\mathbf{D}}_{(k-1),(N-m)}\right)$, which in turn maximizes $\mathrm{Tr}(\mathbf{U}_k\mathbf{S}_k)$. In doing so, we improve the decision statistic. For (6.53) to hold, $\mathbf{U}_k$ should be a Toeplitz matrix.

Next, we consider the situation when there is no ISI. Without ISI, the decision

statistics $\mathbf{R}_k$ in (6.25) simplifies to

$$\mathbf{R}_k = \mathbf{U}_k^{\dagger}\mathbf{D}_{k-1}^{\dagger}\mathbf{H}_1\mathbf{D}_{k-1} + \mathbf{N}_k. \tag{6.54}$$

Suppose two equally likely information symbols $\mathbf{U}$ and $\mathbf{U}'$ are transmitted. The probability of decoding error is then given by

$$\begin{aligned} \Pr(\mathbf{U} \to \mathbf{U}') &= \Pr\left(\mathrm{Tr}\left\{(\mathbf{U}-\mathbf{U}')\mathbf{R}_k\right\} < 0 | \mathbf{U}\right) \\ &= \Pr\left(\mathrm{Tr}\left\{(\mathbf{U}-\mathbf{U}')\left(\mathbf{U}^{\dagger}\mathbf{D}_{k-1}^{\dagger}\mathbf{H}_1\mathbf{D}_{k-1} + \mathbf{N}_k\right)\right\} < 0\right). \end{aligned} \tag{6.55}$$

Since

$$\Pr(\mathbf{U} \to \mathbf{U}') = \Pr(\mathbf{U}' \to \mathbf{U}), \tag{6.56}$$

we have

$$\min \Pr(\mathbf{U} \to \mathbf{U}') \equiv \max \mathrm{Tr}\left\{(\mathbf{U}-\mathbf{U}')(\mathbf{U}-\mathbf{U}')^{\dagger}\right\}. \tag{6.57}$$

Based on (6.57), we define the minimum code distance of the code Ω, which is used as a design criterion.

Definition 4.1: Let $\mathbf{U}$ and $\mathbf{U}'$ be the codewords of Ω, the code distance $\Lambda(\mathbf{U}, \mathbf{U}')$ of $\mathbf{U}$ and $\mathbf{U}'$ is defined as

$$\Lambda(\mathbf{U}, \mathbf{U}') = \mathrm{Tr}\left\{(\mathbf{U}-\mathbf{U}')(\mathbf{U}-\mathbf{U}')^{\dagger}\right\}. \tag{6.58}$$

The minimum code distance Λ of Ω is defined as

$$\Lambda = \min_{\mathbf{U} \neq \mathbf{U}' \in \Omega} \mathrm{Tr}\left\{(\mathbf{U}-\mathbf{U}')(\mathbf{U}-\mathbf{U}')^{\dagger}\right\}. \tag{6.59}$$

6.3.2 Design of Maximum Distance Codes

In this subsection, the Toeplitz matrix criterion and code distance criterion derived in previous subsection are used to design maximum distance codes based on group structure (cf. Appendix C.1). If a code Ω has the minimum code distance of $2N$, we call such code as a maximum distance code.

To generate the maximum distance code Ω, we only need to find a generator matrix $\mathbf{U}$ that contains $e^{i\pi/N}$ as one of its eigenvalues. If the generator $\mathbf{U}$ is found, the maximum distance code Ω can be constructed as

$$\Omega = \{\mathbf{U}^n, n = 1, 2, \cdots, 2N\}. \tag{6.60}$$

To show that codes found by using the method above are maximum distance codes, we only need to prove that Ω is a group and all the codewords in Ω have zero trace (cf. Appendix C.1). Because the trace of a square matrix is equal to the sum of all the eigenvalues [88], we study the properties of eigenvalues of $\mathbf{U}$ in Appendix C.2. We know that $\mathbf{U}$ is an orthogonal matrix whose eigenvalues have unit magnitude and can be written as $e^{i\theta}, \theta \in (0, 2\pi]$. If the eigenvalues of the generator $\mathbf{U}$ are denoted as $\{e^{i\theta_1}, e^{i\theta_2}, \cdots, e^{i\theta_N}\}$, the eigenvalues of $\mathbf{U}^n$ are $\{e^{in\theta_1}, e^{in\theta_2}, \cdots, e^{in\theta_N}\}$ [88]. Therefore, to find a maximum distance code Ω from the group structure is equivalent to finding the generator $\mathbf{U}$ whose eigenvalues satisfies

$$\theta_1 + \theta_2 + \cdots + \theta_N = 2k\pi \tag{6.61}$$

where k is an integer. *Theorems* C.2 - C.5 in Appendix C.2 prove the existence of such $\mathbf{U}$ and *Theorem* C.6 proves that Ω is a group.

To improve the decision statistic, all the elements in Ω should be Toeplitz matrices, which is true when the generator is a Toeplitz matrix (cf. Appendix C.3).

6.4 Simulation Results

In this section, we provide computer simulated system bit-error-rate (BER) results to demonstrate the performance of the DSTC MIMO d^2TD-IR system based on our design and analysis. In all cases, the random channels are generated according to [44]. The channel model used in the simulations, if not specified, is the CM 2, $0 \sim 4$ meters' range non-line-of-sight (NLOS) model. The sampling interval is chosen to be 0.167 ns as in [44]. The bandwidth of the lowpass filter is 2.994 GHz. As in [8], we select the shape of the monocycle $\omega(t)$ to be the second derivative of Gaussian function, namely, $[1 - 4\pi(t/\tau_m)^2]\exp[-2\pi(t/\tau_m)^2]$, where $\tau_m = 0.2877$ ns.

6.4.1 UWB Channel without ISI

Here, the symbol duration T is set to 50.10 ns. The tail of the multipath channel power profile whose delay exceeds $T - T_\omega$ is removed. Therefore, the proposed system works in the UWB channel without ISI. As in [44], the energy of the channel response of $\omega(t)$ is characterized by

$$\mathcal{E}_{pq} = 10^{X/10} \cdot \int_0^{T_\omega} \omega^2(t)dt \tag{6.62}$$

where X is a Gaussian random variable with zero mean and variance 9.

In Fig. 6.3, we compare the BER performance of the single user SISO d^2TD-IR (denoted as "d2TD-IR(S)" in the legend) with that of the proposed single user DSTC MIMO d^2TD-IR system (denoted as "DSTC-d2TD-IR(S)" in the legend) for $P = N \leq 2$ and $Q \leq 2$. In particular, the code Ω used for $P = N = 2$ in our simulations is

$$\begin{aligned} \mathbf{U}^{(1)} &= \begin{pmatrix} 1 & 0 \\ 0 & 1 \end{pmatrix} \quad \mathbf{U}^{(2)} = \begin{pmatrix} 0 & 1 \\ -1 & 0 \end{pmatrix} \\ \mathbf{U}^{(3)} &= \begin{pmatrix} -1 & 0 \\ 0 & -1 \end{pmatrix} \quad \mathbf{U}^{(4)} = \begin{pmatrix} 0 & -1 \\ 1 & 0 \end{pmatrix}. \end{aligned} \tag{6.63}$$

The binary information bits are encoded and decoded by Gray codes, i.e., "00" as $\mathrm{U}^{(1)}$; "01" as $\mathbf{U}^{(2)}$; "11" as $\mathbf{U}^{(3)}$ and "10" as $\mathbf{U}^{(4)}$. Suppose that $\mathbf{U}^{(1)}$ is transmitted, $\mathbf{S}_k$ in (6.41) can be expressed as

$$\mathbf{S}_k = \begin{pmatrix} \mathcal{E}_{11} + \mathcal{E}_{12} + \mathcal{E}_{21} + \mathcal{E}_{22} & \pm\mathcal{E}_{11} \pm \mathcal{E}_{12} \mp \mathcal{E}_{21} \mp \mathcal{E}_{22} \\ \pm\mathcal{E}_{11} \pm \mathcal{E}_{12} \mp \mathcal{E}_{21} \mp \mathcal{E}_{22} & \mathcal{E}_{11} + \mathcal{E}_{12} + \mathcal{E}_{21} + \mathcal{E}_{22} \end{pmatrix}. \tag{6.64}$$

From (6.43) and (6.63), we have

$$\Phi_1 = -\Phi_3 \text{ and } \Phi_2 = -\Phi_4. \tag{6.65}$$

Therefore, the probability of $\mathbf{U}^{(1)}$ detected as $\mathbf{U}^{(3)}$ is

$$\begin{aligned} \Pr\left(\widehat{\mathbf{U}}_k = \mathbf{U}^{(3)} \left| \mathbf{U}^{(1)}, \zeta \right.\right) &= \Pr\left(\max\left\{\Phi_1, \Phi_2, \Phi_2, \Phi_4\right\} = \Phi_3\right) \\ &= \Pr\left(\Phi_1 < -|\Phi_2| < 0\right). \end{aligned} \tag{6.66}$$

Consequently, we have

$$\Pr\Big(\widehat{\mathbf{U}}_k=\mathbf{U}^{(3)}\,\Big|\mathbf{U}^{(1)}\Big)=\int_0^\infty\int_0^\infty\int_0^\infty\int_0^\infty\int_{-\infty}^0\frac{1}{\sqrt{4\pi\sigma_{N|\zeta}^2}}\exp\left(\frac{-(\phi-2(\varepsilon_{11}+\varepsilon_{12}+\varepsilon_{21}+\varepsilon_{22}))^2}{4\sigma_{N|\zeta}^2}\right)$$
$$\left(1-2\Upsilon\left(\frac{|\phi|}{\sqrt{2\sigma_{N|\zeta}^2}}\right)\right)f_{\mathcal{E}_{11}}(\varepsilon_{11})f_{\mathcal{E}_{12}}(\varepsilon_{12})f_{\mathcal{E}_{21}}(\varepsilon_{21})f_{\mathcal{E}_{22}}(\varepsilon_{22})d\phi d\varepsilon_{11}d\varepsilon_{12}d\varepsilon_{21}d\varepsilon_{22} \quad (6.67)$$

where $\Upsilon(z)=\left(1/\sqrt{2\pi}\right)\int_z^\infty\exp(-y^2/2)dy$. By letting

$$\mathcal{E}=\mathcal{E}_{11}+\mathcal{E}_{12}+\mathcal{E}_{21}+\mathcal{E}_{22} \quad (6.68)$$

and

$$f_{\mathcal{E}}(\varepsilon)=f_{\mathcal{E}_{11}}(\varepsilon_{11})\otimes f_{\mathcal{E}_{12}}(\varepsilon_{12})\otimes f_{\mathcal{E}_{21}}(\varepsilon_{21})\otimes f_{\mathcal{E}_{22}}(\varepsilon_{22}), \quad (6.69)$$

(6.67) can be further simplified to

$$\begin{aligned}\Pr\left(\widehat{\mathbf{U}}_k=\mathbf{U}^{(3)}\,\middle|\mathbf{U}^{(1)}\right)=&\int_0^\infty\int_{-\infty}^0\frac{1}{\sqrt{4\pi\sigma_{N|\zeta}^2}}\exp\left(\frac{-(\phi-2\varepsilon)^2}{4\sigma_{N|\zeta}^2}\right)\\&\left(1-2\Upsilon\left(\frac{|\phi|}{\sqrt{2\sigma_{N|\zeta}^2}}\right)\right)f_{\mathcal{E}}(\varepsilon)d\phi d\varepsilon.\end{aligned} \quad (6.70)$$

Using the same method, we can compute the probability of erroneously detecting $\mathbf{U}^{(1)}$ as $\mathbf{U}^{(2)}$ or $\mathbf{U}^{(4)}$ as follows

$$\begin{aligned}&\Pr\left(\widehat{\mathbf{U}}_k=\mathbf{U}^{(2)}\,\middle|\mathbf{U}^{(1)}\right)=\Pr\left(\widehat{\mathbf{U}}_k=\mathbf{U}^{(4)}\,\middle|\mathbf{U}^{(1)}\right)\\&=\int_0^\infty\int_{-\infty}^\infty\frac{1}{\sqrt{4\pi\sigma_{N|\zeta}^2}}\exp\left(\frac{-(\phi-2\varepsilon)^2}{4\sigma_{N|\zeta}^2}\right)\Upsilon\left(\frac{|\phi|}{\sqrt{2\sigma_{N|\zeta}^2}}\right)f_{\mathcal{E}}(\varepsilon)d\phi d\varepsilon.\end{aligned} \quad (6.71)$$

Because of the symmetrical property of the code Ω, the system BER is given by

$$\Pr(e) = \Pr\left(\widehat{\mathbf{U}}_k = \mathbf{U}^{(3)} \left| \mathbf{U}^{(1)} \right.\right) + \Pr\left(\widehat{\mathbf{U}}_k = \mathbf{U}^{(2)} \left| \mathbf{U}^{(1)} \right.\right). \tag{6.72}$$

Fig. 6.3 shows that the proposed system where $P = Q = N = 2$ achieves a performance improvement of about $5 \sim 7$ dB over the SISO system. The theoretical results obtained using (6.72) match the simulation results. In Fig. 6.3, we also show the simulation results of the single user differential repetition coded (DRC) [68] MIMO d^{2}TD-IR system, which is denoted as "DRC-d2TD-IR(S)" in the legend. The system transmits 1×1 matrices $\mathbf{U}_k$ with binary values $\{-1, 1\}$. The message matrix $\mathbf{U}_k$ is differentially encoded using (6.2), where $\mathbf{D}_0$ is $P \times 1$ matrix with all 1 entries. We compare the BER performances of the $P = 2$ DRC system and the $P = N = 2$ DSTC system in Fig. 6.3. At the same transmission rate, Fig. 6.3 shows that their BER performances are also the same. This is because in the equivalent system model without ISI (6.54), the matrix $\mathbf{H}_1$ is diagonal matrix. Even DRC can explore the full diversity of the MIMO UWB channel. Furthermore, the code distances of these two codes are the same.

6.4.2 UWB Channel with ISI

Here, the MIMO UWB channels are generated without the modification applied in the previous subsection. In Fig. 6.4 and Fig. 6.5, we compare the BER performance of the single user SISO d^{2}TD-IR system with that of the proposed single user DSTC MIMO d^{2}TD-IR system for $P = N \leq 2$ and $Q \leq 2$ in CM 2 and CM 3 ($4 \sim 10$ meters' range NLOS model) UWB channels. The symbol duration T is set to 20.04 ns and 40.08 ns, respectively. Fig. 6.4 and Fig. 6.5 show that the

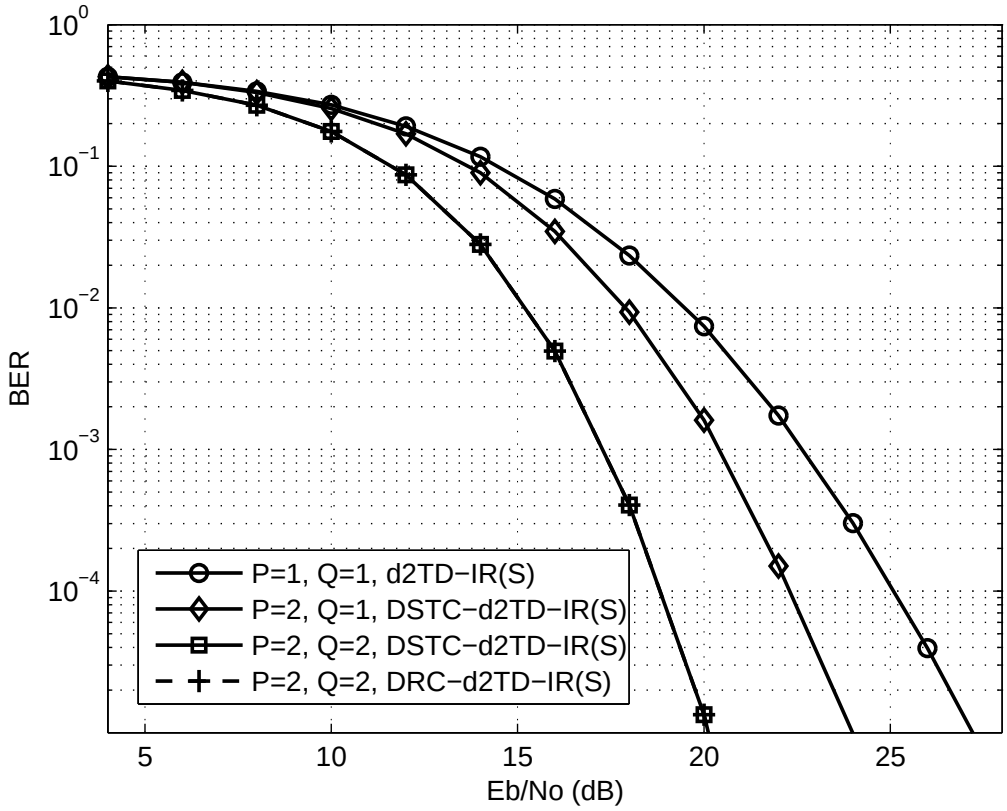

Fig. 6.3: BER performance comparison of single user DSTC MIMO, DRC MIMO and SISO d^2TD-IR systems in CM 2 UWB channels without ISI.

proposed system where $P = Q = N = 2$ achieves a performance improvement of about $3 \sim 5$ dB over the SISO system. In Fig. 6.4 and Fig. 6.5, we also compare the BER performances of the DRC system and the DSTC system. Fig. 6.4 shows that the latter has about 1.0 dB signal-to-noise-ratio (SNR) advantage over the former when the BER is 1×10^{-3} and Fig. 6.5 shows about 1.9 dB SNR advantage when the BER is 3×10^{-2}, respectively.

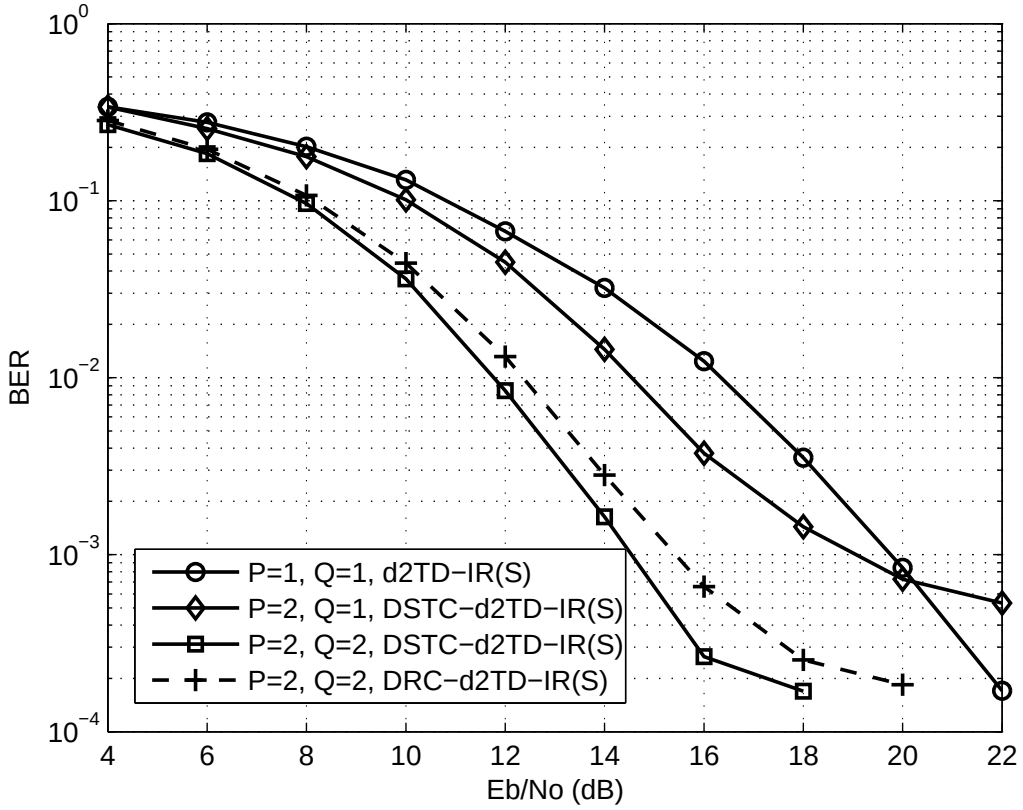

Fig. 6.4: BER performance comparison of single user DSTC MIMO, DRC MIMO and SISO d^2TD-IR systems in CM 2 UWB channels with ISI.

6.4.3 Implement of DSTC on the d^{2}TD-IR System

In the discussion above, we consider the proposed DSTC MIMO d^{2}TD-IR in single user scenario. The DSTC MIMO scheme can be extended to the multiuser system with slight modifications.

In Fig. 6.6, we present the simulation results for BER performance comparison of the multiuser SISO d^{2}TD-IR system (denoted as "d2TD-IR(M)" in the legend) and the proposed multiuser MIMO d^{2}TD-IR system (denoted as "DSTC-d2TD-IR(M)" in the legend) for $P = N \leq 2$ and $Q \leq 2$ in CM 2 UWB channel. The

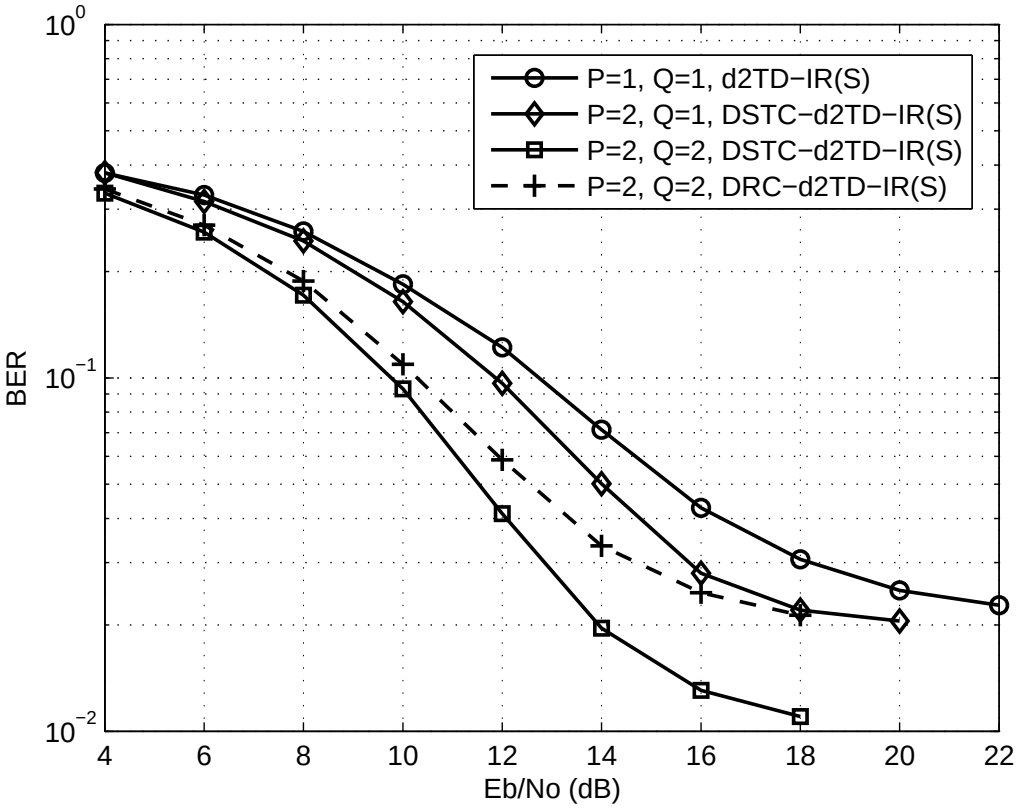

Fig. 6.5: BER performance comparison of single user DSTC MIMO, DRC MIMO and SISO d^2TD-IR systems in CM 3 UWB channels with ISI.

d^2TD-IR system parameters are $T_c = 20.04$ ns, $N_s = 2$ and $N_u = 10$. From Fig. 6.6, it is observed that at BER of 1×10^{-3}, the $P = Q = N = 2$ MIMO d^2TD-IR system outperform the SISO system by about 6 dB. The BER performance of the DRC MIMO d^2TD-IR system (denoted as "DRC-d2TD-IR(M)" in the legend) is also presented. It is found that both DRC system and DSTC system have almost the same performance. This is because that in multiuser systems, the interference can not be exploited to improve the decision statistics.

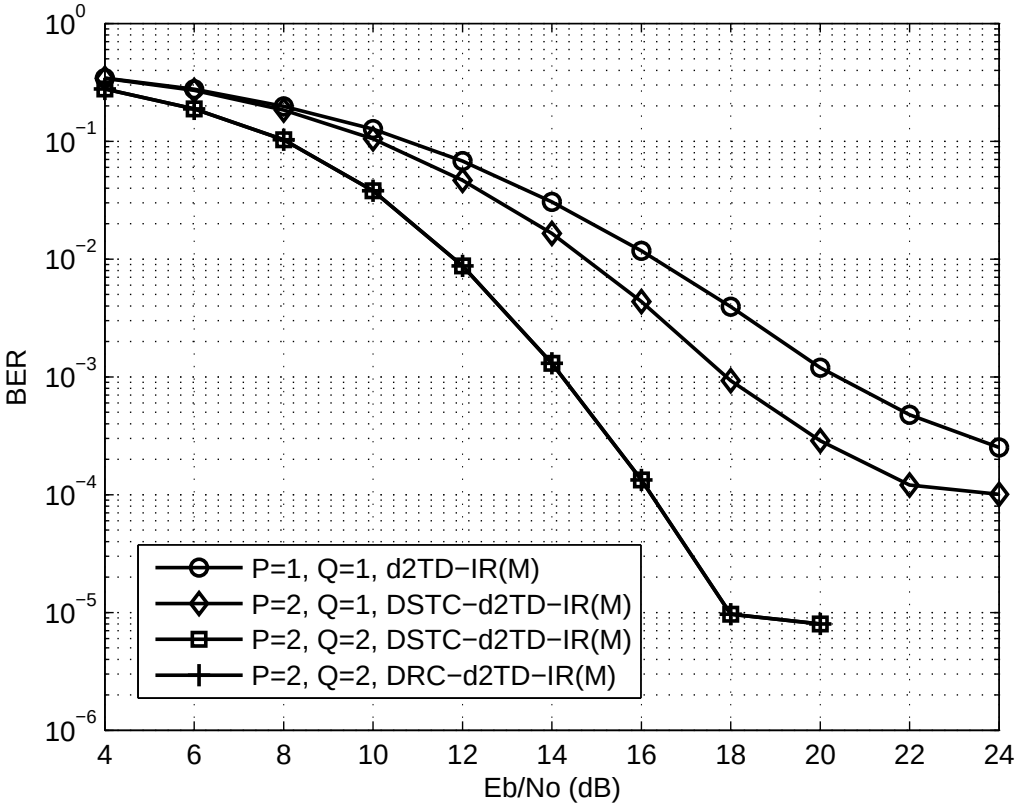

Fig. 6.6: BER performance comparison of multiuser DSTC MIMO, DRC MIMO and SISO d^2TD-IR systems in CM 2 UWB channels with ISI.

6.5 Summary

In this chapter, we proposed a DSTC MIMO d^2TD-IR system, which is capable of exploiting both multipath diversity and spatial diversity.

In a peer-to-peer transmission scenario, an equivalent system model was developed to study the proposed system. When there is no intersymbol interference (ISI), we derived the system bit-error-rate (BER) performance. We also discussed the design criteria of the DSTC for the proposed system for the channel with and without ISI. Such criteria were used to design the so called maximum distance

codes. Computer simulation results were provided to validate our analysis and designs.

In a multiuser transmission scenario, we provided simulation results to show the advantages of the proposed MIMO d^2TD-IR systems over the SISO systems.

Chapter 7

Conclusions and Proposals for Future Work

7.1 Conclusions

In this thesis, we proposed a differentially-encoded di-symbol time-division multiuser impulse radio (d^2TD-IR) system. Synchronization and power control methods had also been proposed to improve the robustness and performance of the system. To achieve low BER at relatively low SNR, we studied the effects of LDPC codes and LDPC product codes on the d^2TD-IR system. The SISO d^2TD-IR was then extended to MIMO d^2TD-IR to evaluate the effectiveness of diversity signaling in combating fading due to the UWB channels.

Through computer simulations and theoretical analysis, we have demonstrated that when the transmission rates are the same, the proposed d^2TD-IR system outperforms the conventional TH-IR system employing Rake reception at high E_b/N_o. This is attributable to the application of a hybrid of time-division (TD) and time-

hopping (TH) multiple access scheme and a delay-sum AcR, which maximally suppress the MUI and channel noise. Furthermore, when compared with the TH-IR system, the proposed system was shown to be more robust to timing synchronization error.

In our proposed d^{2}TD-IR system, the chip duration is not required to be longer than the maximum excess delay of the UWB channels. To properly choose the chip duration for a given scenario, we proposed a method that uses only average power decay profile of the UWB channel to estimate the chip duration which maximizes $\mathrm{E}_{\xi,\,\zeta}\left[\sqrt{\mathrm{SINR}_{\xi,\,\zeta}}\right]$. The estimation method works well, especially when 5 dB$<$ $E_b/N_o < 30$ dB.

Computer simulations also showed that our proposed synchronization algorithm for the d^{2}TD-IR system is efficient. When the algorithm stops at the time when the uncertainty region reduces to a quarter of the chip duration, BER performance of the d^{2}TD-IR system gets very close to that under perfect conditions. Compared with the conventional synchronization algorithms for the coherent TH-IR system, which use serial search or fixed-step serial search [22], the proposed synchronization algorithm, which gradually narrows down the uncertainty regions, is much simpler.

The proposed recursive algorithm which combines synchronization and power control effectively prevents error propagation, which means synchronization errors cause larger power control errors and power control errors cause larger synchronization errors. The accuracy of the recursive algorithm can be observed in the simulation results, which showed that after the combined synchronization and power control process, the system can achieve the BER as low as about 3×10^{-6} (very close to the perfect situation).

It was also found that the LDPC coded and LDPC product coded d^{2}TD-IR systems have about 3 dB coding gain over the uncoded system at the BER of 3×10^{-6}. The performance gain is not as significant as that of LDPC coded and LDPC product coded narrowband systems in AWGN channels. This is due to the fact that UWB channels are very slowly fading, close to static, channels with extremely long coherence time. When the transmitted signal undergoes deep fade, the proposed system requires relatively high SNR at the receiver to guarantee low BER.

When the SISO d^{2}TD-IR system was extended to a MIMO system, we found through computer simulations that the systems employing 2 transmit and 2 receive antennas have significant performance gain over the SISO systems. For simplicity, the proposed MIMO d^{2}TD-IR system was studied in a peer-to-peer transmission scenario with a spreading factor of one. It was observed that when there is no ISI, the theoretically derived system BER performance matches the simulation results. The design criteria of the DSTC for the proposed system were also derived. It was shown that with ISI, the DSTC with Toeplitz structure has better performance. Without ISI, the code distance is the only design criterion, with which we used to design a class of maximum distance codes for any number of the transmit antennas.

7.2 Proposals for Future Work

For simplicity, the synchronization algorithms proposed in Chapter 4 are pilot-assisted algorithms. However, it is a waste of channel capacity to transmit hundreds of pilot symbols. After the coarse synchronization has been achieved, we may transmit the LDPC coded information symbols instead of pilot symbols during the

following steps of synchronization. At the delay-sum AcR, we first apply the LDPC decoding scheme to decode the received symbols based on the decision statistics of each symbol. If the SNR at the receiver is sufficiently high, the received symbols can be correctly decoded. These decoded symbols are then used as pilot symbols for synchronization. Future study may be carried out on the design and performance of decision-direct synchronization algorithms with the help of LDPC codes for the proposed d^2TD-IR system.

In our proposed DSTC MIMO d^2TD-IR, we assumed that UWB channels from different transmit and receive antennas are independent. However, the UWB channels may be correlated with one another when the transmit antennas or receive antennas are close to one another. In [89], a correlation based double directional stochastic model for MIMO UWB propagation channels was proposed. The channel model is capable of describing the correlation between MIMO UWB channel based on the distance between different transmit and receive antennas. It would be interesting to examine how much performance gain the MIMO system can achieve over the SISO system when the transmit and receive antenna arrays can not be spaced more than the coherent distance.

Impulse radio systems are expected to co-exist with other narrowband systems over the same frequency band. When the power of narrowband interference is very high, some form of interference suppression is necessary. In [90], Bergel proposed an minimum mean-square error (MMSE) Rake receiver to suppress narrowband interference. Since channel estimation and Rake receiver are required in the scheme, it is not applicable to our proposed d^2TD-IR system. In [91], Baccarelli proposed a scheme which estimates the frequency, amplitude and phase of the narrowband interference, generates the interference signal locally and subtracts

it from the received signal. However, the scheme will significantly increase the system complexity. In the d^{2}TD-IR receiver block diagram Fig. 3.2, the multiple access code sequence $\left\{a_{0,0}^{(k)}, a_{1,0}^{(k)}, a_{0,1}^{(k)}, a_{1,1}^{(k)}, \cdots, a_{0,N_s-1}^{(k)}, a_{1,N_s-1}^{(k)}\right\}$ has unit magnitude. We may relax the constraint and find a set of $a_{i \bmod 2,j}^{(k)}$'s such that the receiver structure in Fig. 3.2 implements a bandstop filter with stopband centered about the interfere frequency band. Further research is needed to study how this can be done.

Appendix A

Estimation of the Optimal T_c for d^{2}TD-IR Systems

A.1 Computation of $\mathbf{E}[\mathcal{E}_m]$, $\mathbf{E}\left[\sigma_{1m}^2\right]$ and $\mathbf{E}\left[\mathcal{E}_m^2\right]$

Computation of $\mathbf{E}[\mathcal{E}_m]$

First we consider $\mathrm{E}[\mathcal{E}_m]$, which can be expressed as

$$\mathrm{E}[\mathcal{E}_m] = \mathrm{E}\left[\int_0^{T_c} h_m^2(t)dt\right] = \mathrm{E}\left[\int_0^{T_c} \left(g_m(t) \otimes \omega(t)\right)^2 dt\right]. \tag{A.1}$$

In (A.1), the definition of $g_m(t)$ is similar to that of $h_m^{(k)}(t)$ in (5.10),

$$g_m(t) = \sum_{l=L_{m-1}+1}^{L_m} \alpha_l \delta(t - \tau_l + (m-1)T_c) \tag{A.2}$$

where L_m denotes the number of propagation paths arriving within the duration of mT. Expanding (A.1), we have

$$\mathrm{E}\left[\mathcal{E}_m\right] = \mathrm{E}\left[\int_0^{T_c}\int_0^{T_\omega}\int_0^{T_\omega} g_m(t-\tau_1)g_m(t-\tau_2)\omega(\tau_1)\omega(\tau_2)d\tau_1 d\tau_2 dt\right]. \tag{A.3}$$

Since $g_m(t_1)$ and $g_m(t_2)$ are independent for $t_1 \neq t_2$,

$$\mathrm{E}\left[\mathcal{E}_m\right] = \int_0^{T_c}\int_0^{T_\omega} \mathrm{E}\left[\left(g_m(t-\tau)\right)^2\right]\omega^2(\tau)d\tau dt = \int_{(m-1)T_c}^{mT_c}\int_0^{T_\omega} G(t-\tau)\omega^2(\tau)d\tau dt. \tag{A.4}$$

Because of $T_\omega \ll T_c$ and considering $G(t)$ varies slowly with the increase of t when $t \geq T_c - T_\omega$, we approximate $G(t-\tau)$ using $G(t)$. Therefore,

$$\mathrm{E}\left[\mathcal{E}_m\right] = \mathcal{E}_\omega \int_{(m-1)T_c}^{mT_c} G(t)dt \tag{A.5}$$

where $\mathcal{E}_\omega := \int_0^{T_\omega}\omega^2(t)dt$ captures the energy of $\omega(t)$.

Computation of $\mathbf{E}\left[\sigma_{1m}^2\right]$

Next we consider $\mathrm{E}\left[\sigma_{1m}^2\right]$, which can be expressed as

$$\mathrm{E}\left[\sigma_{1m}^2\right] = \mathrm{E}\left[\int_0^{T_c}\int_0^{T_c} h_1(t_1)h_m(t_1)h_1(t_2)h_m(t_2)dt_1 dt_2\right]. \tag{A.6}$$

Replacing $h_m(t)$ with $\int_0^{T_\omega} g_m(t-\tau)\omega(\tau)d\tau$, we have

$$\mathrm{E}\left[\sigma_{1m}^2\right] = \mathrm{E}\left[\int_0^{T_c}\int_0^{T_c}\int_0^{T_\omega}\int_0^{T_\omega}\int_0^{T_\omega}\int_0^{T_\omega} H(\tau_1,\tau_2,\tau_3,\tau_4,t_1,t_2)d\tau_1 d\tau_2 d\tau_3 d\tau_4 dt_1 dt_2\right] \tag{A.7}$$

where

$$H(\tau_1, \tau_2, \tau_3, \tau_4, t_1, t_2) = g_1(t_1-\tau_1)g_m(t_1-\tau_2)g_1(t_2-\tau_3)g_m(t_2-\tau_4)\omega(\tau_1)\omega(\tau_2)\omega(\tau_3)\omega(\tau_4). \tag{A.8}$$

Since $g_m(t_1)$ and $g_m(t_2)$ are independent for $t_1 \neq t_2$,

$$\mathrm{E}\left[H(\tau_1, \tau_2, \tau_3, \tau_4, t_1, t_2)\right] = \mathrm{E}\left[g_1^2(t_1-\tau_1)g_m^2(t_1-\tau_2)\right]\delta(t_1-\tau_1-t_2+\tau_3)$$
$$\delta(t_1-\tau_2-t_2+\tau_4)\omega(\tau_1)\omega(\tau_2)\omega(t_2-t_1+\tau_1)\omega(t_2-t_1+\tau_2). \tag{A.9}$$

Because $g_1(t)$ and $g_m(t)$ are from different realizations of the channel model, $g_1^2(t_1-\tau_1)$ and $g_m^2(t_1-\tau_2)$ are independent. Therefore,

$$\mathrm{E}\left[H(\tau_1, \tau_2, \tau_3, \tau_4, t_1, t_2)\right] = G(t_1-\tau_1)G(t_1-\tau_2+(m-1)T_c)\delta(t_1-\tau_1-t_2+\tau_3)$$
$$\delta(t_1-\tau_2-t_2+\tau_4)\omega(\tau_1)\omega(\tau_2)\omega(t_2-t_1+\tau_1)\omega(t_2-t_1+\tau_2). \tag{A.10}$$

Integrating $\mathrm{E}[H(\tau_1, \tau_2, \tau_3, \tau_4, t_1, t_2)]$ with respect to τ_3 and τ_4, we have

$$\int_0^{T_\omega}\int_0^{T_\omega} \mathrm{E}\left[H(\tau_1, \tau_2, \tau_3, \tau_4, t_1, t_2)\right]d\tau_3 d\tau_4 = G(t_1-\tau_1)G(t_1-\tau_2+(m-1)T_c)$$
$$\omega(\tau_1)\omega(\tau_2)\omega(t_2-t_1+\tau_1)\omega(t_2-t_1+\tau_2). \tag{A.11}$$

As in the computation of $\mathrm{E}\left[\mathcal{E}_m\right]$, we use $G(t_1)$ and $G(t_1+(m-1)T_c)$ to approximate

$G(t_1 - \tau_1)$ and $G(t_1 - \tau_2 + (m-1)T_c)$, respectively. Therefore,

$$\begin{aligned} \mathrm{E}\left[\sigma_{1m}^2\right] &= \int_0^{T_c}\int_0^{T_c} G(t_1)G(t_1+(m-1)T_c)\int_0^{T_\omega}\omega(\tau_1)\omega(t_2-t_1+\tau_1)d\tau_1 \\ &\quad \int_0^{T_\omega}\omega(\tau_2)\omega(t_2-t_1+\tau_2)d\tau_2 dt_1 dt_2. \end{aligned} \tag{A.12}$$

Let $\varphi(t) = \int_0^{T_\omega}\omega(\tau)\omega(t+\tau)d\tau$ denote the autocorrelation function of $\omega(\tau)$. Hence, we have

$$\begin{aligned} \mathrm{E}\left[\sigma_{1m}^2\right] &= \int_0^{T_c}\int_0^{T_c} G(t_1)G(t_1+(m-1)T_c)\varphi^2(t_2-t_1)dt_2 \\ &= \mathcal{E}_\varphi \int_0^{T_c} G(t)G(t+(m-1)T_c)dt \end{aligned} \tag{A.13}$$

where $\mathcal{E}_\varphi := \int_{-T_\omega}^{T_\omega}\varphi^2(t)dt$ captures the energy of $\varphi(t)$.

Computation of $\mathbf{E}\left[\mathcal{E}_m^2\right]$

Finally, we consider $\mathrm{E}\left[\mathcal{E}_m^2\right]$, which appears in the computation of $\mathrm{Var}[z_I]$. At low E_b/N_o, $\mathrm{Var}[z_I]$ has negligible effect on the $\sqrt{\mathrm{SINR}_{\overline{h}(t)}}$ because the effect of channel noise is dominant. Whereas at high E_b/N_o, the optimal T_c which maximizes $\sqrt{\mathrm{SINR}_{\overline{h}(t)}}$ is generally comparable to maximum excess delay of the channel. In this situation, the variances of $\{\mathcal{E}_m\}_{m=2}^M$ are relatively small compared to that of $\mathcal{E}_1$. Furthermore, because $2N_s^3 \gg \frac{N_s^2}{N_u-1}$ in (3.45 - 3.48), $\mathrm{E}\left[\mathcal{E}_m^2\right]$ has limited effect compared to $\mathrm{E}\left[\sigma_{1m}^2\right]$. Therefore, we approximate $\mathrm{E}\left[\mathcal{E}_m^2\right]$ as

$$\mathrm{E}\left[\mathcal{E}_m^2\right] \simeq \mathrm{E}^2\left[\mathcal{E}_m\right] = \mathcal{E}_\omega^2\left(\int_{(m-1)T_c}^{mT_c} G(t)dt\right)^2. \tag{A.14}$$

A.2 Derivation of T_c that Maximizes $\sqrt{\text{SINR}_{\overline{h}(t)}}$

Foremost, we differentiate $\sqrt{\text{SINR}_{\overline{h}(t)}}$ in (3.41) with respect to T_c and apply (3.50 - 3.52) to obtain

$$\frac{\partial\sqrt{\text{SINR}_{\overline{h}(t)}}}{\partial T_c} = \frac{1}{\Psi}N_s^2\mathcal{E}_\omega G(T_c) - \frac{1}{2\Psi^3}N_s^2\mathcal{E}_\omega\int_0^{T_c}G(t)dt\cdot\left(\frac{\partial\text{Var}\left[z_I\right]}{\partial T_c}+\frac{\partial\text{Var}\left[u\right]}{\partial T_c}\right) \tag{A.15}$$

where

$$\Psi = \sqrt{\text{Var}\left[z_I\right]+\text{Var}\left[u\right]}, \tag{A.16}$$

$$\begin{aligned}\frac{\partial\text{Var}\left[z_I\right]}{\partial T_c} &= 2N_s^3\mathcal{E}_\varphi\sum_{m=2}^{M}\left[G(T_c)G(mT_c)+\int_0^{T_c}G(t)\frac{dG(t+(m-1)T_c)}{dT_c}dt\right]+\frac{2N_s^2}{N_u-1}\\ &\quad\mathcal{E}_\omega^2\sum_{m=2}^{M}\left[(mG(mT_c)-(m-1)G(mT_c-T_c))\int_{(m-1)T_c}^{mT_c}G(t)dt\right],\end{aligned} \tag{A.17}$$

$$\frac{\partial\text{Var}\left[u\right]}{\partial T_c} = N_s^2N_o\mathcal{E}_\omega\left[N_sG(T_c)+\sum_{m=2}^{M}\left(mG(mT_c)-(m-1)G(mT_c-T_c)\right)\right]+\frac{N_s^2N_o^2W}{2}. \tag{A.18}$$

Corresponding to (3.54), we substitute (3.39) into (A.15 - A.18) and equate (A.15) to zero to get

$$2ae^{-bT_c}\Psi^2-\left(\frac{a(1-e^{-bT_c})}{b}+c\right)\cdot\left(\frac{\partial\text{Var}\left[z_I\right]}{\partial T_c}+\frac{\partial\text{Var}\left[u\right]}{\partial T_c}\right)=0 \tag{A.19}$$

where

$$\begin{aligned}\Psi^2 &= 2N_s^3\mathcal{E}_\varphi\left(\frac{a^2e^{-bT_c}}{2b}(1+e^{-bT_c})+\frac{ace^{-bT_c}}{1-e^{-bT_c}}\right)+\frac{a^2N_s^2\mathcal{E}_\omega^2e^{-2bT_c}(1-e^{-bT_c})}{b^2(N_u-1)(1+e^{-bT_c})}\\ &+ N_s^2N_o\mathcal{E}_\omega\left(N_s\frac{a(1-e^{-bT_c})}{b}+N_sc+\frac{ae^{-bT_c}}{b}\right)+\frac{N_s^2N_o^2WT_c}{2}, \qquad \text{(A.20)}\end{aligned}$$

$$\begin{aligned}\frac{\partial\mathrm{Var}\left[z_I\right]}{\partial T_c} &= 2N_s^3\mathcal{E}_\varphi\left(-\frac{a^2e^{-bT_c}}{2}(2e^{-bT_c}+1)-\frac{abce^{-bT_c}}{(1-e^{-bT_c})^2}\right)\\ &+ \frac{2a^2N_s^2\mathcal{E}_\omega^2e^{-2bT_c}(e^{-2bT_c}+e^{-bT_c}-1)}{b^2(N_u-1)(1+e^{-bT_c})^2}, \qquad \text{(A.21)}\end{aligned}$$

$$\frac{\partial\mathrm{Var}\left[u\right]}{\partial T_c}=N_s^2\left(N_s-1\right)N_o\mathcal{E}_\omega ae^{-bT_c}+\frac{N_s^2N_o^2W}{2}. \qquad \text{(A.22)}$$

In the equation (A.19 - A.22), the terms that contain e^{-MbT_c} are omitted since they are negligibly small compared to terms that contain e^{-bT_c} since $M \gg 1$. The T_c that maximizes $\sqrt{\mathrm{SINR}_{\overline{h}(t)}}$ can now be obtained by solving (A.19) numerically.

Appendix B

LDPC Product Codes

Low-density parity check (LDPC) codes were invented by Gallager [52] in 1962. After about 40 years, they had been rediscovered to be capable of achieving system performance remarkably close to the Shannon limit at reasonably low decoder complexity [53]. However, one practical drawback of LDPC codes has been that of high encoding complexity. Encoding is, in general, performed by matrix multiplication and the complexity grows with the square of the code length. In [92], Luby slightly modified the construction of codes from bipartite graphs to a cascade of such graphs for erasure channels. In [93–95], the LDPC codes were designed based on finite geometry and algebra. Low-density generator matrix (LDGM) codes were explored in [96]. In [97], product accumulate codes were proposed, which comprises the serial concatenation of a single-parity-check (SPC)-based product code, an interleaver, and a rate-1 recursive convolutional code. All these works are aimed towards reducing encoding complexity and/or decoding complexity of LDPC codes.

In this thesis, we propose to reduce the encoding complexity of LDPC codes

by employing two-dimensional LDPC product codes of equivalent code length and code rate. In view of the computational advantage of LDPC product codes, it is of interest to determine its feasibility by examining the trade-offs, if any, in terms of code design, decoding complexity, and code performance in noisy channels. Well known general properties of product codes that naturally carry over will not be reiterated here. The structure of the parity check matrix of an LDPC product code and its relationship with those of its components codes are discussed in Section B.1, where several important properties that can be used to guide the design of LDPC product codes are revealed. In section B.2, the encoding and decoding complexities of LDPC product codes are evaluated against those of LDPC codes. Depending on the choice of code parameters, it is observed that LDPC product codes can substantially reduce encoding complexity with virtually uncompromised decoding complexity. The computer simulation results are presented in Section B.3.

B.1 LDPC Product Code Structure

In this and subsequent sections, let $\boldsymbol{\mathcal{C}}_s$ denote a binary $(N_s, K_s, \lambda_s, \rho_s)$ linear block code which has length N_s, dimension K_s, a parity check matrix $\mathbf{H}_s$ with average column (row)-weight λ_s (ρ_s), and a generator matrix $\mathbf{G}_s$. $\mathbf{H}_s$ is not in systematic form. The generator matrix $\mathbf{G}_s = [\mathbf{P}_s|\mathbf{I}_s]$ is obtained from $\mathbf{H}_s$ by Gauss-Jordan elimination, where $\mathbf{I}_s$ is the identity $K_s \times K_s$ matrix and $\mathbf{P}_s$ the $K_s \times (N_s - K_s)$ parity matrix. The subscript "s" is an alphanumeric variable used for code identification. Unless otherwise specified, one-dimensional (1-D) vectors are assumed to be row vectors.

Starting with two LDPC component codes, $\boldsymbol{\mathcal{C}}_1$ and $\boldsymbol{\mathcal{C}}_2$, we form a two-dimensional

(2-D) product code $\boldsymbol{\mathcal{C}}_P$ for encoding an information vector $\mathbf{x} = [x_1, x_2, \cdots, x_{K_P}]$ into a codeword $\mathbf{y} = [y_1, y_2, \cdots, y_{N_P}]$, where $K_P = K_1 K_2$ and $N_P = N_1 N_2$. This is done by first rearranging $\mathbf{x}$ into a $K_2 \times K_1$ matrix $\mathbf{U} = [u_{i,j}]_{\substack{i=1\ldots K_2 \\ j=1\ldots K_1}}$ where $u_{i,j} = x_{(i-1)K_1+j}$, then computing

$$\mathbf{V} = [v_{i,j}]_{\substack{i=1\ldots N_2 \\ j=1\ldots N_1}} = \begin{bmatrix} \mathbf{v}_1 \\ \mathbf{v}_2 \\ \vdots \\ \mathbf{v}_{N_2} \end{bmatrix} = [\mathbf{G}_2]^\dagger \, \mathbf{U} \mathbf{G}_1, \tag{B.1}$$

where $\mathbf{v}_m$ is the m^{th}-row of $\mathbf{V}$, and $\dagger$ denotes vector (or matrix) transpose. The formation of the codeword

$$\mathbf{y} = [\mathbf{v}_1, \mathbf{v}_2, \cdots, \mathbf{v}_{N_2}] \tag{B.2}$$

completes the encoding process. Clearly, the code rate of $\boldsymbol{\mathcal{C}}_P$ is $(K_1 K_2)/(N_1 N_2)$. Since $\mathbf{V}$ satisfies $\mathbf{V}\mathbf{H}_1^\dagger = \mathbf{0}$ and $\mathbf{V}^\dagger \mathbf{H}_2^\dagger = \mathbf{0}$, it can be shown by inspection that the parity check matrix $\mathbf{H}_P$ which satisfies $\mathbf{y}\mathbf{H}_P^\dagger = \mathbf{0}$ has the form

$$\mathbf{H}_P = \begin{bmatrix} \boldsymbol{\Phi}_1 \\ \boldsymbol{\Phi}_2 \end{bmatrix} \tag{B.3}$$

where

$$\mathbf{\Phi}_1 = \begin{bmatrix} \mathbf{H}_1 & & & \\ & \mathbf{H}_1 & & \\ & & \ddots & \\ & & & \mathbf{H}_1 \end{bmatrix} \quad \text{Block} \rightarrow \begin{array}{cccc} 1 & & 2 & N_2 \end{array} \tag{B.4}$$

$$\mathbf{\Phi_2} = \begin{bmatrix} \mathbf{h}_1^2 & & & \mathbf{h}_2^2 & & & \mathbf{h}_{N_2}^2 & & \\ & \mathbf{h}_1^2 & & & \mathbf{h}_2^2 & & & \mathbf{h}_{N_2}^2 & \\ & & \ddots & & & \ddots & \cdots & & \ddots \\ & & \underbrace{\mathbf{h}_1^2}_{1} & & & \underbrace{\mathbf{h}_2^2}_{2} & & & \underbrace{\mathbf{h}_{N_2}^2}_{N_1} \end{bmatrix} \quad \text{Block} \rightarrow \tag{B.5}$$

in which $\mathbf{h}_j^2$ is the j^{th}-column of $\mathbf{H}_2$. Since $\mathbf{H}_1$ is $(N_1 - K_1) \times N_1$ and $\mathbf{H}_2$ is $(N_2 - K_2) \times N_2$, it is easy to see that $\mathbf{\Phi}_1$ is $N_2(N_1 - K_1) \times N_1 N_2$, $\mathbf{\Phi}_2$ is $N_1(N_2 - K_2) \times N_1 N_2$, and $\mathbf{H}_P$ is $[N_1(N_2 - K_2) + N_2(N_1 - K_1)] \times N_1 N_2$. Thus, although $\boldsymbol{\mathcal{C}}_P$ is an $(N_P, K_P, \lambda_P, \rho_P)$ product code, the usual implication that $\mathbf{H}_P$ has $(N_P - K_P)$ rows does not apply here. In fact, $\mathbf{H}_P$ has $(N_1 - K_1)(N_2 - K_2)$ rows in excess of $(N_P - K_P)$.

From (B.3 - B.5), we observe that each column of $\mathbf{H}_P$ contains one column of $\mathbf{H}_1$ and one column of $\mathbf{H}_2$. Also, each row of $\mathbf{H}_P$ contains either one row of $\mathbf{H}_1$ or one row of $\mathbf{H}_2$. This results in

$$\lambda_P = \lambda_1 + \lambda_2; \;\; \rho_P = \frac{\rho_1 N_2(N_1 - K_1) + \rho_2 N_1(N_2 - K_2)}{N_2(N_1 - K_1) + N_1(N_2 - K_2)} \tag{B.6}$$

Clearly, if $\mathbf{H}_1$ and $\mathbf{H}_2$ are sparse, then $\mathbf{H}_P$ will also be sparse. Thus, $\boldsymbol{\mathcal{C}}_P$ can be

viewed as an LDPC product code. Further, if $\boldsymbol{\mathcal{C}}_1$ and $\boldsymbol{\mathcal{C}}_2$ are both regular with $\rho_1 = \rho_2$, then $\boldsymbol{\mathcal{C}}_P$ is also regular.

A well known concern when applying LDPC codes with iterative decoding is that the bipartite graph representing the parity check matrix should not contain short cycles. Since $\mathbf{H}_P$ is constructed from $\mathbf{H}_\alpha(\alpha = 1, 2)$, it is important to determine how the cycle lengths in $\mathbf{H}_P$ are related to the cycle lengths in $\mathbf{H}_\alpha$'s. From (B.3 - B.5), the LDPC product code structure effectively prevents the sharing of a cycle between $\boldsymbol{\Phi}_1$ and $\boldsymbol{\Phi}_2$. The shortest cycle length (SCL) in $\mathbf{H}_P$ is then given by

$$\text{SCL in } \mathbf{H}_P = \min_{\alpha \in [1,2]} [\text{SCL in } \mathbf{H}_\alpha] \tag{B.7}$$

which provides an efficient mean of eliminating short cycles in $\mathbf{H}_P$ through $\mathbf{H}_1$ and $\mathbf{H}_2$.

B.2 Complexity Comparison

The encoding and decoding complexities of an LDPC product code $\boldsymbol{\mathcal{C}}_P$ and an LDPC code $\boldsymbol{\mathcal{C}}_L$ of comparable code parameter values are compared in this section.

B.2.1 Encoding Complexity

The 1-D code $\boldsymbol{\mathcal{C}}_L$, encodes a $1 \times K_L$ information vector $\mathbf{x}$ into a $1 \times N_L$ codeword $\mathbf{y}$ through $\mathbf{y} = \mathbf{x}\mathbf{G}_L$, which involves $K_L \times (N_L - K_L)$ "xor" operations. The 2-D product code $\boldsymbol{\mathcal{C}}_P$, encodes a $1 \times K_P$ information vector $\mathbf{x}$ into a $1 \times N_P$ codeword $\mathbf{y}$ through (B.1), which involves $(N_1 - K_1)K_1K_2 + (N_2 - K_2)K_2N_1$ "xor" operations. Assuming $\boldsymbol{\mathcal{C}}_P$, $\boldsymbol{\mathcal{C}}_L$ have the same code lengths $N_P = N_L = N_1N_2$ and same code

dimensions $K_P = K_L = K_1 K_2$, we define the encoding complexity (EC) ratio of the two codes as

$$\begin{aligned} \Omega_E &= \frac{\text{EC of } \boldsymbol{\mathcal{C}}_P}{\text{EC of } \boldsymbol{\mathcal{C}}_L} \\ &= \frac{(N_1 - K_1)K_1K_2 + (N_2 - K_2)K_2N_1}{(N_1N_2 - K_1K_2)K_1K_2} \\ &= \frac{K_1 + \zeta}{(K_2 + \zeta)K_1} \end{aligned} \tag{B.8}$$

where $\zeta = N_1(\frac{N_2 - K_2}{N_1 - K_1})$. From (B.8), it is easy to see that

$$\frac{1}{\max[K_1, K_2]} < \Omega_E < \frac{1}{\min[K_1, K_2]}. \tag{B.9}$$

Equation (B.9) indicates that a substantial reduction in encoding complexity can be achieved by using LDPC product codes since $K_1, K_2 > 1$ in practice.

B.2.2 Decoding Complexity

While the proposed LDPC product code $\boldsymbol{\mathcal{C}}_P$ is in principle a 2-D code, the formation of the composite parity check matrix $\mathbf{H}_P$ permits iterative decoding to be carried out in the usual ways as with 1-D LDPC code. The decoding complexities of belief propagation (BP) based algorithms [53], commonly used for LDPC codes, are functions of the code length, code dimension, and the code parity check matrix's column and row weights. Kou, et al [93] in fact reported that the BP algorithm has a decoding complexity order that depends only on the code length and the code parity check matrix's column weight. Given a $\boldsymbol{\mathcal{C}}_P$, if we can find a $\boldsymbol{\mathcal{C}}_L$ of matched parameters, then without further evaluation, we can safely assume that they both

have identical decoding complexity for any given BP-based iterative decoder.

B.3 Simulation Results

In this section, we compare the BER of LDPC product codes $\boldsymbol{\mathcal{C}}_P$ with that of LDPC codes $\boldsymbol{\mathcal{C}}_L$ for binary phase-shift-keying (BPSK) in AWGN channels. With $N_P = N_L = N'$, $K_P = K_L = K'$, and $\lambda_P = \lambda_L = \lambda'$, we match $\boldsymbol{\mathcal{C}}_P$ and $\boldsymbol{\mathcal{C}}_L$ as far as possible. Therefore, both $\boldsymbol{\mathcal{C}}_P$ and $\boldsymbol{\mathcal{C}}_L$ have the same code rate $R' = K'/N'$.

The codes under investigation are all rate $R' = 1/2$, with (N', K') equal to $(9000, 4500)$. The LDPC product code $\boldsymbol{\mathcal{C}}_P$ employs LDPC component codes $\boldsymbol{\mathcal{C}}_1$ and $\boldsymbol{\mathcal{C}}_2$, where $\boldsymbol{\mathcal{C}}_1$ is randomly generated $(1500, 900, 3, 15/2)$ LDPC code and $\boldsymbol{\mathcal{C}}_1$ is $(6, 5, 1, 6)$ linear block code. From (B.8), we compute that the encoding process with $\boldsymbol{\mathcal{C}}_P$ is about 7.479 times faster than with $\boldsymbol{\mathcal{C}}_L$. The column weight (λ') of $\boldsymbol{\mathcal{C}}_P$ is 4. We also generate the LDPC code $\boldsymbol{\mathcal{C}}_L$, which has parity check matrix with column weight (λ') equals 4. Length-4 cycles are removed from the parity check matrices of both LDPC codes and LDPC product component codes. Decoding is carried out with the BP algorithm [53] where the maximum iteration number is 50. Curves A and C in Fig. B.1 show the computer simulated BER results. Here, we observe that the LDPC product code outperforms its counterpart LDPC code.

Generally, LDPC codes with column weight 3 have better error performance than those with column weight 4. Therefore, we also present the simulation results of the LDPC code with (N', K', λ') values of $(9000, 4500, 3)$. In Fig. B.1, we observe that the LDPC product code outperforms the $(9000, 4500, 3)$ LDPC code for SNR values below 2.3 dB. At higher SNR, the LDPC product code is found to give poorer BER performance compared to the LDPC code.

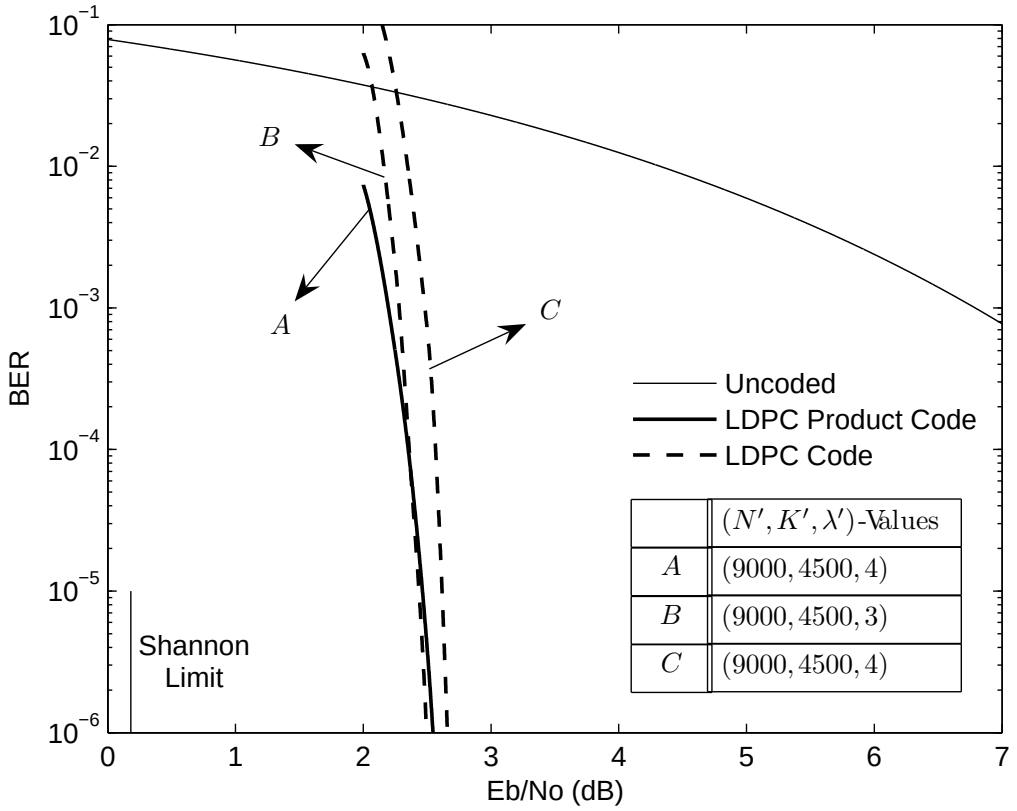

Fig. B.1: BERs of LDPC product code and LDPC code in AWGN channels for various values of N', K' and λ'.

B.4 Summary

In this appendix, we proposed LDPC product codes as a mean of achieving reduced complexity encoding when compared to LDPC codes. The parity check matrix of the product code was constructed from those of its component codes. The relationships between their code lengths, code dimensions, column weights, and row weights, which could serve as guidelines for the design of LDPC product codes, were determined. On comparing LDPC product codes and LDPC codes of identical code lengths and code rates, it was found that the former could achieve significant

reduction in encoding complexity with virtually no impact on decoding complexity. Computer simulation results showed that with the same column weight of 4, LDPC product code outperforms the LDPC code when code length is sufficiently long. Compared with column weight 3 LDPC codes, the proposed LDPC product code leads to lower BER at low SNR, and higher BER at high SNR values. In summary, for cases of long code length and large code dimension, LDPC product codes were shown to be attractive alternatives to LDPC codes in terms of reduced encoding complexity and improved BER performance at low SNR.

Appendix C

Theorems in Maximum Distance Code Design for DSTC MIMO d^2TD-IR Systems

---

C.1 Maximum Distance Code Design Preliminaries

Here, for completeness, we provide the definition of a group [98] and the necessary and sufficient condition for a code Ω to have a minimum code distance of $2N$.

***Definition* C.1.** *A group is an ordered pair $(G, \circ)$, where G is a set and $\circ$ is a binary operation on G satisfying the following axioms:*

- $(a \circ b) \circ c = a \circ (b \circ c)$, *for all* $a, b, c \in G$, *i.e.,* $\circ$ *is associative.*
- *There exists an element* e *in* G, *called the identity of* G, *such that for all* $a \in G$, $a \circ e = e \circ a = a$.
- *For each* $a \in G$, *there exists an element* a^{-1} *of* G, *called an inverse of* a, *such that* $a \circ a^{-1} = a^{-1} \circ a = e$.

Normally, the binary operation is called multiplication. In brief, a group is a set of elements that is closed under both multiplication and inversion.

From *Definition* C.1, we know that if the code Ω forms a group, $\mathbf{I}$ is the identity of Ω. In general, let $\mathbf{U}$ and $\mathbf{U}'$, which are $N \times N$ matrices specified in Section 6.1, be two codewords of a code Ω with alphabet size N_Ω. The code distance $\Lambda(\mathbf{U}, \mathbf{U}')$ takes on at most $N_\Omega(N_\Omega - 1)/2$ distinct values. Therefore, when N_Ω is large, the minimum value of $\Lambda(\mathbf{U}, \mathbf{U}')$ may be quite small. If Ω forms a group, $\Lambda(\mathbf{U}, \mathbf{U}')$ takes on at most $K - 1$ distinct values [88].

***Theorem* C.1.** *If the code* Ω *forms a group, the necessary and sufficient condition for* Ω *to be maximum distance codes is that all the codewords except* $\mathbf{I}$ *of* Ω *have zero trace.*

Proof. Let $N \times N$ orthogonal matrices $\mathbf{U}$ and $\mathbf{U}'$ be codewords of Ω. If the code Ω forms a group, there exists a matrix $\mathbf{U}'' \in \Omega$ which satisfies $\mathbf{U}'' = \mathbf{U}^{-1}\mathbf{U}'$.

Therefore,

$$\begin{aligned}
\Lambda(\mathbf{U},\mathbf{U}') &= \mathrm{Tr}\left\{(\mathbf{U}-\mathbf{U}')(\mathbf{U}-\mathbf{U}')^{\dagger}\right\} \\
&= \mathrm{Tr}\left\{\mathbf{U}(\mathbf{I}-\mathbf{U}'')(\mathbf{I}-\mathbf{U}'')^{\dagger}\mathbf{U}^{\dagger}\right\} \\
&= \mathrm{Tr}\left\{(\mathbf{I}-\mathbf{U}'')(\mathbf{I}-\mathbf{U}'')^{\dagger}\right\} \qquad \text{(C.1)} \\
&= \mathrm{Tr}(2\mathbf{I}) - \mathrm{Tr}(\mathbf{U}'') - \mathrm{Tr}\left(\mathbf{U}''^{\dagger}\right) \\
&= 2N - 2\mathrm{Tr}(\mathbf{U}'').
\end{aligned}$$

If and only if all the codewords except $\mathbf{I}$ of Ω have zero trace, the code Ω has a minimum code distance of $2N$. □

C.2 Eigenvalues of U

The properties of eigenvalues of the matrix $\mathbf{U}$ are examined in this subsection, where we prove that the matrix $\mathbf{U}$ that contains $e^{i\pi/N}$ as its eigenvalue does exist and the codes found by using the method in Section 6.3 are maximum distance codes.

***Theorem* C.2.** $\mathbf{U}$ *contains no eigenvalue of* $e^{i\theta}$ *where* $0 < \theta < \pi/N$.

In order to prove this theorem, we need to prove the following lemma first.

***Lemma* C.1.** *All the nonzero entries of an eigenvector of* $\mathbf{U}$ *have the same magnitude.*

Proof. Suppose $e^{i\theta}$ is an eigenvalue of $\mathbf{U}$ and $\mathbf{x}$ is the corresponding eigenvector,

$$\mathbf{U}\mathbf{x} = e^{i\theta}\mathbf{x}. \tag{C.2}$$

Because every column and every row of $\mathbf{U}$ have only one nonzero entry, which is either -1 or 1, the multiplication of $\mathbf{U}$ and $\mathbf{x}$ is equivalent to the permutation of the entries in $\mathbf{x}$ with sign variations according to $\mathbf{U}$. To achieve (C.2), the nonzero entries in $\mathbf{x}$ must have the same magnitude. □

Proof of Theorem C.2. Suppose $e^{i\theta}$, $0 < \theta < \pi/N$ is an eigenvalue of $\mathbf{U}$ and the eigenvector corresponding to the eigenvalue has no zero entry, namely

$$\mathbf{U}\mathbf{x} = \mathbf{U}\begin{pmatrix} \gamma e^{ix_1} \\ \gamma e^{ix_1} \\ \vdots \\ \gamma e^{ix_N} \end{pmatrix} = \begin{pmatrix} \gamma e^{i(x_1+\theta)} \\ \gamma e^{i(x_1+\theta)} \\ \vdots \\ \gamma e^{i(x_N+\theta)} \end{pmatrix} = e^{i\theta}\mathbf{x}. \tag{C.3}$$

Since all the entries in $\mathbf{U}$ take on values from $\{-1, 0, 1\}$, we have

$$\begin{aligned} x_{f(1)} + \text{sign}_1 \cdot \pi &= x_1 + \theta; \\ x_{f(2)} + \text{sign}_2 \cdot \pi &= x_2 + \theta; \\ &\cdots \\ x_{f(N)} + \text{sign}_N \cdot \pi &= x_N + \theta \end{aligned} \tag{C.4}$$

where $f(\bullet)$ means the permutation of $\{1, 2, \cdots, N\}$ according to $\mathbf{U}$, and sign_n is the sign of the nonzero entry of the n^{th} row of $\mathbf{U}$, i.e., $\text{sign}_n = 0$ if the nonzero entry is positive and $\text{sign}_n = 1$ otherwise. If (C.3) has the solution $\{x_1, x_2, \cdots, x_N\}$, the

region of $[0, 2\pi)$ should be fully covered with N subregions, where each subregion is $(x_n - \theta/2, x_n + \theta/2] \cup (-x_n - \theta/2, -x_n + \theta/2]$, $n = 1, 2, \cdots, N$. However, because $2N\theta < 2\pi$, the region $[0, 2\pi)$ cannot be covered seamlessly. Therefore, (C.4) has no solution. The existence of zero entries in the eigenvector corresponding to the eigenvalue $e^{i\theta}$ will further deteriorate the situation. This proves that $\mathbf{U}$ has no eigenvalue of $e^{i\theta}$, where $0 < \theta < \frac{\pi}{N}$. □

***Theorem* C.3.** *The eigenvalues of* $\mathbf{U}$ *belong to the set* $\{e^{il\pi/n}\}$*, where* $l \in \{1, 2, \cdots, 2N\}$ *and* $n \in \{1, 2, \cdots, N\}$.

Proof. Because in general, the eigenvector $\mathbf{x}$ corresponding to the eigenvalue $e^{i\theta}$ may contain zero entries, we remove all the zero entries in $\mathbf{x}$ and denote the remaining vector as $\mathbf{x}' = [\gamma e^{ix_1}, \gamma e^{ix_2}, \cdots, \gamma e^{ix_n}]^\dagger$. Accordingly, remove all corresponding rows and columns in $\mathbf{U}$ and denote the remaining matrix as $\mathbf{U}' = [\mathbf{u}_1, \mathbf{u}_2, \cdots, \mathbf{u}_n]^\dagger$, where $\mathbf{u}_1, \mathbf{u}_2, \cdots, \mathbf{u}_n$ are row vectors. From (C.2), we have

$$\mathbf{U}'\mathbf{x}' = \begin{pmatrix} \mathbf{u}_1\mathbf{x}' \\ \mathbf{u}_2\mathbf{x}' \\ \vdots \\ \mathbf{u}_n\mathbf{x}' \end{pmatrix} = \begin{pmatrix} \gamma e^{i(x_1+\theta)} \\ \gamma e^{i(x_1+\theta)} \\ \vdots \\ \gamma e^{i(x_n+\theta)} \end{pmatrix} = e^{i\theta}\mathbf{x}'. \tag{C.5}$$

To satisfy (C.5), every row of $\mathbf{U}'$ has one nonzero entry, which is either -1 or 1. Therefore,

$$\begin{aligned} x_{f'(1)} + \text{sign}_1 \cdot \pi &= x_1 + \theta; \\ x_{f'(2)} + \text{sign}_2 \cdot \pi &= x_2 + \theta; \\ &\cdots \\ x_{f'(n)} + \text{sign}_n \cdot \pi &= x_n + \theta \end{aligned} \tag{C.6}$$

where $f'(\bullet)$ means the permutation of $\{1, 2, \cdots, n\}$ according to $\mathbf{U}'$. To be the solution of (C.6), $\{x_1, x_2, \cdots x_n\}$ partitions the region of $[0, 2l\pi)$, $l \in \{1, 2, \cdots, 2n\}$ into n adjacent subregions, where each subregion is $(x_n - l\pi/(2n), x_n + l\pi/(2n)] \cup (-x_n - l\pi/(2n), -x_n + l\pi/(2n)]$. Possible θ values that satisfy (C.6) are $l\pi/n$. □

***Theorem* C.4.** *There exists* $\mathbf{U}$ *which has the eigenvalue of* $e^{i\pi/N}$.

Proof. We use $\{x_1, x_2, \cdots x_N\}$ to partition the region of $[0, 2\pi)$ into N adjacent subregions, where each subregion is $(x_n - \pi/(2N), x_n + \pi/(2N)] \cup (-x_n - \pi/(2N), -x_n + \pi/(2N)]$. This is a possible solution for (C.6), where $n = N$. Accordingly, we can find $\mathbf{U}$ which has the eigenvalue of $e^{i\pi/N}$. □

***Theorem* C.5.** *If* $e^{i\theta}$ *is an eigenvalue of* $\mathbf{U}$*, so are* $\{e^{i3\theta}, e^{i5\theta}, \cdots, e^{i(2N-1)\theta}\}$.

Proof. If $e^{i\theta}$ is an eigenvalue of $\mathbf{U}$, there exists a solution $\{x_1, x_2, \cdots, x_n\}$ satisfying (C.6). When multiplying both sides of (C.6) with $3, 5, \cdots, (2N-1)$, the formula (C.6) is also satisfied. Therefore, $\{e^{i3\theta}, e^{i5\theta}, \cdots, e^{i(2N-1)\theta}\}$ are also the eigenvalues of $\mathbf{U}$. □

***Corollary* C.1.** *There exists* $\mathbf{U}$ *with eigenvalues of* $\{e^{i\pi/N}, e^{i3\pi/N}, \cdots, e^{i(2N-1)\pi/N}\}$.

***Theorem* C.6.** *The set* $\Omega = \{\mathbf{U}^n, n = 1, 2, \cdots, 2N\}$ *forms a group, where* $\mathbf{U}$ *has eigenvalues of* $\{e^{i\pi/N}, e^{i3\pi/N}, \cdots, e^{i(2N-1)\pi/N}\}$.

Proof. The set Ω satisfies all the requirements of a group. First, the multiplication of the matrices is associative. Second, $\mathbf{I}$ is the identity of Ω. Finally, because

$$\mathbf{U}^{2N} = \mathbf{I}, \tag{C.7}$$

for each element $\mathbf{U}^n$ in the set, the inverse $\mathbf{U}^{2N-n}$ exists. Therefore, the set $\{\mathbf{U}^n, n = 1, 2, \cdots, 2N\}$ forms a group. □

C.3 Other Extensions

The following theorem will compute the number of $\mathbf{U}$'s that contain $e^{i\pi/N}$ as their eigenvalues.

***Theorem* C.7.** *There are* $2^{N-1}(N-1)!$ *different* $\mathbf{U}$*'s that contain* $e^{i\pi/N}$ *as their eigenvalues.*

Proof: From the proof of *Theorem* C.2 and *Theorem* C.3, we observe that if $\mathbf{U}$ contains $e^{i\pi/N}$ as its eigenvalue, the eigenvector corresponding to the eigenvalue $e^{i\pi/N}$ should have no zero entry and satisfy (C.3) and (C.4), where $\theta = \pi/N$. To find all the solutions of (C.4) without considering the signs of the entries in $\mathbf{U}$ is then a circular permutation problem. There is a total of $(N-1)!$ different solutions.

Now, consider the the signs of the entries in $\mathbf{U}$. If $\mathbf{U}$ contains even number of -1, (C.4) can be rewritten in the following form

$$\begin{aligned} x'_{f(1)} &= x'_1 + \theta; \\ x'_{f(2)} &= x'_2 + \theta; \\ &\cdots \\ x'_{f(N)} &= x'_N + \theta \end{aligned} \tag{C.8}$$

where $x'_n = x_n$ or $x'_n = x_n + \pi$. If (C.8) has the solution $\{x'_1, x'_2, \cdots, x'_N\}$, the region of $[0, 2\pi)$ should be fully covered by N subregions, where each subregion is $(x_n - \theta/2, x_n + \theta/2]$, $n = 1, 2, \cdots, N$. The smallest solution θ for (C.8) is $2\pi/N$.

Therefore, if $\mathbf{U}$ contains $e^{i\pi/N}$ as its eigenvalue, the number of -1 among the entries of $\mathbf{U}$ should be odd. Since

$$\begin{pmatrix} N \\ 1 \end{pmatrix} + \begin{pmatrix} N \\ 3 \end{pmatrix} + \begin{pmatrix} N \\ 5 \end{pmatrix} + \cdots = 2^{N-1}, \tag{C.9}$$

there are $2^{N-1}(N-1)!$ different $\mathbf{U}$'s that contain $e^{i\pi/N}$ as their eigenvalues. □

In Section 6.3, it has been shown that in ISI channel, the code with Toeplitz structure should have better performance. To design maximum distance codes with Toeplitz structure, the following theorem proves that we only need to find the generator $\mathbf{U}$ which is Toeplitz matrix.

***Theorem* C.8.** *If* $\mathbf{U}$ *is a codeword of* Θ *and* $\mathbf{U}$ *is Toeplitz matrix, so is* $\mathbf{U}^n$.

Proof. Let $e^{i\theta_n}$ and $\mathbf{x}_n$, $n = 1, 2, \cdots, N$, be the eigenvalue and eigenvector of $\mathbf{U}$, respectively. $\mathbf{U}$ can be expressed as

$$\mathbf{U} = e^{i\theta_1}\mathbf{x}_1\mathbf{x}_1^H + e^{i\theta_2}\mathbf{x}_2\mathbf{x}_2^H + \cdots + e^{i\theta_N}\mathbf{x}_N\mathbf{x}_N^H \tag{C.10}$$

where H denotes the transpose and conjugate operation. We also have

$$\mathbf{I} = \mathbf{x}_1\mathbf{x}_1^H + \mathbf{x}_2\mathbf{x}_2^H + \cdots + \mathbf{x}_N\mathbf{x}_N^H. \tag{C.11}$$

Therefore, $\mathbf{U} - a\mathbf{I}$ is Toeplitz matrix for $-\infty < a < \infty$. Because the eigenvectors are independent with one another, we know $\mathbf{x}_n\mathbf{x}_n^H$ is Toeplitz matrix. Since

$$\mathbf{U}^n = e^{in\theta_1}\mathbf{x}_1\mathbf{x}_1^H + e^{in\theta_2}\mathbf{x}_2\mathbf{x}_2^H + \cdots + e^{in\theta_N}\mathbf{x}_N\mathbf{x}_N^H, \tag{C.12}$$

$\mathbf{U}^n$ is also Toeplitz matrix. □

Bibliography

[1] D. Porcino and W. Hirt, "Ultra-wideband radio technology: potential and challenges ahead," *IEEE, Commun. Mag.*, vol. 41, pp. 66-74, July 2003.

[2] L. Yang and G. B. Giannakis, "Ultra-wideband communications: an idea whose time has come," *IEEE Signal Process. Mag.*, vol. 21, pp. 26-54, Nov. 2004.

[3] G. F. Ross, "The transient analysis of certain TEM mode four-port networks," *IEEE Trans. Microwave Theory and Tech.*, vol. 14, pp. 528-547, 1966.

[4] G. F. Ross, "A time domain criterion for the design of wideband radiating elements," *IEEE Trans. Antennas Propagat.*, vol. 16, pp. 355-356, 1968.

[5] C. L. Bennett and G. F. Ross, "Time-domain electromagnetics and its applications," in *Proc. of the IEEE 1978*, pp. 299-318.

[6] K. Robbins, "Short base-band pulse receiver," *U. S. Patent*, No. 3,662,316, 1972.

[7] M. Z. Win and R. A. Scholtz, "Impulse radio: how it works," *IEEE Commun. Lett.*, vol. 2, pp. 36-39, Feb. 1998.

[8] M. Z. Win and R. A. Scholtz, "Ultra-wide bandwidth time-hopping spread-spectrum impulse radio for wireless multiple-access communications," *IEEE Trans. Commun.*, vol. 48, pp. 679-691, Apr. 2000.

[9] FCC, "Revision of part 15 of the commission's rules regarding ultra-wideband transmission system: first report and order," *Technical report, U.S. Federal Communications Commission*, Feb. 2002.

[10] A. Batra et al, "Multi-band OFDM Physical Layer Proposal for IEEE 802.15 Task Group 3a," *IEEE P802.15-03/268r2*, Nov. 2003.

[11] C. Snow, L. Lampe, and R. Schober, "Performance analysis of multiband OFDM for UWB communication," in *Proc. ICC 2005*, pp. 2573-2578.

[12] W. P. Siriwongpairat, W. Su, M. Olfat, and K. J. R. Liu, "Multiband-OFDM MIMO coding framework for UWB communication systems," *IEEE Trans. Signal Process.*, vol. 54, pp. 214-224, Jan. 2006.

[13] J. R. Foerster, "The performance of a direct-sequence spread ultra-wideband system in the presence of multipath, narrowband interference, and multiuser interference," in *Proc. UWBST 2002*, pp. 87-91.

[14] L. Qinghua and L. A. Rusch, "Multiuser detection for DS-CDMA UWB in the home environment," *IEEE J. Select. Areas Commun.*, vol. 20, pp. 1701-1711, Dec. 2002.

[15] L. Piazzo, "Performance analysis and optimization for impulse radio and direct-sequence impulse radio in multiuser interference," *IEEE Trans. Commun.*, vol. 52, pp. 801-810, May 2004.

[16] L. Piazzo and F. Ameli, "Performance analysis for impulse radio and direct-sequence impulse radio in narrowband interference," *IEEE Trans. Commun.*, vol. 53, pp. 1571-1580, Sep. 2005.

[17] C. J. L. Martret and G. B. Giannakis, "All-digital PAM impulse radio for multiple-access through frequency-selective multipath," in *Proc. GLOBECOM 2000*, vol. 1, pp. 77-81.

[18] R. A. Scholtz, "Multiple access with time-hopping impulse modulation," in *Proc. MILCOM 1993*, vol. 2, pp. 447-450.

[19] M. Hamalainen, R. Tesi, J. Iinatti, and V. Hovinen, "On the performance comparison of different UWB data modulation schemes in AWGN channel in the presence of jamming," in *Proc. RAWCON 2002*, pp. 83-86.

[20] J. A. N. Silva and M. L. R. Campos, "Orthogonal pulse shape modulation for impulse radio," in *Proc. ITS 2002*, 47-51.

[21] I. Guvenc and H. Arslan, "On the modulation options for UWB systems," in *Proc. MILCOM, 2003*, 892-897.

[22] W. Suwansantisuk, M. Z. Win, and L. A. Shepp, "On the performance of wide-bandwidth signal acquisition in dense multipath channels," *IEEE Trans. Veh. Technol.*, vol. 54, pp. 1584-1594, Sep. 2005.

[23] V. Lottici, A. D'Andrea, and U. Mengali, "Channel estimation for ultra-wideband communications," *IEEE J. Select. Areas Commun.*, vol. 20, pp. 1638-1645, Dec. 2002.

[24] M. Z. Win and R. A. Scholtz, "On the robustness of ultra-wide bandwidth signals in dense multipath environments," *IEEE Commum. Lett.*, vol. 2, pp. 51-53, Feb. 1998.

[25] M. Z. Win and Z. A. Kostic, "Virtual path analysis of selective Rake receiver in dense multipath channels," *IEEE Commun. Lett.*, vol. 3, pp. 308-310, Nov. 1999.

[26] M. Z. Win, G. Chrisikos, and N. R. Sollenberger, "Performance of Rake reception in dense multipath channels: implications of spreading bandwidth and selection diversity order," *IEEE J. Select. Areas Commun.*, vol. 18, pp. 1516-1525, Aug. 2000.

[27] E. Fishler and H. V. Poor, "Low-complexity multiuser detectors for time-hopping impulse-radio systems," *IEEE Trans. Signal Process.*, vol. 52, pp. 2561-2571, Sep. 2004.

[28] S. Gezici, H. Kobayashi, H. V. Poor, and A. F. Molisch, "Performance evaluation of impulse radio UWB systems with pulse-based polarity randomization," *IEEE Trans. Signal Process.*, vol. 53, pp. 2537-2549, July 2005.

[29] M. Z. Win, "A unified spectral analysis of generalized time-hopping spread-spectrum signals in the presence of timing jitter," *IEEE J. Select. Areas Commun.*, vol. 20, pp. 1664-1676, Dec. 2002.

[30] R. T. Hoctor and H. W. Tomlinson, "Delay-hopped transmitted-reference RF communications," in *Proc. UWBST 2002*, pp. 289-292.

[31] M. Ho, V. S. Somayazulu, J. Foerster, and S. Roy, "A differential detector for an ultra-wideband communications system," in *Proc. VTC 2002-Spring*, pp. 1896-1900.

[32] J. D. Choi and W. E. Stark, "Performance of ultra-wideband communications with suboptimal receivers in multipath channels," *IEEE J. Select. Areas Commun.*, vol. 20, pp. 1754-1766, Dec. 2002.

[33] T. Q. S. Quek and M. Z. Win, "Analysis of UWB transmitted-reference communication systems in dense multipath channels," *IEEE J. Select. Areas Commun.*, vol. 23, pp. 1863-1874, Sep. 2005.

[34] H. Ning and C. Tepedelenlioglu, "Performance analysis of non-coherent UWB receivers at different synchronization levels," *IEEE Trans. Wireless Commun.*, vol. 5, pp. 1266-1273, June 2006.

[35] Y. -L. Chao and R. A. Scholtz, "Optimal and suboptimal receivers for ultra-wideband transmitted reference systems," in *Proc. GLOBECOM 2003*, pp. 759-763.

[36] L. Yang and G. B. Giannakis, "Optimal pilot waveform assisted modulation for ultrawideband communications," *IEEE Trans. Wireless Commun.*, vol. 3, pp. 1236-1249, July 2004.

[37] F. Tufvesson and A. F. Molish, "Ultra-wideband communication using hybrid matched filter correlation receivers," in *Proc. VTC 2004-Spring*, pp. 1290-1294.

[38] S. Gezici, F. Tufvesson, and A. F. Molisch, "On the Performance of Transmitted-Reference Impulse Radio," in *Proc. GLOBECOM 2004*, pp. 2874-2879.

[39] K. Witrisal, G. Leus, M. Pausini, and C. Krall, "Equivalent system model and equalization of differential impulse radio UWB systems," *IEEE J. Select. Areas Commun.*, vol. 23, pp. 1851-1862, Sep. 2005.

[40] Q. Zhang and C. S. Ng, "Differential TDMA impulse radio systems using delay-sum scheme in UWB channel," in *Proc. GLOBECOM 2005*, pp. 3670-3675.

[41] S. Franz and U. Mitra, "Generalized UWB transmitted reference systems," *IEEE J. Select. Areas Commun.*, vol. 24, pp. 780-786, Apr. 2006.

[42] J. Romme and K. Witrisal, "Transmitted-reference UWB systems using weighted autocorrelation receivers," *IEEE Trans. Microwave Theory Tech.*, vol. 54, pp. 1754-1761, June 2006.

[43] X. Zhengyuan and B. M. Sadler, "Multiuser transmitted reference ultra-wideband communication systems," *IEEE J. Select. Areas Commun.*, vol. 24, pp. 766-772, Apr. 2006.

[44] IEEE, "Channel Modeling Sub-committee Report Final," *IEEE P802.15-02/368r5-SG3a*.

[45] X. Zhong, S. Mei, Y. Wang, and W. Jing, "Synchronization in TDMA ad hoc network," in *Proc. VTC 2004-Fall*, pp. 5011-5014.

[46] Y. Su, S. Su, and J. Li, "Topology-transparent node activation scheduling schemes for multihop TDMA ad hoc networks," in *Proc. GLOBECOM 2004*, pp. 68-73.

[47] O. Dousse, F. Baccelli, and P. Thiran, "Impact of interferences on connectivity in ad hoc networks," *IEEE/ACM Trans. Networking*, vol. 13, pp. 425-436, Apr. 2005.

[48] X. Wu, B. S. Sharif, O. R. Hinton, and C. C. Tsimenidis, "Solving optimum TDMA broadcast scheduling in mobile ad hoc networks: a competent permutation genetic algorithm approach," in *Proc. Commun. 2005*, pp. 780-788.

[49] D. L. Goeckel and Q. Zhang, "Slightly frequency-shifted reference ultra-wideband (UWB) radio: TR-UWB without the delay element," in *Proc. MILCOM 2005*, pp. 1-7.

[50] S. Bagga, L. Zhang, W. A. Serdijin, J. R. Long, and E. B. Busking, "A quantized analog delay for an ir-UWB quadrature downconversion autocorrelation receiver," in *Proc. ICU 2005*, pp. 328-332.

[51] H. Ning and C. Tepedelenlioglu, "Adaptive synchronization for non-cohenrent UWB receivers," in Proc. ICASSP 2004, pp. 517-520.

[52] R. G. Gallager, *Low-Density Parity-Check Codes*. Cambridge: MIT Press, 1963.

[53] D. J. C. MacKay, "Good error correcting codes based on very sparse matrices," *IEEE Trans. Inform. Theory*, vol. 45, pp. 399-431, Mar. 1999.

[54] T. J. Richardson and R. Urbanke, "The capacity of low-density parity-check codes under message-passing decoding," *IEEE Trans. Inform. Theory*, vol. 47, pp. 599-618, Feb. 2001.

[55] T. J. Richardson, A.Shokrollali, and R. Urbanke, "Design of capacity-approaching irregular low-density parity-check codes," *IEEE Trans. Inform. Theory*, vol. 47, pp. 619-637, Feb. 2001.

[56] C. Berrou, A. Glavieux, and P. Thitimajshima, "Near Shannon limit error-correcting coding and decoding: Turbo-codes (1)," in *Proc. ICC 1993*, pp. 1064-1070.

[57] J. G. J. Foschini and M. J. Gans, "On limits of wireless communication in a fading environment when using multiple antennas," *Wireless Personal Commun.*, pp. 311-335, Mar. 1998.

[58] I. E. Telatar, "Capacity of multi-antenna Gaussian channel," *Eur. Trans. Telecom*, vol. 10, pp. 585-595, Nov. 1999.

[59] V. Tarokh, N. Seshadri, and A. R. Calderbank, "Space-time codes for high data rate wireless communication: Performance criterion and code construction," *IEEE Trans. Inform. Theory*, vol. 44, pp. 744-765, Mar. 1998.

[60] S. Alamouti, "A simple transmitter diversity technique for wireless communications," *IEEE J. Select. Areas. Commun.*, vol. 16, pp. 1451-1458, Oct. 1998.

[61] B. M. Hochwald and T. L. Marzetta, "Unitary space-time modulation for multiple-antenna communications in rayleigh flat fading," *IEEE Trans. Inform. Theory*, vol. 46, pp. 543-563, Mar. 2000.

[62] B. L. Hughes, "Differential space-time modulation," *IEEE Trans. Inform. Theory*, vol. 46, pp. 2567-2578, Nov. 2000.

[63] B. M. Hochwald and W. Sweldens, "Differential unitary space-time modulation," *IEEE Trans. Commun.*, vol. 48, pp. 2041-2052, Dec. 2000.

[64] R. C. Qiu, C. Zhou, N. Guo, and J. Q. Zhang, "Time Reversal With MISO for Ultrawideband Communications: Experimental Results," *IEEE Antenna and Wireless propagation Lett.*, vol. 5, pp. 269-273, 2006.

[65] M. Weisenhorn and W. Hirt, "Performance of binary antipodal signaling over the indoor UWB MIMO channel," in *Proc. ICC 2003*, pp. 2872-2878.

[66] L. Yang and G. B. Giannakis, "Analog space-time coding for multiantenna ultra-wideband transmissions," *IEEE Trans. Commun.*, vol. 52, pp. 507-517, Mar. 2004.

[67] E. Baccarelli, M. Biagi, C. Pelizzoni, and P. Bellotti, "A novel multi-antenna impulse radio UWB transceiver for broadband high-throughput 4G WLANs," *IEEE Commun. Lett.*, vol. 8, pp. 419-421, July 2004.

[68] A. Paulraj, R. Nabar, and D. Gore, *Introduction to Space-Time Wireless Communications*. Cambridge, UK: Cambridge University, 2003.

[69] M. G. Benedetto and G. Giancola, *Understanding Ultra Wide Band Radio Fundamentals*. New Jersey: Prentice-Hall, 2004.

[70] S. B. M. Acheroy and A. V. Vost, "Time-domain simulation and characterization of TEM horns using a normalized impulse response," in *Proc. Microwave Antenna Propagation 2000*, pp. 463-468.

[71] B. Parr, B. Cho, K. Wallace, and Z. Ding, "A novel ultra-wideband pulse design algorithm," *IEEE Commun. Lett.*, vol. 7, pp. 219-221, May 2003.

[72] X. Wu, Z. Tian, T. N. Davidson, and G. B. Giannakis, "Optimal waveform design for UWB radios," *IEEE Trans. Signal Process.*, vol. 54, pp. 2009-2021, June 2006.

[73] F. Ramirez-Mireles, "Performance of ultrawideband SSMA using time hopping and M-ary PPM," *IEEE J. Select. Areas Commun.*, vol. 19, pp. 1186-1196, June 2001.

[74] N. V. Kokkalis, P. T. Mathiopoulos, G. K. Karagiannidis, and C. S. Koukourlis, "Performance analysis of M-ary PPM TH-UWB systems in the presence of MUI and timing jitter," *IEEE J. Select. Areas Commun.*, vol. 24, pp. 822-828, Apr. 2006.

[75] T. Wang and Y. Wang, "Capacity of M-ary PAM impulse radio with various derivatives of Gaussian pulse subject to FCC spectral masks," in *Proc. ISCC 2004*, 696-701.

[76] J. A. N. Silva and M. L. R. Campos, "Performance comparison of binary and quaternary UWB modulation schemes," in *Proc. GLOBECOM 2003*, 789-793.

[77] K. Usuda, H. Zhang, and M. Nakagawa, "M-ary pulse shape modulation for PSWF-based UWB systems in multipath fading environment," in *Proc. GLOBECOM 2004*, 3498-3504.

[78] A. Molisch, M. Z. Win, and D. Cassioli, "The ultra-wide bandwidth indoor channel: from statistical model to simulations," *IEEE J. Select. Areas Commun.*, vol. 20, pp. 1247-1257, Aug. 2002.

[79] D. Cassioli, M. Z. Win, and A. Molisch, "A statistical model for UWB indoor channel," in *Proc. VTC 2001-Spring*, pp. 1159-1163.

[80] W. Turin, R. Jana, S. S. Ghassemzadeh, C. W. Rice, and T. Tarokh, "Autoregressive modeling of an indoor UWB channel," in *Proc. UWBST 2002*, pp. 71-74.

[81] A. Saleh and R. Valenzuela, "A statistical model for indoor multipath propagation," *IEEE J. Select. Areas Commun.*, vol. SAC-5, pp. 128-137, Feb. 1987.

[82] S. Verdu, *Multiuser Detecion*. Cambridge, UK: Cambridge University Press, 1998.

[83] D. Cassioli, M. Z. Win, F. Vatalaro, and A. F. Molisch, "Performance of Low-complexity Rake reception in a realistic UWB channel," in *Proc. ICC 2002*, Vol. 2, pp. 763-767.

[84] E. Fishler and H. V. Poor, "Low-complexity multi-user detectors for time hopping impulse radio systems," *IEEE Trans. Signal Process.*, vol. 52, pp. 2561-2571, Sep. 2004.

[85] Y. -L. Chao and R. A. Scholtz, "Multiple access performance of ultra-wideband transmitted reference systems in multipath environments," in *Proc. WCNC 2004*, pp. 21-25.

[86] T. S. Rappaport, *Wireless Communications: Principles and Practice*. New Jersey: Prentice Hall, 1996.

[87] B. Lu, X. Wang, and K. R. Narayanan, "LDPC-based space-time coded OFDM systems over correlated fading channels: performance analysis and receiver design," *IEEE Trans. Commun.*, vol. 50, pp. 74-88, Jan. 2002.

[88] G. Strang, *Linear Algebra and Its Applications*. New York: Harcourt-Brace-Jovanovich, 1988.

[89] X. Hong and C. Wang, "A correlation based double directional stochastic model for MIMO-UWB propagation channels," in *Proc. IEE UWSTA 2006*, pp. 249-253.

[90] I. Bergel, E. Fishler, and H. Messer, "Narrowband interference suppression in time-hopping impulse-radio systems," in *Proc. UWBST 2002*, pp. 303-307.

[91] E. Baccarelli, M. Biagi, and L. Taglione, "A novel approach to in-band interference mitigation in ultra wideband radio systems," in *Proc. UWBST 2002*, pp. 297-301.

[92] M. G. Luby, M. Mitzenmacher, M. A. Shokrollahi, and D. A. Spielman, "Efficient erasure correcting codes," *IEEE Trans. Inform. Theory*, vol. 47, pp. 569-584, Feb. 2001.

[93] Y. Kou, S. Lin, and M. P. C. Fossorier, "Low-density parity-check codes based on finite geometries: a rediscovery and new results," *IEEE Trans. Inform. Theory*, vol. 47, pp. 2711-2736, Nov. 2001.

[94] R. Lucas, M. P. C. Fossorier, Y. Kou, and S. Lin, "Iterative decoding of one-step majority-logic decodable codes based on belief propagation," *IEEE Trans. Commun.*, vol. 48, pp. 931-937, June 2000.

[95] S. J. Johnson and S. R. Weller, "A family of irregular LDPC Codes with low encoding complexity," *IEEE Commun. Lett.*, vol. 7, pp. 79-81, Feb. 2003.

[96] J. G. Frias and W. Zhong, "Approaching Shannon performance by iterative decoding of linear codes with low-density generator matrix," *IEEE Commun. Lett.*, vol. 7, pp. 266-268, June 2003.

[97] J. Li, K. R. Narayanan, and C. N. Georghiades, "Product accumulate codes: a class of codes with near-capacity performance and low decoding complexity," *IEEE Trans. Inform. Theory*, vol. 50, pp. 31-46, Jan. 2004.

[98] T. W. Hungerford, *Algebra*. New York: Springer-Verlag, 1974.

List of Publications

Journal Papers

[1] Qi Zhang and Chun Sum Ng, "Differentially-encoded di-Symbol time-division multiuser impulse radio in UWB channel," *accepted for publication by the IEEE Transactions on Communications*.

[2] Qi Zhang and Chun Sum Ng, "Differential space-time coded MIMO impulse radios with autocorrelation receiver in UWB channels," *submitted to the IEEE Transactions on Wireless Communications*.

Conference Papers

[3] Qi Zhang and Chun Sum Ng, "LDPC product codes," in *Proc. ICCS 2004*, 481 - 483.

[4] Qi Zhang and Chun Sum Ng, "Differential TDMA impulse radio systems using delay-sum scheme in UWB channel," in *Proc. GLOBECOM 2005*, pp. 3670-3675.

[5] Qi Zhang and Chun Sum Ng, "Differential space-time coded impulse radio systems using MIMO autocorrelation reveivers in UWB channel," in *Proc. VTC 2006-Fall*, accepted for presentation.